

Rochester Institute of Technology

**RIT Digital Institutional Repository**

---

Theses

---

8-6-2021

## **Coplanar Electrowetting-Induced Droplet Ejection for 3D Digital Microfluidic Devices**

Collin Taylor Burkhart  
ctb6973@rit.edu

Follow this and additional works at: <https://repository.rit.edu/theses>

---

### **Recommended Citation**

Burkhart, Collin Taylor, "Coplanar Electrowetting-Induced Droplet Ejection for 3D Digital Microfluidic Devices" (2021). Thesis. Rochester Institute of Technology. Accessed from

This Dissertation is brought to you for free and open access by the RIT Libraries. For more information, please contact [repository@rit.edu](mailto:repository@rit.edu).

# **Coplanar Electrowetting-Induced Droplet Ejection for 3D Digital Microfluidic Devices**

By:

**Collin Taylor Burkhart**

A dissertation submitted in partial fulfillment of the requirements  
for the degree of Doctor of Philosophy in Engineering

Department of Mechanical Engineering  
Kate Gleason College of Engineering

Rochester Institute of Technology

Rochester, New York

Submitted August 6, 2021

# Coplanar Electrowetting-Induced Droplet Ejection for 3D Digital Microfluidic Devices

By:

**Collin Taylor Burkhardt**

## Committee Approval:

We, the undersigned committee members, certify that we have advised and/or supervised the candidate on the work described in this dissertation. We further certify that we have reviewed the dissertation manuscript and approve it in partial fulfillment of the requirements of the degree of Doctor of Philosophy in Engineering.

---

Dr. Michael Schertzer (Advisor) Date  
*Associate Professor, Department of Mechanical Engineering*

---

Dr. Vinay Abhyankar Date  
*Assistant Professor, Department of Biomedical Engineering*

---

Dr. Ke Du Date  
*Assistant Professor, Department of Mechanical Engineering*

---

Dr. Michael Schlau Date  
*Associate Professor, Department of Mechanical Engineering*

## Certified by:

---

Dr. Edward Hensel Date  
*Director, PhD in Engineering Program*

## Abstract

Digital microfluidics is a promising fluid processing technology used in lab-on-a-chip applications to perform chemical synthesis, particle filtration, immunoassays, and other biological protocols. Traditional digital microfluidic (DMF) devices consist of a 2D grid of coated electrodes over which droplets are manipulated. Selective activation of the electrodes results in an electrowetting effect that deforms the droplets and can move them around the electrode grid. More recently, electrowetting on dielectric has also been used to eject droplets and transfer them between opposing surfaces. This has given rise to new 3D DMF devices capable of more sophisticated routing patterns that can minimize cross-contamination between different biological reagents used during operation. A better understanding of electrowetting-induced droplet ejection is critical for the future development of efficient 3D DMF devices.

The focus of this work was to better predict electrowetting-induced droplet ejection and to determine how droplet selection and electrode design influence the process. An improved model of droplet gravitational potential and interfacial energy throughout ejection was developed that predicts a critical electrowetting number necessary for successful detachment. Predictions using the new model agreed more closely with experimentally observed thresholds than previous models, especially for larger droplet volumes. Droplet ejection experiments were also performed with a variety of coplanar electrode designs featuring different numbers of electrode pieces and different spacings between features. The critical voltage for ejection was observed to be approximately the same for all designs, despite the poor predicted performance for the case with the widest spacing ( $200\ \mu\text{m}$ ) where nearly 25% of the area beneath the droplet was dead space. Findings indicated that a critical electrowetting for ejection must be achieved at the contact line of a droplet rather than over the entire droplet region. Droplets were also ejected for the first time from devices with inkjet-printed electrodes, demonstrating the feasibility of future low-cost 3D DMF systems.

## Acknowledgments

This work was only possible with support from numerous people along the way. I would first like to thank my advisor, Dr. Michael Schertzer. He sparked my interest in digital microfluidics when I was still an undergraduate. His guidance and support since then have been instrumental to the success of my subsequent master's research and my doctoral research here. I also wish to thank Dr. Maki, our collaborator of nearly seven years. She has always offered an interesting perspective, and her insights and suggestions have improved the quality of my research.

I would also like to extend my sincere thanks to the members of my dissertation research committee: Dr. Vinay Abhyankar, Dr. Ke Du, and Dr. Michael Schrlau. I was fortunate to be able to present my work to them many times over the years. The encouraging comments and helpful suggestions I received from them, and from other professors and students in attendance at these presentations, are very much appreciated.

I am also grateful to the PhD in Engineering program for providing me with this research opportunity and funding to pursue it. Dr. Edward Hensel helped me plan my path through the program before it even began, and he and Rebecca Ziebarth have always had answers for my questions along the way. I am also thankful to Dr. Risa Robinson and the Mechanical Engineering Department for financial support. My thanks extend to the faculty and staff I have worked with over the last decade. Our lab would not be running without the support of Jan Maneti, William Finch, Len Levaskevich, and Brittany Pasquale.

Two other labs at RIT were vital to this work. I would like to thank Thomas Grimsley, Patricia Meller, and Sean O'Brien of the Semiconductor and Microsystems Fabrication Laboratory (SMFL) for use of their cleanroom facilities and assistance with processing. I also wish to thank Dr. Denis Cormier, Dr. Bruce Kahn, and Manoj Meda of the Center for Additive Manufacturing and Multifunctional Printing (AMPrint) for their help analyzing our printed electrodes.

I have had the pleasure of working with a number of other graduate students throughout the course of my studies. A special thanks to Hee Tae An, Kimberly Bernetski, Sari Houchaimi, Elisabeth McClure, and Olivia Scheibel for their advice and encouragement over the last years and for sharing successes, failures, and meals together.

Finally, I am extremely thankful to my wife, Cammie Johanning. Your unending love and support have helped make all of this possible.

# Contents

List of Figures .....	vi
List of Tables .....	ix
Nomenclature .....	x
1.0 Introduction.....	1
1.1 Digital Microfluidics .....	1
1.2 Device Fabrication.....	8
1.3 Objectives .....	8
1.4 List of Contributions.....	10
2.0 Background .....	12
2.1 Electrowetting on Dielectric (EWOD) .....	13
2.2 Electrowetting-Induced Droplet Ejection.....	22
2.3 Ejection Threshold.....	24
2.4 Droplet Ejection in Air .....	27
3.0 Experimental Methodology .....	30
3.1 Cleanroom-Fabricated (CRF) Devices .....	30
3.2 Inkjet-Printed (IJP) Devices .....	35
3.3 Ejection Setup.....	39
3.4 Image Capture and Processing .....	42
3.5 Electrode Design Analysis.....	43
4.0 Impact of Droplet Size on Ejection.....	46
4.1 Modeling the Ejection Threshold .....	47
4.2 Coplanar Ejection from Radially Symmetric Electrodes .....	55
4.3 Wired Ejection.....	57
4.4 Significance of Gravitational Potential Energy .....	58
4.5 Summary.....	62
5.0 Impact of Electrode Geometry on Ejection .....	64
5.1 Electrode Design Variations.....	65
5.2 Design Analysis.....	66
5.3 Droplet Ejection Results.....	70
5.4 Contact Line Electrowetting Model .....	72
5.5 Designing for Localized Electrowetting.....	76
5.6 Summary.....	78
6.0 Ejection from Inkjet-Printed Devices .....	79
6.1 Conductivity of Printed Electrodes.....	80
6.2 Roughness, Dielectric Thickness, and Adhesion.....	82
6.3 Droplet Ejection.....	84
6.4 Summary.....	86
7.0 Concluding Remarks.....	88
7.1 Summary.....	88
7.2 Contributions .....	90
7.3 Future Work.....	92
References.....	96

## List of Figures

Figure 1.1	Schematic of an open coplanar digital microfluidic device from the (a) top and (b) side views.	3
Figure 1.2	Schematic of a closed digital microfluidic device from the (a) top and (b) side views.	4
Figure 1.3	Droplet transfer between plates achieved by (a) transitioning between open and closed regions and (b) bridging after vertical distortion.	6
Figure 1.4	3D DMF devices allow a droplet to be (a) transferred to the opposite plate, (b) moved past a separate droplet on the initial plate, and (c) transferred back to the initial plate.	7
Figure 2.1	The unactuated initial contact angle of a droplet on a surface is a function of the relative strengths of the interfacial surface tensions.	14
Figure 2.2	Side-view diagram of a typical wired electrowetting setup.	15
Figure 2.3	Side-view diagram of a typical coplanar electrowetting setup.	17
Figure 2.4	Side-view diagrams of the different circuits within (a) wired and (b) coplanar electrowetting setups.	18
Figure 2.5	Partial electrowetting pulls a droplet toward an active electrode.	20
Figure 2.6	Electrodes in a DMF device are sized to allow a droplet to cover adjacent positions. Interdigitations can also be included to ensure overlap.	21
Figure 2.7	A $5\ \mu\text{L}$ sodium chloride droplet actuated beyond saturation voltage (a) after approximately $7\ \text{ms}$ and (b) after several seconds. The droplet overshoots its steady-state position. <sup>35</sup>	22
Figure 2.8	A $3\ \mu\text{L}$ sodium chloride droplet undergoing electrowetting-induced droplet ejection in air. <sup>57</sup>	24
Figure 2.9	The work to separate two surfaces can generally be expressed as a change in surface energies.	25
Figure 2.10	Side-view depiction of a droplet at its (a) maximally spread and (b) detachment threshold positions.	26

Figure 2.11	Top-view diagram of an interdigitated finger electrode design like that previously used for coplanar electrowetting-induced droplet ejection in air. <sup>56</sup> An actuated droplet tends to deform asymmetrically along the electrodes.	29
Figure 3.1	Top-view diagram of the radially symmetric ejection pad design used in a CRF4 device. Gaps and wiring are enlarged for visibility. A 10 $\mu L$ droplet is shown for scale. <sup>35</sup>	32
Figure 3.2	Side-view diagrams of the layers in the (a) wired and (b) coplanar CRF devices used.	34
Figure 3.3	Experimental facility for low-cost fabrication of electrodes by inkjet printing.	36
Figure 3.4	Side-view diagram of the layers in the wired IJP devices used.	38
Figure 3.5	Experimental facility used to perform electrowetting-induced droplet ejection. <sup>57</sup>	40
Figure 3.6	Electrodes identified in the (a) ejection pads and (b) droplet contact regions of a 5 $\mu L$ droplet ( $\theta_0 \approx 120^\circ$ ) centered on the CRF4-20 design.	44
Figure 4.1	Approximated shape of a droplet at its (a) maximally spread and (b) detachment threshold positions. The quantities $h_s$ and $R_{sph}$ denote the distance from the droplet's center of mass to the substrate in the spread and threshold positions, respectively. <sup>35</sup>	49
Figure 4.2	Predicted $Ew$ detachment thresholds for each model shown as solid lines. From top to bottom (based on 18 $\mu L$ volume): interfacial plus gravitational model (orange), adhesion plus gravitational model (green), interfacial model (purple), and adhesion model (black). <sup>35</sup>	53
Figure 4.3	Increase in predicted electrowetting number (solid) and corresponding voltage (empty) between the adhesion plus gravitational potential model (red circles) and the interfacial plus gravitational model (blue squares) as compared to the adhesion only and interfacial only models, respectively. <sup>35</sup>	54
Figure 4.4	Captured frames of a 5 $\mu L$ droplet on a coplanar device (i) after a 7 $ms$ pulse and then (ii-vi) every $\sim 3.3 ms$ . The droplet exhibits (a) incomplete detachment at 250 $V$ and (b) detachment at 260 $V$ . <sup>35</sup>	55
Figure 4.5	Coplanar detachment threshold results (red circles), wired results	59

(blue squares), Lee et al.'s wired results<sup>56</sup> (black triangles), saturation limit (dashed black), and detachment threshold predictions from top to bottom (based on an 18  $\mu\text{L}$  volume): interfacial plus gravitational model (solid orange), adhesion plus gravitational model (solid green), interfacial model (solid purple), and adhesion model (solid black).<sup>35</sup>

Figure 5.1	Simplified top-view of the detachment pad designs used with varying numbers of segments ( $N$ ) and minimum gap spacings ( $G$ ). Gaps are not to scale. Wiring of alternating segments is not shown. <sup>36</sup>	65
Figure 5.2	Expected area factor efficiency of a 5 $\mu\text{L}$ droplet offset along the midline of an electrode segment (inset). <sup>36</sup>	68
Figure 5.3	A 5 $\mu\text{L}$ droplet ejected from a CRF4-200 electrowetting device. Approximately 5 $\text{ms}$ elapse between consecutive frames. <sup>36</sup>	71
Figure 5.4	Experimentally observed threshold voltage and critical electrowetting number for droplet ejection from each device type. <sup>36</sup>	72
Figure 5.5	Expected perimeter factor efficiency of a 5 $\mu\text{L}$ droplet offset along the midline of an electrode segment. <sup>36</sup>	75
Figure 5.6	Top-view schematic of a theoretical two-part electrode design sized for a 5 $\mu\text{L}$ droplet ( $\theta_0 \approx 120^\circ$ ). <sup>36</sup>	77
Figure 6.1	An early inkjet-printed electrode.	80
Figure 6.2	Conductivity of fresh and dried printed electrodes samples after various curing techniques. <sup>37</sup>	82
Figure 6.3	A single-electrode printed device used for droplet ejection. <sup>37</sup>	85
Figure 6.4	Successful ejection of a 5 $\mu\text{L}$ droplet from an CRF and IJP device. <sup>37</sup>	86
Figure 7.1	Diagram of a proposed 3D DMF droplet delivery system for cell culturing applications.	95

## List of Tables

Table 3.1	Initial printer settings used for IJP electrode fabrication and nozzle cleaning <sup>37</sup>	37
Table 3.2	Later printer settings used for IJP electrode fabrication and cleaning to improve printer longevity	37
Table 3.3	Estimated electrode fabrication costs for a batch of eight CRF or eight IJP devices	39
Table 4.1	Bond numbers for a droplet in air on a Teflon surface ( $\theta_0 = 120.1^\circ$ ) <sup>35</sup>	50
Table 4.2	Deviations in droplet geometry at maximum spreading <sup>35</sup>	50
Table 4.3	Observed droplet ejection thresholds <sup>35</sup>	56
Table 4.4	Deviations from predicted thresholds <sup>35</sup>	60
Table 5.1	Predicted electrowetting performance over the contact area of a centered $5 \mu L$ droplet ( $\theta_0 = 120^\circ$ ) <sup>36</sup>	67
Table 5.2	Predicted electrowetting performance along the contact line of a centered $5 \mu L$ droplet ( $\theta = 75^\circ$ ) <sup>36</sup>	74

# Nomenclature

<b>Symbol</b>	<b>Meaning</b>
$A_a$	Active electrode area covered by a droplet
$A_g$	Gap area covered by a droplet
$A_r$	Reference electrode area covered by a droplet
$A_s$	Contact area of a maximally spread droplet
$A_t$	Total area covered by a droplet
$Bo$	Bond number
$c$	Capacitance per unit area
$c_a$	Capacitance per area of the dielectric layer over active electrodes
$c_d$	Capacitance per unit area of the dielectric layer
$c_h$	Capacitance per unit area of the hydrophobic layer
$c_H$	Helmholtz capacitance per unit area of the electric double layer
$c_r$	Capacitance per area of the dielectric layer over reference electrodes
$d$	Dielectric layer thickness
$E_{cr}$	Total free interfacial energy in the critically detached state
$\Delta E_g$	Net change in gravitational potential energy
$\Delta E_{int}$	Net change in total free interfacial energy
$E_s$	Total free interfacial energy in the maximally spread state
$E_{s,lg}$	Component of $E_s$ along the liquid-gas interface
$E_{s,sg}$	Component of $E_s$ along the solid-gas interface
$E_{s,sl}$	Component of $E_s$ along the solid-liquid interface
$EW$	Electrowetting number
$EW_A$	Effective $EW$ over the droplet contact area in a coplanar device
$EW_{cr}$	Minimum $EW$ required for droplet ejection
$EW_{cr,adh}$	$EW_{cr}$ as computed by the adhesion model
$EW_{cr,adh+g}$	$EW_{cr}$ as computed by the adhesion plus gravitational potential model

$E_{W_{cr,int}}$	$E_{W_{cr}}$ as computed by the interfacial model
$E_{W_{cr,int+g}}$	$E_{W_{cr}}$ as computed by the interfacial plus gravitational potential model
$E_{W_P}$	Effective $E_{W}$ over the droplet contact line in a coplanar device
$f_{adh}$	Detachment function for the adhesion model
$f_{adh+g}$	Detachment function for the adhesion plus gravitational potential model
$f_{int}$	Detachment function for the interfacial model
$f_{int+g}$	Detachment function for the interfacial plus gravitational potential model
$G$	Gap width
$g$	Acceleration due to gravity
$H$	Droplet height
$h_{cap}$	Center of mass height of a spherical cap
$h_s$	Center of mass height of a maximally spread droplet
$L$	Characteristic droplet length
$N$	Number of segments
$n$	Number of trials
$p$	Probability value for statistical testing
$R$	Radius of curvature
$R_{sph}$	Radius of a sphere with the same volume as the droplet
$\hat{R}$	Arbitrary radius of a cylindrical system domain larger than $R$
$r$	Droplet contact radius
$r_{inner}$	Radius of the inner circle electrode
$r_{outer}$	Radius of the outer ring electrode
$s$	Sample standard deviation
$s_a$	Length of contact line over active electrodes
$s_g$	Length of contact line over gaps
$s_r$	Length of contact line over reference electrodes
$s_t$	Total length of the contact line
$t$	Time

$t_s$	Time to maximal spreading
$U$	Input voltage
$U_a$	Voltage across the dielectric over active electrodes
$U_g$	Voltage across the dielectric over gaps
$U_r$	Voltage across the dielectric over reference electrodes
$\tilde{U}_A$	Effective voltage over the droplet contact area in a coplanar device
$\tilde{U}_P$	Effective voltage over the droplet contact line in a coplanar device
$V$	Droplet volume
$w$	Work per area
$w_{adh}$	Adhesion work per area
$w_{sl}$	Work per area to separate the solid-liquid interface
$\alpha_A$	Area factor
$\alpha_P$	Perimeter factor
$\gamma$	Surface energy, surface tension
$\gamma_g$	Surface energy along the liquid-gas interface, droplet surface tension
$\gamma_{sg}$	Surface energy along the solid-gas interface
$\gamma_{sl}$	Surface energy along the solid-liquid interface
$\epsilon_0$	Permittivity of free space
$\epsilon_d$	Dielectric constant
$\eta_A$	Area efficiency
$\eta_P$	Perimeter efficiency
$\theta_0$	Initial contact angle
$\theta_U$	Apparent contact angle during actuation
$\rho$	Density of the droplet
$\Delta\rho$	Density difference between the droplet and surrounding medium

**Abbreviation    Meaning**

CRF	Cleanroom-fabricated
CRF1	A single-electrode CRF device
CRF4-20	A four-part CRF device with 20 $\mu m$ spacing

CRF4-200	A four-part CRF device with 200 $\mu m$ spacing
CRF4-55	A four-part CRF device with 55 $\mu m$ spacing
CRF6-20	A six-part CRF device with 20 $\mu m$ spacing
CRF8-20	An eight-part CRF device with 20 $\mu m$ spacing
DI	Deionized
DMF	Digital microfluidic
EDL	Electric double layer
EWOD	Electrowetting on dielectric
IJP	Inkjet-printed
IJP1	A single-electrode IJP device
LOC	Lab-on-a-chip
PDMS	Polydimethylsiloxane
PET	Polyethylene terephthalate
POC	Point of care
ROI	Region of interest

## 1.0 Introduction

Microfluidics is a multidisciplinary field in which fluids are processed at small scales where the effects of surface forces begin to outweigh the effects of body forces, unlike in macroscale systems. It can broadly be divided into two branches depending on how a working fluid is processed: continuous-flow microfluidics and droplet-based microfluidics. In continuous-flow systems, fluid flows through sub-millimeter sized channels<sup>1</sup> either passively due to capillary forces<sup>2</sup> or actively via mechanical pumps<sup>3,4</sup> or electrokinetics.<sup>5</sup> In droplet-based systems, discrete volumes of fluid are manipulated in air or while dispersed through another immiscible fluid.<sup>6,7</sup> Droplets are typically several microliters or smaller in volume.<sup>6</sup>

Lab-on-a-chip (LOC) devices leverage the small footprint of microfluidic techniques to perform fluid processing functions on a single palm-sized chip rather than in an entire traditional laboratory.<sup>8,9</sup> The scale of a microfluidic approach reduces the required quantities of reagents required.<sup>1,9</sup> The higher surface-area-to-volume ratio at the microscale also expedites heat and mass transfer.<sup>6,10</sup> These devices are typically used to perform diagnostic and other biomedical tests.<sup>11,12</sup> The size and processing speed of LOC devices also makes them well suited for point-of-care testing.<sup>7,11-13</sup>

### 1.1 Digital Microfluidics

Digital microfluidic (DMF) devices are a class of droplet-based LOC device that manipulate droplets over grids of electrodes. Electrical signals applied to select electrodes are used to perform basic droplet operations, such as moving, merging, mixing, and

splitting.<sup>14,15</sup> Sequences of these basic operations can be used to execute a wide variety of biological protocols,<sup>7,16–20</sup> including chemical synthesis, particle filtration, and immunoassays. The DMF platform has several advantages over other microfluidic techniques. It is capable of processing droplets with volumes ranging from picoliters to milliliters.<sup>16,19,21</sup> Multiple droplets can be manipulated simultaneously without the need for additional tubing or valve networks.<sup>7,19</sup> Droplet manipulation sequences can be readily reconfigured to perform a variety of protocols on a single generic electrode array.<sup>7</sup> Solid test samples can also be used by suspending them in a working fluid, and subsequent processing can be performed without any risk of clogging.<sup>7,19,22–24</sup>

Traditional DMF devices can be broadly classified as “open” or “closed” based on their structure.<sup>7,15</sup> In an “open” device (Fig. 1.1), droplets rest on a single substrate containing a 2D array of coplanar electrodes. The electrodes are coated with dielectric and hydrophobic polymer layers that prevent electrical breakdown and improve droplet manipulation, respectively. Droplets are typically surrounded by air which allows them to be easily accessed.<sup>19</sup> Voltage is applied either across two electrode beneath a droplet or across one electrode and a wire inserted into the droplet. This produces an electrowetting response in which the droplet deforms and spreads toward the substrate surface. Deformation of only part of a droplet creates a pressure difference across the droplet interface that can induce bulk motion. Selective electrode activation can leverage this to position droplets as desired in 2D space. Separate droplets can also be merged and mixed together.

In a “closed” DMF device (Fig. 1.2), droplets are also contacted from above by a second hydrophobic substrate. Different immiscible fluids can be filled between the two

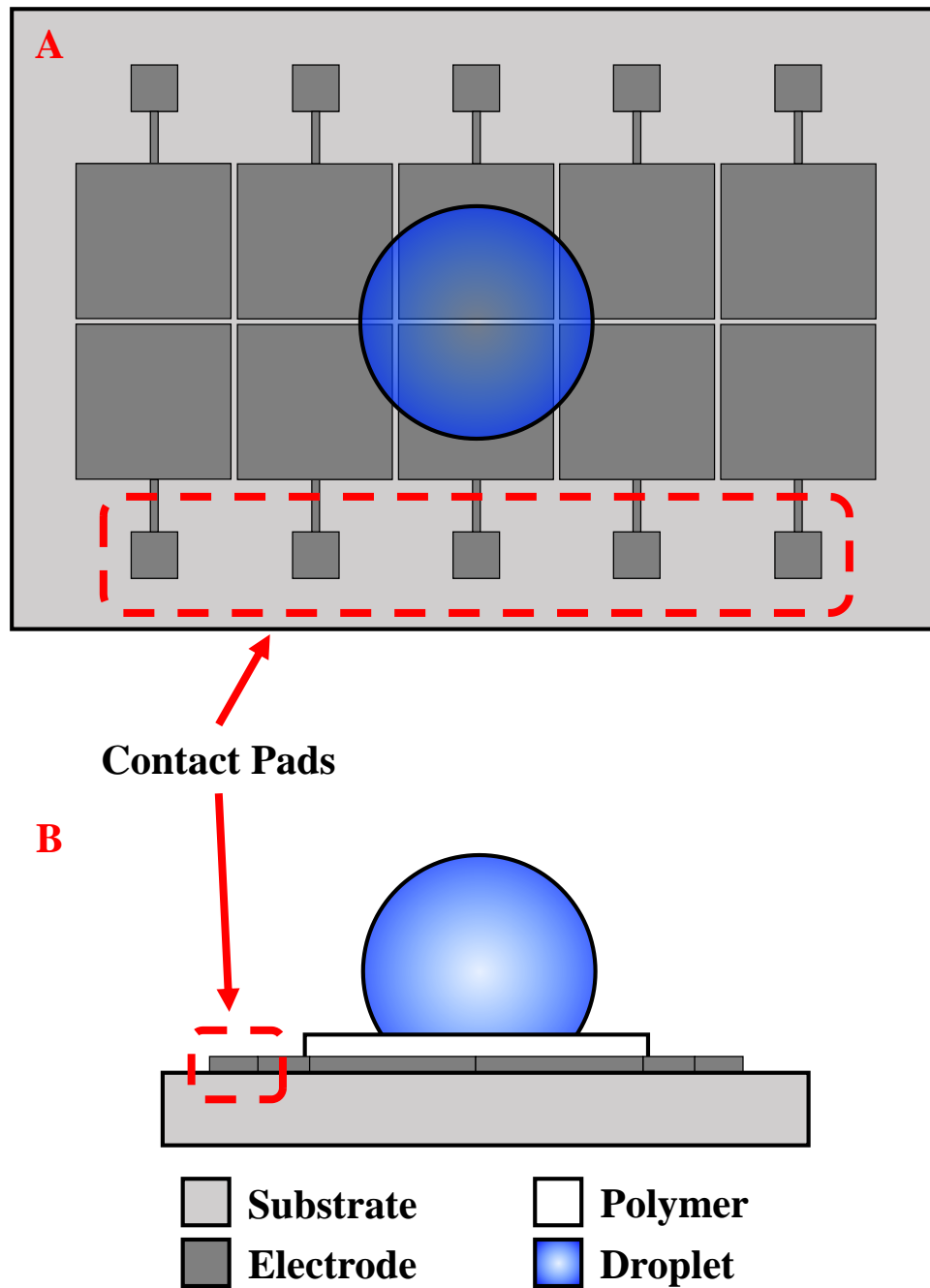


**Figure 1.1** Schematic of an open coplanar digital microfluidic device from the (a) top and (b) side views.

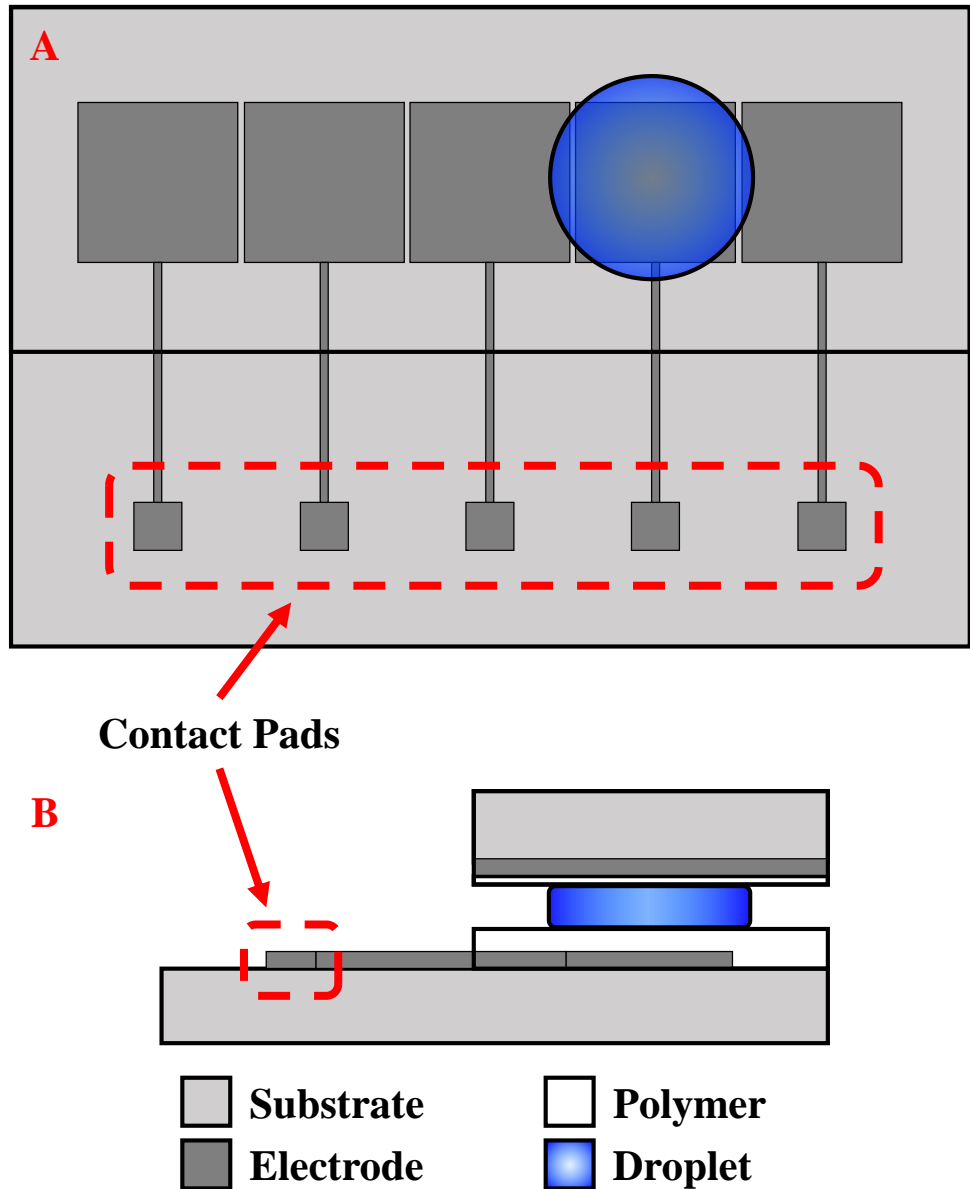


**Figure 1.2** Schematic of a closed digital microfluidic device from the (a) top and (b) side views.

substrates to facilitate droplet movement<sup>14,25–27</sup> and limit evaporation.<sup>14,25,28</sup> The second substrate may contain electrodes, but this is not strictly necessary. Voltage can be applied across either two coplanar electrodes on a single substrate or two electrodes on opposite substrates to produce an electrowetting response that induces motion.<sup>29</sup> Selective electrode

activation can produce the same moving, merging, and mixing possible in an open device. A closed design is also capable of splitting droplets apart.<sup>14,15</sup>

More sophisticated “3D” DMF devices incorporate elements of both open and closed devices. They can perform traditional 2D droplet movements and also transfer droplets between opposing substrates using the same electrowetting mechanism. This can be done using a hybrid device with a closed region that widens to two separate open regions.<sup>30</sup> Droplets can be transferred from one open substrate to the other by first transitioning through the closed region (Fig. 1.3a). Similar transfer can also be achieved in a device consisting of only two opposing open substrates. Carefully tuned electrowetting signals can create vertical distortions in the shape of a droplet. This can result in the formation of a temporary bridge between two opposing open devices in close proximity that transfers a droplet across (Fig. 1.3b).<sup>31,32</sup> Tuned electrowetting signals can also induce detachment and eject a droplet to an opposing substrate.<sup>33-37</sup> As in a closed device, the gap between two opposing open substrates in a 3D device can be filled with an immiscible fluid to facilitate droplet transfer.

The droplet transfer functionality in 3D DMF devices gives two primary advantages over 2D devices. First, a 3D DMF is capable of more sophisticated droplet routing not possible in only two dimensions. Droplets can be moved across a device without ever crossing paths (Fig. 1.4).<sup>34,38-40</sup> Second, a 3D DMF device can support a larger number of droplet operations in a given device footprint. The working area is up to twice that of a 2D device since the opposing open substrates can perform independent operations. These advantages make 3D devices well suited for biomedical applications where sensitivity can suffer due to reagent cross-contamination<sup>41,42</sup> and adsorption.<sup>16,17</sup>

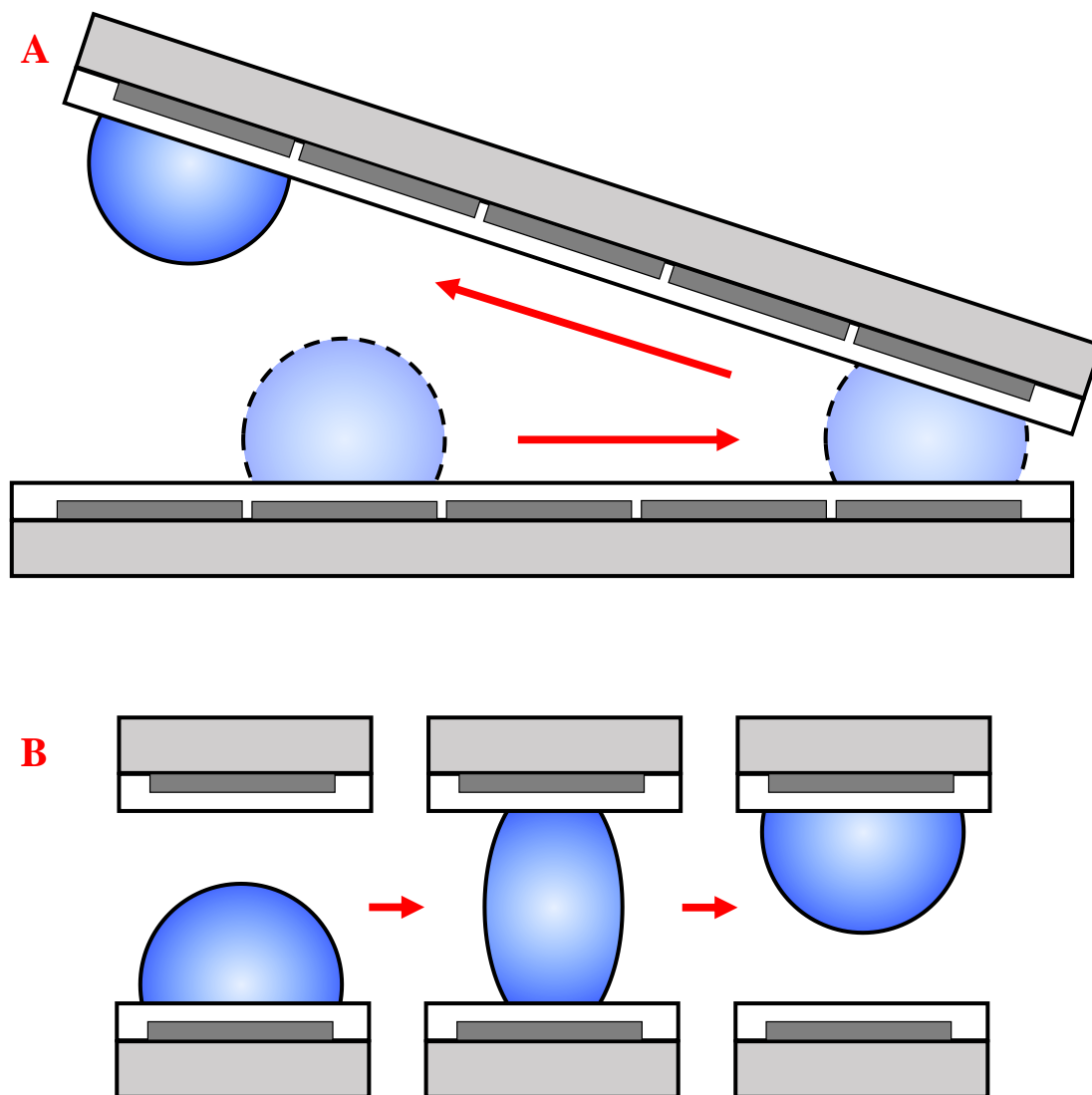


**Figure 1.3** Droplet transfer between plates achieved by (a) transitioning between open and closed regions and (b) bridging after vertical distortion.

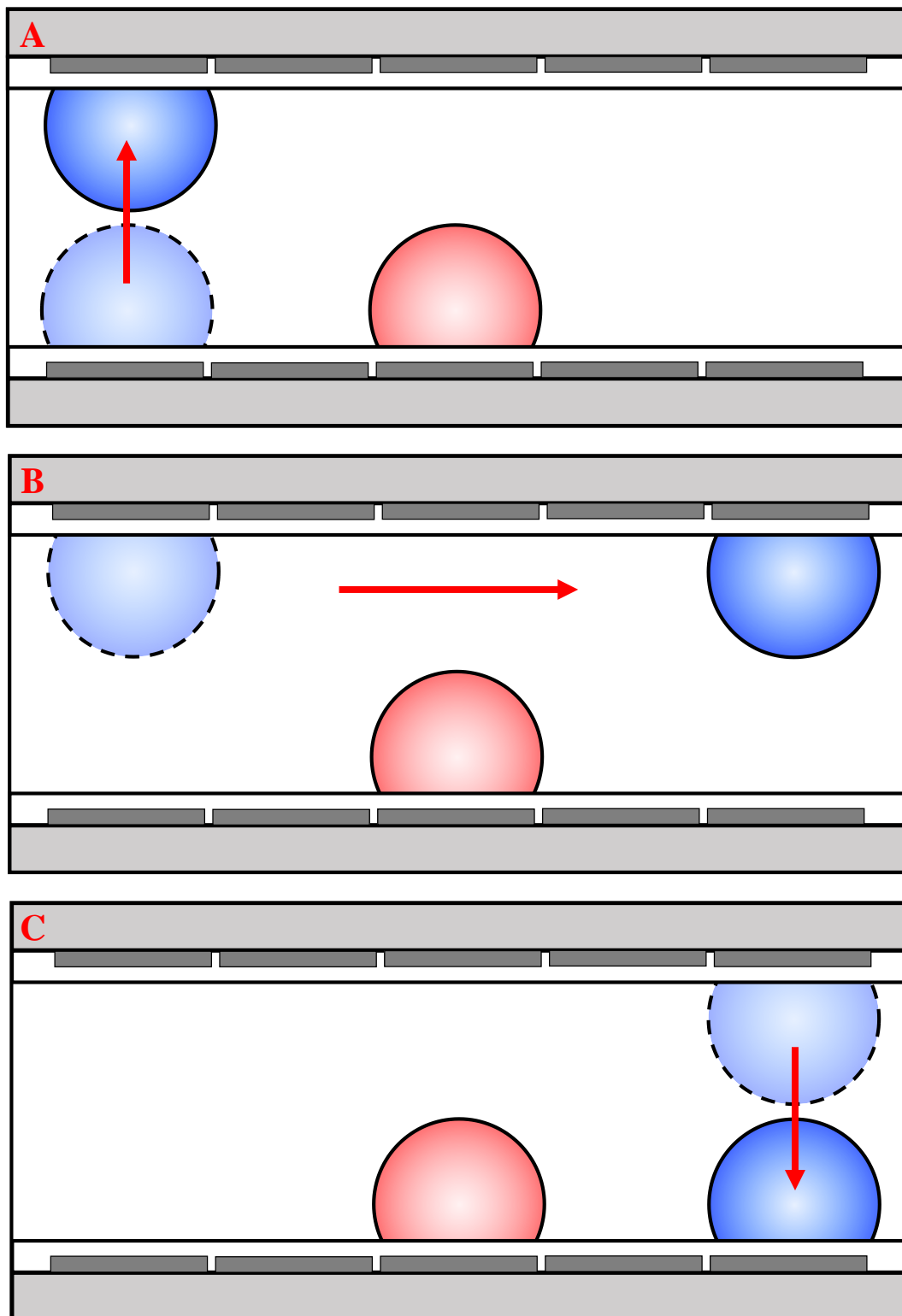


**Figure 1.4** 3D DMF devices allow a droplet to be (a) transferred to the opposite plate, (b) moved past a separate droplet on the initial plate, and (c) transferred back to the initial plate.

## 1.2 Device Fabrication

The fabrication of DMF devices is a critical hurdle for their implementation as point of care (POC) diagnostic tools. Due to the nature of their operation, devices require small features that can be difficult to produce. Fabrication is traditionally performed in cleanroom facilities<sup>43,44</sup> and involves photolithography to form the desired electrode arrays and spin coating to apply various polymer layers. This processing has a high cost per device due to the necessary facilities, equipment, materials, and trained technicians.<sup>44,45</sup> Reducing these costs has been an ongoing focus in the development of new DMF devices.

A variety of alternative fabrication techniques have been developed that reduce fabrication costs by producing device electrodes without the need for cleanroom facilities.<sup>18,37,46–51</sup> Custom polydimethylsiloxane (PDMS) stamps can be coated with different materials and used to microprint conductive layers.<sup>46</sup> Masking images can be laser printed<sup>47</sup> or hand drawn<sup>48</sup> directly onto copper sheets and etched to form the desired electrode pattern. Inkjet printers can also be used to deposit conductive inks onto photopapers<sup>49</sup> and other polymer films<sup>18,50</sup> to create flexible electrodes.<sup>18,37,49–51</sup> Alternative techniques often sacrifice feature resolution, but resulting devices can still be of practical benefit. One inkjet printing process using an inexpensive commercial printer (~\$120 USD) was able to produce devices with a minimum electrode spacing of  $\sim 50 \mu\text{m}$  that were capable of diagnosing measles and rubella in the field.<sup>18,50</sup>

## 1.3 Objectives

The overarching goal of this work is to improve the current physical understanding of electrowetting-induced droplet ejection. Such understanding is valuable in a variety of

applications where electrowetting is used to facilitate droplet removal, such as windshields,<sup>52</sup> cameras,<sup>53</sup> and condensation heat systems.<sup>54,55</sup> However, this work is specifically motivated by 3D DMF applications where droplet ejection can enable new routing<sup>34,38-40</sup> that minimizes cross-contamination in biological tests.<sup>16,17,41,42</sup> An improved understanding of ejection can facilitate the development of 3D DMF devices by revealing how different design parameters affect device operation and making ejection capabilities easier to implement.

To this end, this work has three main objectives. The first is (i) to determine how droplet size impacts electrowetting-based droplet ejection. Previous approximations of the ejection threshold<sup>56</sup> and modeling of the energy throughout detachment<sup>38</sup> have considered only interfacial energies. These models are detailed in Chapter 2. However, gravitational potential energy also changes throughout detachment. The magnitude of this change scales with size and may introduce error in the predicted threshold of larger droplets. Here, experiments are performed in which droplets of varying sizes are ejected from DMF devices using the setup described in Chapter 3. A new analytical model of both the interfacial and gravitational potential energies during detachment is developed in Chapter 4 to better predict the ejection threshold. Thresholds observed during experimentation are used to validate the thresholds predicted by the model. Findings from this improved ejection model can be used to inform droplet selection in future 3D DMF devices.

The second objective of this work is (ii) to determine how electrode geometry impacts electrowetting-based droplet ejection. While traditional cleanroom fabrication is capable of producing electrodes micron-scale features, the process can be expensive. Low-cost inkjet-printing fabrication can produce devices of comparable quality,<sup>49,50</sup> but this

technique is more limited in the electrode sizes and spacings it can produce. Understanding how electrode design features impact droplet ejection is valuable since fabrication constraints can vary between techniques. In Chapter 5, droplets are ejected from DMF devices with varying numbers of ejection pad segments and varying electrode spacings. Experimentally observed thresholds are then compared to those predicted by the proposed interfacial plus gravitational potential energies model. During subsequent analysis, a model of how electrode geometry impact the electrowetting number at the contact line of an actuated droplet is also developed. Findings from this investigation can be used to increase the efficiency of ejection electrode designs used in 3D DMF devices.

The final objective of this work is (iii) to demonstrate electrowetting-induced droplet ejection from a low-cost DMF device. Inkjet printing is a promising low-cost fabrication technique. One process in particular has already been used to produce 2D DMF devices that have successfully performed POC testing.<sup>18,50</sup> In Chapter 6, single-electrode devices are fabricated using a similar inkjet printing process and used to eject droplets. Successful droplet ejection from inkjet-printed devices demonstrates the feasibility of future low-cost 3D DMF devices. Such devices would allow 3D DMF technology to be studied more easily by new research laboratories and would make 3D DMF devices more affordable for POC diagnostic applications.

## **1.4 List of Contributions**

Three separate investigations were performed in this work and are discussed in detail throughout the following chapters. The findings of these investigations have been disseminated to the wider scientific community through a publication in *Langmuir*,<sup>35</sup> a

publication in *Microfluidics and Nanofluidics*,<sup>37</sup> and a submission for publication in *Sensors and Actuators A: Physical*.<sup>36</sup> Results were also shared with the local community through an article in *The Rochester Engineer*.<sup>57</sup> The original contributions are as follows:

- A numerical approach for computing the effective electrowetting number on different coplanar ejection electrode designs.<sup>35,36</sup>
- An analytical model of changes in the interfacial and gravitational potential energies during droplet ejection that can be used to predict the ejection threshold.<sup>35</sup>
- An empirical study of the ejection thresholds for droplets of varying sizes that compared observed thresholds to those predicted by the proposed model as well as previous adhesion work and interfacial energy models.<sup>35</sup>
- The first reported electrowetting-induced droplet ejection in air from coplanar electrode using a single voltage pulse.<sup>35</sup>
- An analytical model of the electrowetting number at the contact line of an actuated droplet.<sup>36</sup>
- An empirical study of the ejection thresholds for droplets ejected from radially symmetric electrode designs with different pad segmentation and spacing that compared observed thresholds to those predicted by the proposed interfacial plus gravitational potential energies model.<sup>36</sup>
- The first reported electrowetting-induced droplet ejection from an inkjet-printed electrowetting device.<sup>37</sup>

## 2.0 Background

Digital microfluidic (DMF) devices operate by means of electrowetting.<sup>14,15,58,59</sup> Electrowetting is the modification of wetting behavior on a surface through the application of electric fields. This interaction was first explained by Gabriel Lippmann in 1875 as the electrocapillarity phenomenon.<sup>58,60</sup> Lippmann observed that in capillary tubes the shape of the interface between mercury and a sulfuric acid solution could be manipulated by applying small voltages across the two phases. The resulting electric field causes charged ions to accumulate at the mercury-acid interface and form an electric double layer (EDL).<sup>58-60</sup> The electrical energy stored in the EDL reduces the effective surface tension of the interface.

Electrowetting in DMF devices extends the principles of electrocapillarity to the case of a droplet on a solid electrode.<sup>14,15,58,59</sup> When a small voltage ( $< 1 V$ )<sup>58</sup> is applied to an aqueous droplet, an EDL forms at the solid-liquid interface and reduces its effective surface tension. This causes an increase in the apparent wettability of the droplet. Higher voltages disrupt the EDL and can result in electrolysis as current flows through the droplet.<sup>58,59</sup> However, the onset of electrolysis can be delayed by including a thin dielectric layer between the electrode and droplet.<sup>14,15,58,59</sup> This configuration was first employed by Berge in 1993 and is now known as electrowetting on dielectric (EWOD).<sup>61,62</sup> The capacitance per area of the dielectric layer is typically much lower than the Helmholtz capacitance per area of the EDL. This causes the applied voltage to drop primarily across the dielectric layer.<sup>14,15,58,59,61,62</sup> Depending on the thickness and dielectric strength of the material used in this layer, larger voltages can be applied without risk of electrolysis.

Material presented here has previously been published in *Langmuir*,<sup>35</sup> published in *Microfluidics and Nanofluidics*,<sup>37</sup> and submitted for publication in *Sensors and Actuators A: Physical*.<sup>36</sup>

## 2.1 Electrowetting on Dielectric (EWOD)

The shape of a static droplet in contact with a flat, rigid surface and surrounded by air is dictated by surface tension and gravitational forces. The relative significance of these two factors is quantified by the Bond number ( $Bo$ )

$$Bo = \frac{\Delta\rho gRH}{\gamma_{lg}}, \quad (2.1)$$

where  $\Delta\rho$  is the different in density between the droplet and surrounding air,  $g$  is the acceleration due to gravity,  $R$  is the radius of curvature of the droplet,  $H$  is the height of the droplet, and  $\gamma_{lg}$  is the surface tension along the liquid-gas interface.<sup>63</sup> A value of  $Bo \approx 1$  indicates that surface tension and gravitational forces both affect the shape of the droplet. Smaller values of  $Bo$  indicate that droplet shape is predominantly affected by surface tension forces and that gravitational effects are negligible. For the droplets examined in this work, gravitational effects on shape are neglected since  $Bo < 1$  in all cases.<sup>58</sup>

In the absence of gravitational effects, a droplet will take the shape of a spherical cap (Fig. 2.1). The initial contact angle ( $\theta_0$ ) of the droplet depends on the surface energies ( $\gamma$ ) along the different interfaces in the system. This relationship is described by the Young equation<sup>58,59</sup>

$$\gamma_{sg} = \gamma_{sl} + \gamma_{lg} \cos \theta_0, \quad (2.2)$$

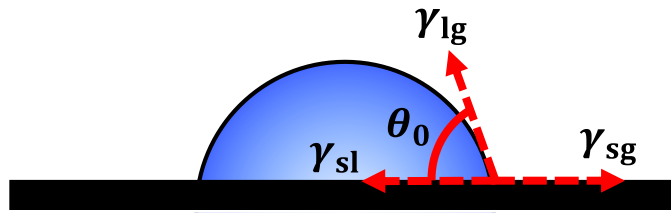


**Figure 2.1** The unactuated initial contact angle of a droplet on a surface is a function of the relative strengths of the interfacial surface tensions.

where the “sg,” “sl,” and “lg” subscripts indicate the solid-gas, solid-liquid, and liquid-gas interfaces, respectively. Two known geometric quantities of a spherical cap, such as volume and initial contact angle, can be used to calculate any other desired geometric quantities, such as the contact area or height. In the presence of gravitational effects,  $\theta_0$  will remain the same but the radius of curvature of the droplet will change over its profile and take a less predictable shape.

An EWOD device can be used to manipulate the droplet and reduce its apparent contact angle ( $\theta_U$ ). A typical open EWOD device consists of four layers: (i) a base substrate material to provide structural support, (ii) a conductive layer of one or more electrodes, and (iii) a dielectric layer to delay electrolysis, and (iv) a hydrophobic layer that contacts the droplet. The hydrophobic layer increases the initial contact angle which allows for greater changes in droplet shape. A dielectric material that is sufficiently hydrophobic can also serve as a single hybrid layer.<sup>14</sup>

In a simple “wired” EWOD setup, a droplet rests over a large, single electrode (Fig. 2.2). A voltage is then applied between the electrode and a wire inserted into the top of the droplet. This charges the layers between the electrode and droplet which reduces the

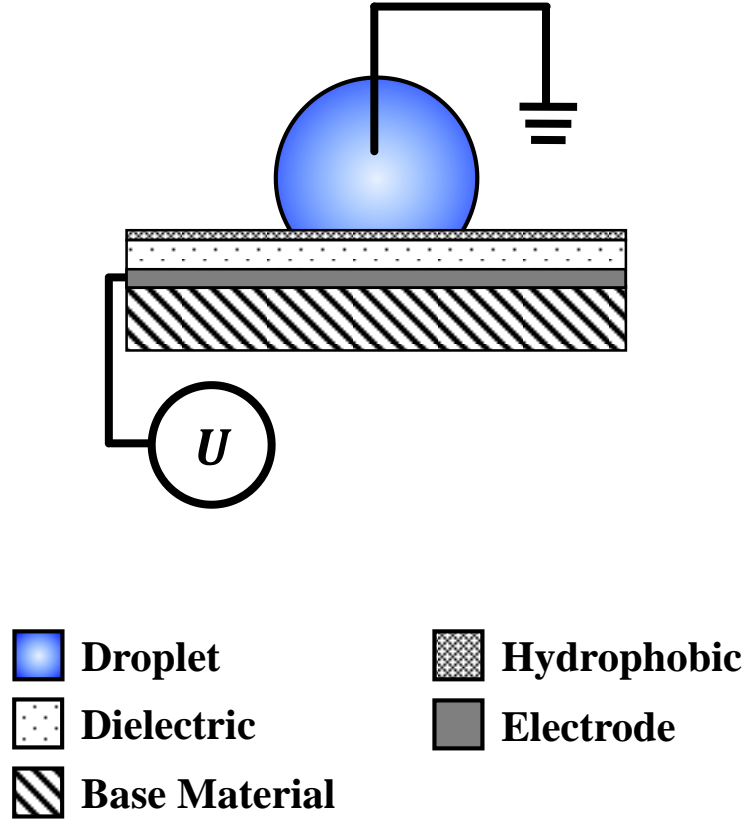


**Figure 2.2** Side-view diagram of a typical wired electrowetting setup.

effective surface energy along the solid-liquid interface ( $\gamma_{sl}(U)$ ). This reduction is expressed by the Lippmann equation<sup>26,59,61</sup>

$$\gamma_{sl}(U) = \gamma_{sl}(0) - \frac{cU^2}{2}, \quad (2.3)$$

where  $\gamma_{sl}(0)$  is the solid-liquid surface energy without an electric field,  $c$  is the total capacitance per unit area between the droplet and electrode, and  $U$  is the voltage applied.

In the case of an AC signal,  $U$  is the root-mean-square voltage applied. The total capacitance is affected by the capacitances per area of the dielectric layer ( $c_d$ ), hydrophobic layer ( $c_h$ ), and EDL ( $c_H$ ). Since these all span the same area,  $c$  can be computed as

$$\frac{1}{c} = \frac{1}{c_d} + \frac{1}{c_h} + \frac{1}{c_H}. \quad (2.4)$$

The capacitance of the EDL has a negligible impact, since  $c_d \ll c_H$  and  $c_h \ll c_H$ .<sup>58</sup> For the devices used here,  $c_h$  also has a negligible impact (within  $\sim 3\%$ ) since  $c_h$  exceeds  $c_d$  by a factor of approximately 30. In such cases the total capacitance per area can then be approximated as the capacitance of the dielectric layer ( $c \approx c_d$ ). The capacitance of the dielectric is expressed as

$$c_d = \frac{\epsilon_0 \epsilon_d}{d}, \quad (2.5)$$

where  $\epsilon_0$  is the permittivity of free space,  $\epsilon_d$  is the dielectric constant, and  $d$  is the thickness of the dielectric layer.

The change in effective solid-liquid surface energy causes the droplet to spread on the surface and reach a new steady-state position. For the aqueous droplets actuated by DC voltages examined in this work, this takes several milliseconds.<sup>35–37,56,64</sup> The steady-state apparent contact angle ( $\theta_U$ ) can be predicted by recalculating Young's equation (Eq. 2.2) based on the reduced effective surface energy (Eq. 2.3). This yields the electrowetting equation<sup>59,65</sup>

$$\cos \theta_U = \cos \theta_0 + \frac{c_d U^2}{2\gamma_{lg}}, \quad (2.6)$$

also known as the Young-Lippmann equation<sup>62,64</sup> or the Berge-Lippmann-Young equation.<sup>15</sup> The dimensionless quantity  $\frac{c_d U^2}{2\gamma_{lg}}$  is known as the electrowetting number ( $EW$ ).

This quantity describes the ratio of the stored electrical energy to the interfacial energy along the boundary of the droplet and surrounding medium. Equation 2.6 accurately predicts steady-state droplet deformation up to a system-dependent saturation voltage. Voltages beyond saturation produce rapidly diminishing further changes in the apparent contact angle.<sup>59,66–68</sup>

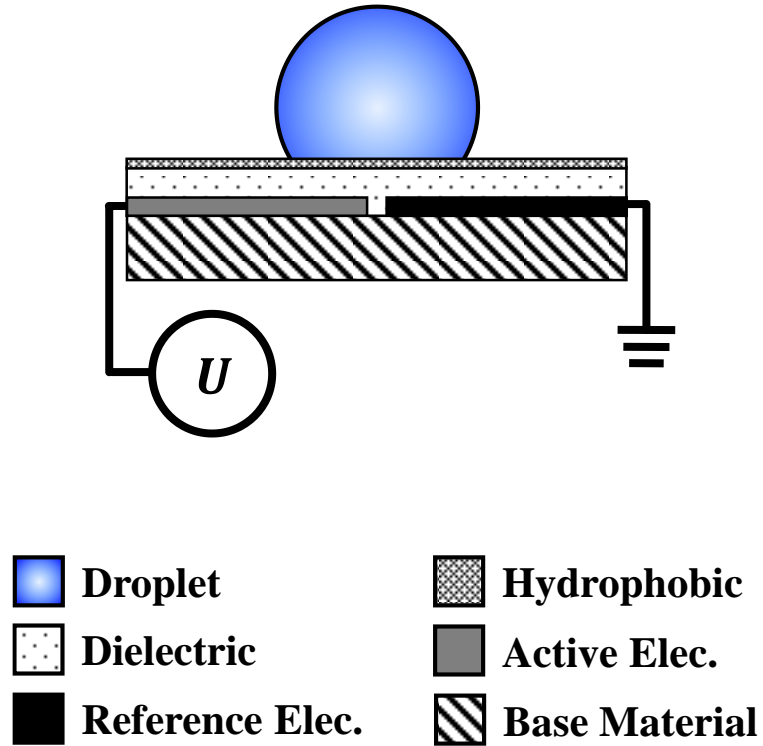
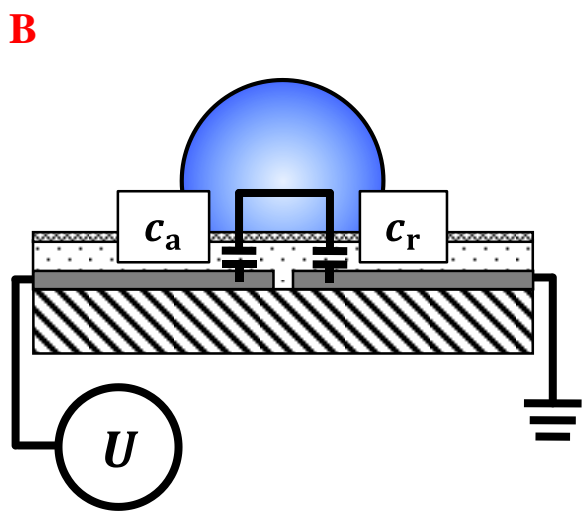
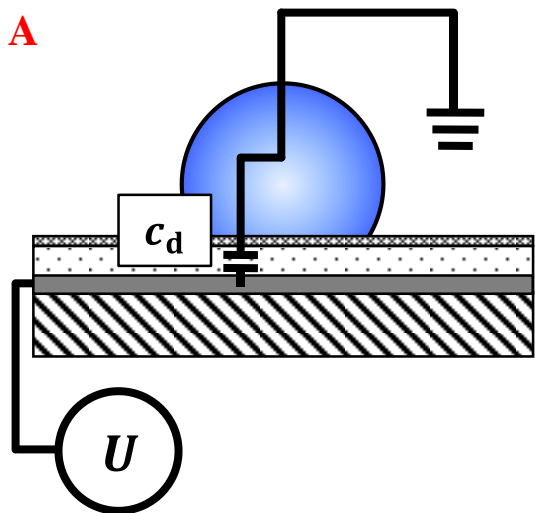


**Figure 2.3** Side-view diagram of a typical coplanar electrowetting setup.

In a more practical “coplanar” EWOD configuration, a droplet rests over multiple electrodes embedded under the dielectric layer (Fig. 2.3). Each covered electrode can serve as either an active or reference electrode depending on how voltage is applied. This type of design is preferred in real-world applications, because it eliminates the need for an external ground wire at each actuation site.<sup>29</sup> This fundamentally changes the device circuit as compared to the wired configuration (Fig. 2.4). In a coplanar design, dielectric material in areas where the droplet covers active electrodes ( $A_a$ ) and in areas where the droplet covers reference electrodes ( $A_r$ ) act as two capacitors in series with capacitances per area of  $c_a$  and  $c_r$ , respectively.<sup>29</sup> When all electrodes have the same dielectric layer, as is the case for all coplanar devices used in this work, voltage divides between the two regions as



- |   |   |
|---|---|
|  Droplet       |  Hydrophobic |
|  Dielectric    |  Electrode   |
|  Base Material |   |

**Figure 2.4** Side-view diagrams of the different circuits within (a) wired and (b) coplanar electrowetting setups.

$$U_a = \frac{A_r}{A_a + A_r} U, U_r = \frac{A_a}{A_a + A_r} U, \quad (2.7)$$

where  $U_a$  and  $U_r$  are the voltage drops across the dielectric layer where a droplet covers active and reference electrodes, respectively. As a result of the voltage division through a coplanar device, higher input voltages are required to achieve the same degree of electrowetting as in a wired device with the same dielectric layer.

Since voltage can vary across a coplanar device, the electrowetting number can also vary when calculated at different positions. A representative electrowetting number ( $EW_A$ ) for the entire droplet area ( $A_t$ ) can be calculated by weighting the electrowetting numbers in the active, reference, and gap regions by their area fraction as<sup>29</sup>

$$EW_A = \frac{\epsilon_0 \epsilon_d}{2d\gamma_{lg}} \left( \frac{A_a}{A_t} U_a^2 + \frac{A_r}{A_t} U_r^2 + \frac{A_g}{A_t} U_g^2 \right), \quad (2.8)$$

where  $A_g$  is the total area of gaps between electrodes covered by the droplet ( $A_g = A_t - A_a - A_r$ ) and  $U_g$  is the voltage drop through the dielectric layer in the gap regions. This can be reduced to

$$EW_A = \frac{\epsilon_0 \epsilon_d}{2d\gamma_{lg}} \left( \frac{A_a A_r}{(A_a + A_r) A_t} \right) U^2 = \frac{\epsilon_0 \epsilon_d}{2d\gamma_{lg}} \alpha_A^2 U^2, \quad (2.9)$$

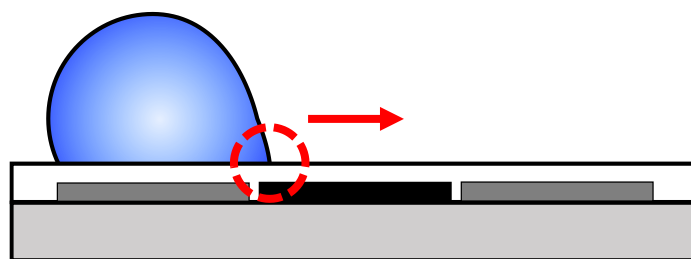
since voltage divides only over the active and reference electrode regions ( $U_g = 0$ ).

The reduced formulation of  $EW_A$  resembles the general electrowetting equation for a single-electrode device, but it includes an additional coefficient based on the electrode geometry. This ‘‘area factor’’ ( $\alpha_A$ ) describes how effectively the input voltage is applied over the entire droplet area. The same droplet on a similarly coated single-electrode device would achieve an identical electrowetting number at a voltage  $\tilde{U}_A$  where

$$\tilde{U}_A = \alpha_A U. \quad (2.10)$$

The area factor has a theoretical maximum value of  $\max(\alpha_A) = 0.5$  when no gaps are present and the droplet area covers active and reference electrode areas equally. In this ideal case, the active and reference electrode areas evenly split the input voltage and the entire droplet region is actuated at 50%. However, gaps are necessary in real devices to isolate different electrodes, and some electrodes may be left inactive. Practically speaking, this “dead space” limits the maximum achievable  $Ew_A$  before reaching saturation.

The droplet deformation caused by electrowetting is used in many 2D DMF devices as a means for inducing horizontal droplet motion.<sup>14,15,26</sup> When a droplet is positioned over multiple electrodes and only one is activated, only a portion of the droplet experiences electrowetting (Fig. 2.5). This can result in the reduction of the apparent contact angle on one side of the droplet while the other side remains relatively unaffected. The change in curvature along the droplet surface results in a pressure gradient across the droplet that drives it toward the active electrode at speeds on the order of centimeters per second.<sup>26</sup> Devices are designed such that droplets centered over one electrode will overlap adjacent



-  **Droplet**
-  **Active Electrode**
-  **Inactive Electrode**

**Figure 2.5** Partial electrowetting pulls a droplet toward an active electrode.

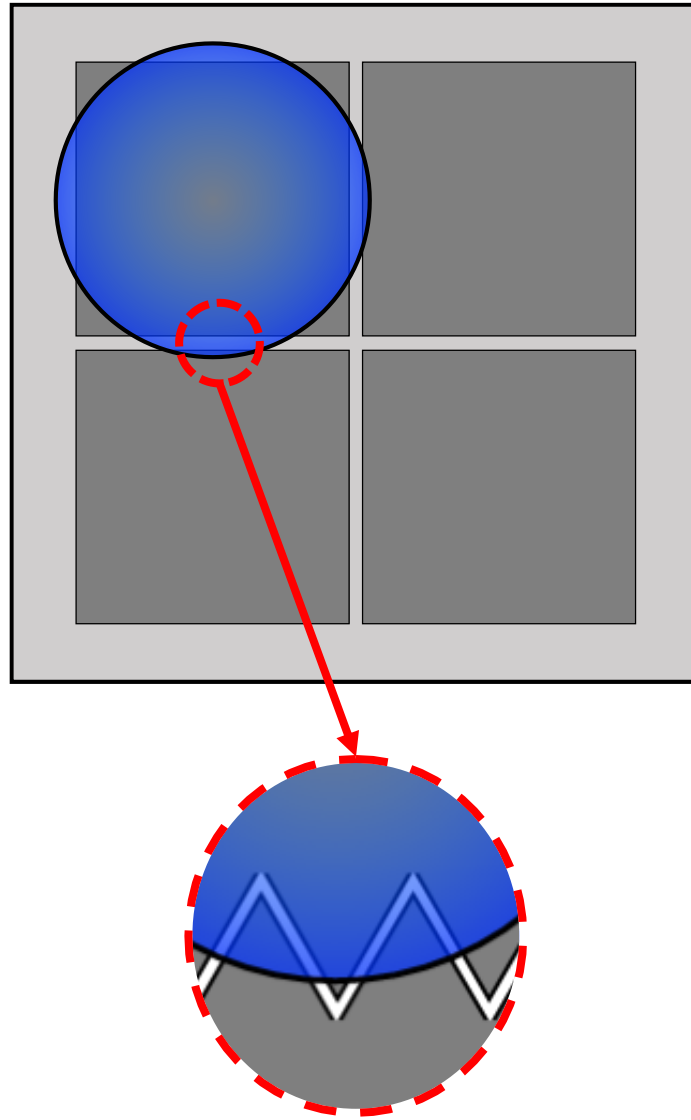


**Figure 2.6** Electrodes in a DMF device are sized to allow a droplet to cover adjacent positions. Interdigitations can also be included to ensure overlap.

electrodes should movement in those direction be desired. Unusual electrode shapes and small interdigitations along the electrode borders can be used to ensure coverage (Fig. 2.6). Sequential movements can be performed to move, merge, and mix droplets as needed for different biological protocols.<sup>7,16-20</sup>

## 2.2 Electrowetting-Induced Droplet Ejection

The electrowetting equation (Eq. 2.6) can be used to predict the steady-state shape of a droplet subjected to electrowetting, but the electrowetting response also has a dynamic component.<sup>31–34,38,39,56,64,69–71</sup> When an actuation signal is applied to a device, the dielectric layer charges in a matter of microseconds.<sup>38</sup> The reduced effective surface energy at the device surface causes the contact line of the droplet to spread, and over the next several milliseconds the entire droplet takes a new shape. For millimeter-size aqueous droplets, the spreading response is typically underdamped (Fig. 2.7).<sup>56,64,71</sup> The dynamics of an underdamped droplet are such that the inertia from actuation allows it to overshoot the predicted steady-state position to achieve a maximally spread position at time  $t_s$ . This time is proportional to  $L^{3/2}$ , where  $L$  is a characteristic length of the droplet, such as the

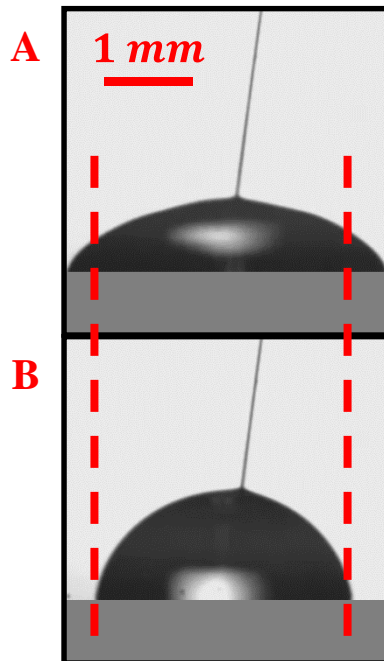


**Figure 2.7** A  $5 \mu\text{L}$  sodium chloride droplet actuated beyond saturation voltage (a) after approximately  $7 \text{ ms}$  and (b) after several seconds. The droplet overshoots its steady-state position.<sup>35</sup>

radius of curvature ( $R$ ).<sup>64</sup> For aqueous droplets where inertial and surface tension forces dominate over viscous and frictional forces, like those examined in this work, the spreading time can be approximated as half of the dominant natural oscillation period of a hemispherical droplet.<sup>64</sup> This is expressed as

$$t_s \approx \sqrt{\frac{3\pi\rho V}{16\gamma_{lg}}}, \quad (2.11)$$

where  $\rho$  and  $V$  are the density and volume of the droplet, respectively.<sup>64</sup> As droplets become smaller or more viscous, spreading times increasingly deviate from this estimate and the electrowetting response becomes overdamped.<sup>71</sup>

Electrical signals tuned to the spreading response of an underdamped droplet can take advantage of the transient response to manipulate the droplet in new ways. Vertical distortions can be created that are sufficient to bridge a droplet to a nearby substrate.<sup>31,32</sup> Droplets can also be ejected from a substrate entirely. Tuned AC<sup>69</sup> and DC<sup>39,56,64</sup> signals have achieved ejection in air from both superhydrophobic<sup>39,69</sup> and hydrophobic<sup>56,64</sup> surfaces. These manipulations can be used in a 3D DMF devices as a means to transfer droplets between two opposing open DMF substrates.

In the case of DC electrowetting-induced droplet ejection, as is examined here, ejection is achieved by applying a sufficient voltage for a time of precisely  $t_s$ .<sup>38,56</sup> A previous model predicting the minimum voltage threshold is discussed in the following section. Actuation for  $t_s$  allows a droplet to reach its most spread state and maximize its surface energy (Fig. 2.8). When actuation stops, the apparent contact angle quickly changes back toward its initial value and causes the contact line to recoil towards its unactuated position.<sup>38</sup> Vertical elongation is induced as a capillary wave travels from the contact line toward the apex of the droplet.<sup>56</sup> This conversion of excess surface energy into kinetic

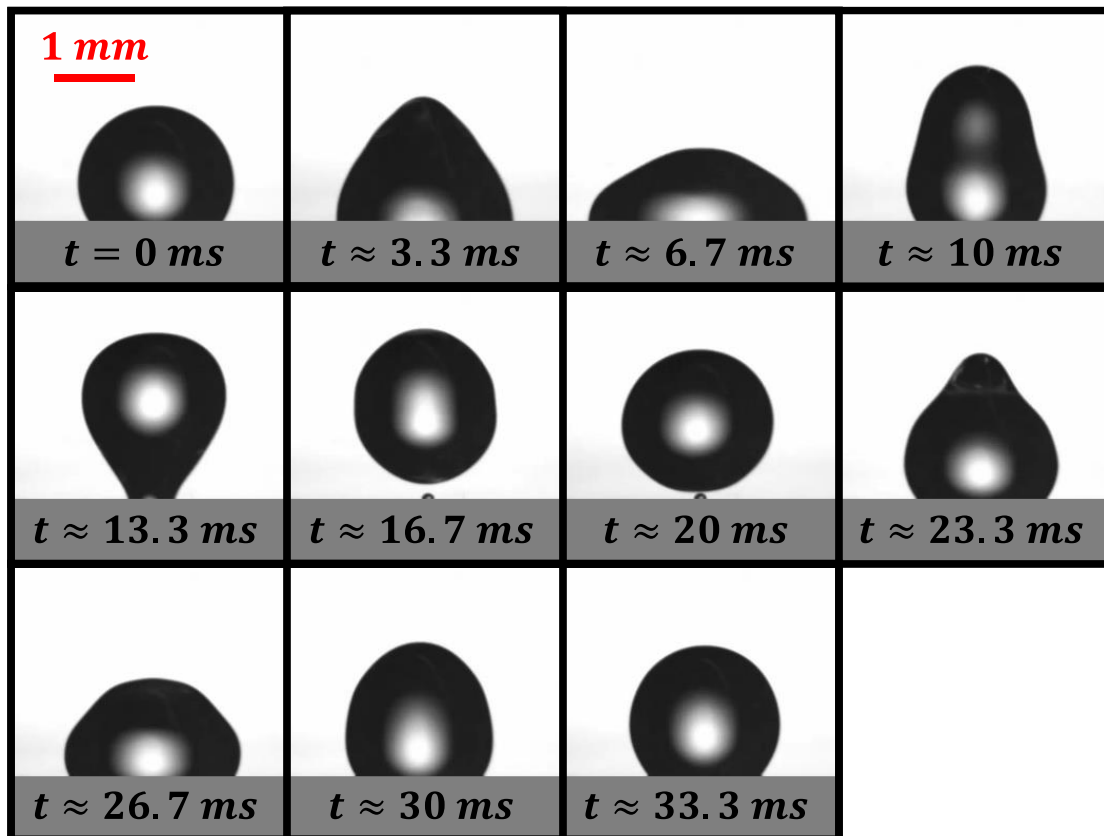


**Figure 2.8** A  $3 \mu\text{L}$  sodium chloride droplet at various times ( $t$ ) throughout electrowetting-induced droplet ejection in air.<sup>57</sup>

energy can be sufficient for detachment from hydrophobic surfaces in air<sup>56</sup> as well as oil.<sup>33,34</sup>

### 2.3 Ejection Threshold

The critical electrowetting number for electrowetting-induced droplet ejection ( $Ew_{\text{cr}}$ ) has previously been estimated using an adhesion model.<sup>56</sup> In order to achieve droplet ejection, this model asserts the electrical energy per area stored in the charged dielectric layer during actuation must exceed the adhesion work per area necessary to

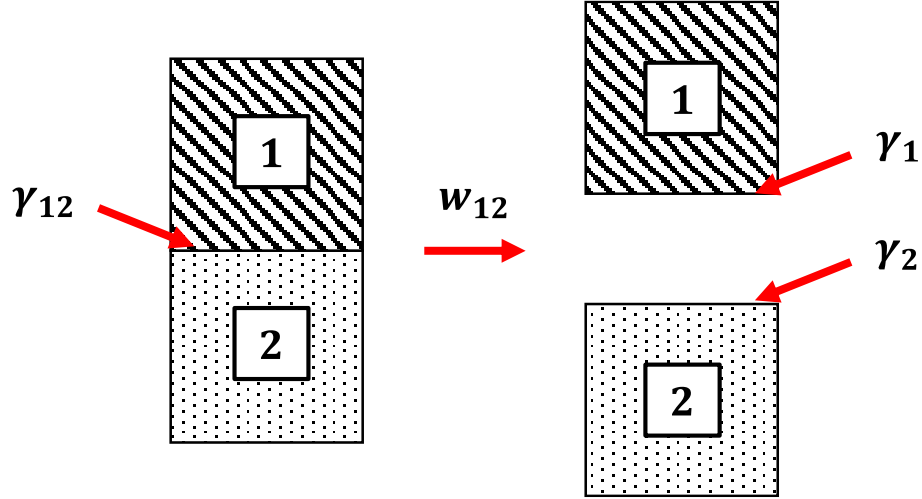


**Figure 2.9** The work to separate two surfaces can generally be expressed as a change in surface energies.

separate the droplet-surface interface. This assumes energy changes along other interfaces as the droplet separates are negligible and no other significant energy changes occur.

The work per area ( $w_{12}$ ) required to separate two phases with interfacial surface energy  $\gamma_{12}$  can generally be expressed as

$$w_{12} = (\gamma_1 + \gamma_2) - \gamma_{12}, \quad (2.12)$$

where  $\gamma_1$  and  $\gamma_2$  are the surface energies of the individual phases (Fig. 2.9). In the case of a droplet on an open DMF device, the solid phase ( $\gamma_1 = \gamma_{sg}$ ) and liquid phase ( $\gamma_2 = \gamma_{lg}$ ) contact at the solid-liquid interface ( $\gamma_{12} = \gamma_{sl}$ ). Using Young's equation (Eq. 2.2), the work per area to separate the liquid droplet from the solid substrate surface ( $w_{sl}$ ) can be expressed as

$$w_{sl} = \gamma_{lg}(1 + \cos \theta_0). \quad (2.13)$$

By equating this work to the energy per area stored in the dielectric layer ( $\gamma_{lg}Ew$ ), the critical electrowetting number for detachment can then be expressed as,

$$Ew_{cr} = 1 + \cos \theta_0. \quad (2.14)$$

An electrowetting number higher than  $Ew_{cr}$  is expected to eject a droplet.

The adhesion model focuses solely on energy changes at the solid-liquid interface. However, changes also occur in the shapes of the solid-gas and liquid-gas boundaries as a droplet ejects from a surface. The interfacial energy model considers changes in interfacial energy along all three of these boundaries.<sup>38</sup> This model asserts that a droplet can only eject from a surface when its total free interfacial energy in the dynamically maximally spread state ( $E_s$ ) exceeds its total free interfacial energy in the ejected state ( $E_{cr}$ ) (Fig. 2.10). This is expressed as

$$\Delta E_{int} = E_{cr} - E_s, \quad (2.15)$$

where  $\Delta E_{int}$  is the net change in total free interfacial energy.

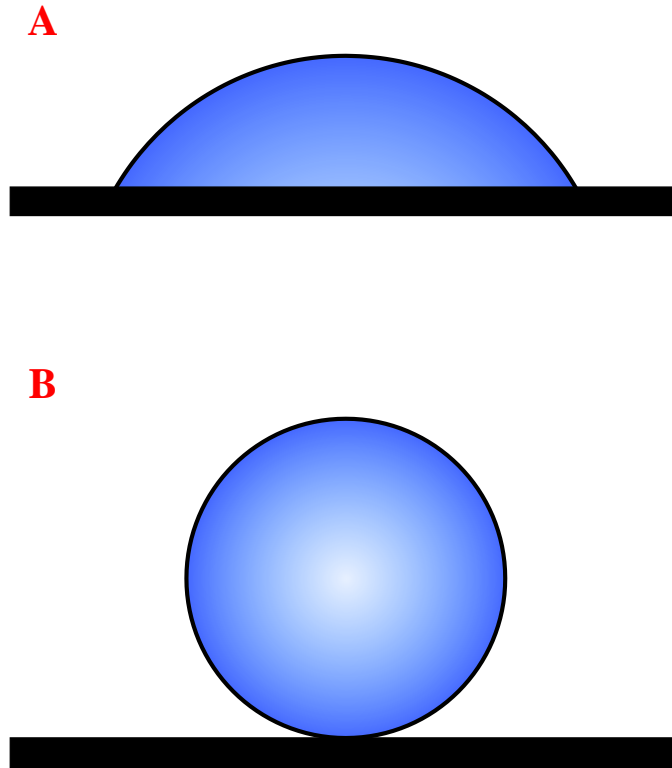


**Figure 2.10** Side-view depiction of a droplet at its (a) maximally spread and (b) detachment threshold positions.

The total free interfacial energy of the spread droplet is expressed as,

$$E_s = E_{s,sl} + E_{s,sg} + E_{s,lg}, \quad (2.16)$$

where  $E_{s,sl}$ ,  $E_{s,sg}$ , and  $E_{s,lg}$  are the interfacial energies along the solid-liquid, solid-gas, and liquid-gas boundaries, respectively. Each of the individual energies is computed as the product of the surface energy of the interface and its area. These can be expressed as

$$E_{s,sl} = \gamma_{sl}(\pi R^2 \sin^2 \theta), \quad (2.17)$$

$$E_{s,sg} = \gamma_{sg}(\pi \hat{R}^2 - \pi R^2 \sin^2 \theta), \quad (2.18)$$

and

$$E_{s,lg} = \gamma_{lg}(2\pi R^2)(1 - \cos \theta), \quad (2.19)$$

where  $\hat{R}$  is an arbitrary radius of the cylindrical system domain larger than  $R$ . The shape of the droplet in its ejected state is assumed to be a sphere tangent to the surface. In this threshold position, the solid-liquid boundary has no area. The total interfacial energy is expressed as

$$E_{cr} = \gamma_{lg}(4\pi R_{sph}^2) + \gamma_{sg}(\pi \hat{R}^2), \quad (2.20)$$

where  $R_{sph}$  is the radius of a sphere with the same volume as the droplet. The net change in total free interfacial energy can then be expressed as,

$$\Delta E_{int} = 4\pi\gamma_{lg}R_{sph}^2 - 2\pi\gamma_{lg}R^2(1 - \cos \theta) + \pi\gamma_{lg}R^2 \cos \theta_0 \sin^2 \theta. \quad (2.21)$$

Droplet ejection is expected when  $\Delta E_{int} < 0$ .

## 2.4 Droplet Ejection in Air

All experiments in this work are performed in an air medium. An oil medium has the advantage of reducing surface adhesion which can reduce operating voltage.<sup>14,25–27</sup>

However, it also inhibits evaporation. While this can at times be beneficial for reducing biofouling,<sup>14,25,28</sup> some applications depend on evaporation to deposit suspended particles on a substrate.<sup>20,72,73</sup> Oil also limits the droplet compositions available for use since a selected carrier fluid must be oil-immiscible, and it runs the risk of adsorbing analytes from working droplets.<sup>19,73,74</sup> Thus in several circumstances an air medium is preferable.

Only a small number of previous investigations have focused on electrowetting-induced droplet ejection in an air medium.<sup>31,32,56</sup> Successful ejection using DC actuation has been demonstrated using both single-electrode devices in a wired configuration and a multi-electrode coplanar devices.<sup>56</sup> In the wired configuration, droplets from  $0.4 \mu L$  to  $10 \mu L$  in volume were ejected and found to have similar threshold voltages. However, thresholds were approximately 15% higher than the value predicted by the adhesion model. This suggests other factors may be at play that the adhesion model does not consider.

The successful coplanar DC electrowetting-induced ejection was performed on a device with an interdigitated finger electrode design.<sup>56</sup> Actuation on this design resulted in asymmetric droplet deformation (Fig. 2.11) which wasted energy on azimuthal oscillations after release. Successful ejection required the use of a modified signal. Two pulses spaced  $t_s$  apart were sent to give the droplet an initial perturbation. The asymmetric wetting and significant dead space beneath the droplet were cited as limiting factors for detachment on the coplanar design used. Other coplanar electrode geometries have not been examined for droplet ejection.

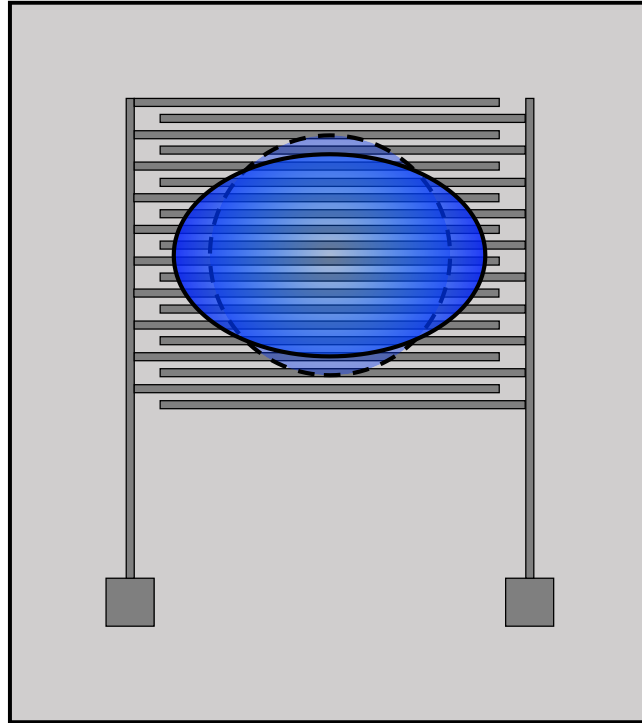


**Figure 2.11** Top-view diagram of an interdigitated finger electrode design like that previously used for coplanar electrowetting-induced droplet ejection in air.<sup>56</sup> An actuated droplet tends to deform asymmetrically along the electrodes.

## 3.0 Experimental Methodology

Electrowetting-induced droplet ejection experiments were performed in each of the investigations presented in the following chapters. The electrowetting devices in those experiments were broadly classified as either “cleanroom fabricated” (CRF) or “inkjet-printed” (IJP) based on how the electrodes of the device were formed. This chapter details both fabrication processes and how the finished electrowetting devices were used.

Material presented here has previously been published in *Langmuir*,<sup>35</sup> published in *Microfluidics and Nanofluidics*,<sup>37</sup> and submitted for publication in *Sensors and Actuators A: Physical*.<sup>36</sup>

### 3.1 Cleanroom-Fabricated (CRF) Devices

Electrodes on CRF devices were fabricated in the cleanroom facilities of the Semiconductor and Microsystems Fabrication Laboratory at the Rochester Institute of Technology. A naming convention was used to distinguish different designs from one another, since a number of different designs were fabricated. Specific device types were identified based on number of ejection pad segments and electrode spacing in addition to fabrication technique. For example, cleanroom-fabricated devices with four ejection pad segments and an electrode spacing of  $20\ \mu\text{m}$  were identified as “CRF4-20” devices. Single-electrode devices were identified simply as “CRF1” devices since ejection was performed on an unsegmented electrode and the electrode spacing metric was not applicable.

A commercially available clear borosilicate float glass microscope slide ( $50 \times 75 \times 1.1\ \text{mm}$ ) was used as a base material for most devices (Deposition Research

Lab, Inc.). These slides were available pre-coated with  $\sim 100\text{ nm}$  of aluminum which served as the conductive layer. For CRF devices used in Chapter 6, plain glass microscope slides (Corning) were used as a base material. These were cleaned in piranha solution and then sputter coated with approximately  $1\ \mu\text{m}$  of aluminum to form the conductive layer.

The conductive layer was left intact for all single-electrode devices. For all multi-electrode coplanar devices, the metal layer was patterned using a traditional photolithography process. Photomasks of the desired electrode geometries were produced prior to processing for use during the exposure stage. Electrode geometries were first drawn in AutoCAD software. Electrode spacings were drawn  $5\ \mu\text{m}$  wider than intended to compensate for sizing bias observed in preliminary devices. Photomasks of each electrode geometry were then printed by CAD ART Services, Inc. at  $25,400\ \text{dpi}$  and a feature precision of  $\pm 2\ \mu\text{m}$ . Electrodes in the photomasks appeared as opaque black.

The photomask for a single device included up to eight sets of ejection electrodes. Ejection electrodes were comprised of an ejection pad where the droplet was positioned during testing and contact pads for electrical access wired off toward the edge of the device. Electrodes were radially symmetric to allow for more radially uniform wetting during actuation. Each ejection pad consisted of a  $6\ \text{mm}$  circular electrode region divided into four, six, or eight radially symmetric segments (Fig. 3.1). Opposite segments were connected by either an outer ring or through the center. Only four, six, or eight primary gap lines were required, as determined by the number of segments. Gap widths between electrodes were  $20\ \mu\text{m}$ ,  $55\ \mu\text{m}$ , or  $200\ \mu\text{m}$ . The intent of this ejection pad design was to address issues of asymmetric wetting and excess dead space which were previously noted to limit detachment from devices with coplanar interdigitated finger electrodes.<sup>56</sup>

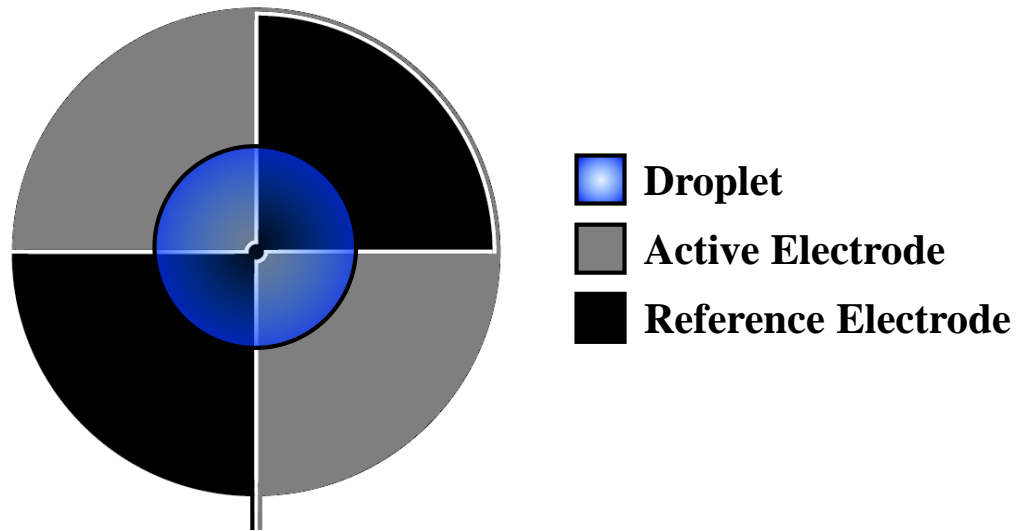


**Figure 3.1** Top-view diagram of the radially symmetric ejection pad design used in a CRF4 device. Gaps and wiring are enlarged for visibility. A  $10\ \mu\text{L}$  droplet is shown for scale.<sup>35</sup>

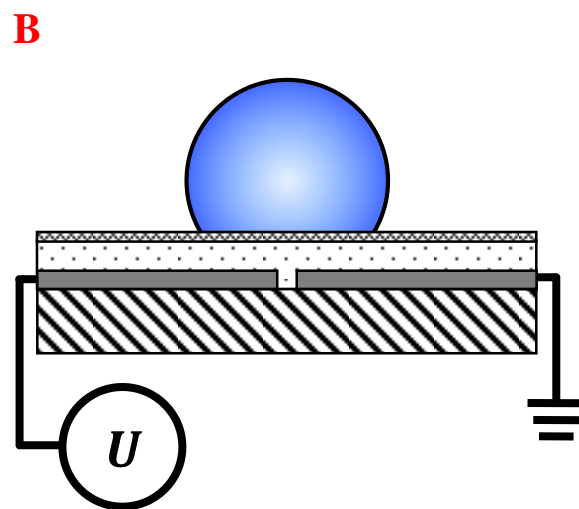
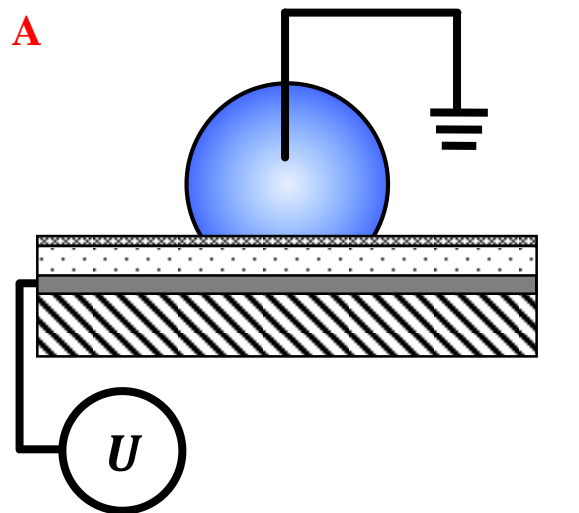
Electrode patterning in the cleanroom facilities began with coating the metal layer of the devices in photoresist. A  $\sim 1\ \mu\text{m}$  layer of AZ MiR 701 positive tone photoresist was applied via spin coating at  $3000\ \text{rpm}$  for  $40\ \text{s}$ . Devices were then soft baked at  $90\ ^\circ\text{C}$  for 1 minute prior to exposure. A Suss MA150 Contact Aligner loaded with an *i*-line filter was used to expose the photoresist coating to a  $220\ \text{mJ}/\text{cm}^2$  dose of ultraviolet light. A photomask was taped to a transparent glass cover plate and positioned directly against devices during exposure to prevent exposure in the intended electrode regions. A post exposure bake was then performed at  $115\ ^\circ\text{C}$  for 1 minute.

Exposed devices were then developed using a manual process. Devices were placed in a bath of CD-26 developer for 1 minute while lightly agitated to remove all exposed photoresist. Devices were then washed with deionized (DI) water to remove excess developer. Excess DI water was subsequently removed via nitrogen spray. At this point the

remaining unexposed photoresist pattern could be seen with the naked eye. Devices were visually inspected for obvious defects and then hard baked at 140 °C for 1 minute.

Excess aluminum was removed using a chemical wet etch process. A bath of Fujifilm 16:1:1:2 aluminum etch was warmed to 40 °C. Devices were submerged in the etching solution for 2 minutes and then moved to a flowing DI water bath for 5 minutes. Unexposed photoresist was then stripped away to leave only the desired electrodes. Two baths of Baker PRS-2000 photoresist stripper were warmed to 90 °C. Devices were submerged in one bath of stripper solution for 5 minutes and then moved to the second bath for 5 minutes. Stripped devices were then moved to a flowing DI water bath for 5 minutes. The final patterned devices were then dried. A nitrogen spray gun was used to remove the bulk of the DI water. Remaining moisture was then removed by baking devices at 140 °C for 1 minute.

Two additional polymer layers were then spin coated over finished electrodes outside the cleanroom facilities using a Laurell WS-650-23 spin coater (Fig. 3.2). A dielectric layer of SU-8 3005 photoresist (PR) was first applied directly over the electrode layer. This was done using a two-stage coating process: 500 *rpm* for 10 *s* then 4000 *rpm* for 30 *s*. An acceleration of 300 *rpm/s* was used between stages. Devices were then soft baked at 95 °C for 2.5 minutes. An Electro-Lite EC-500 curing chamber equipped with a 365 *nm* ultraviolet lamp was then used to cure the photoresist. Devices were exposed in the chamber for 30 *s* and then hard baked at 150 °C for 3 minutes. Coating thickness was ~5  $\mu\text{m}$  and verified via profilometry (Tencor P2). A final layer of Teflon AF 1601 ~100 *nm* thick was then applied to increase the hydrophobicity of the outermost device surface. This was done in a single spin coating stage at 2000 *rpm* for 1 minute followed



- |   |   |
|---|---|
|  NaCl Solution |  Teflon AF |
|  SU-8 3005     |  Aluminum  |
|  Glass         |   |

**Figure 3.2** Side-view diagrams of the layers in the (a) wired and (b) coplanar CRF devices used.

by a hard bake at 160 °C for 10 minutes. Initial contact angles ( $\theta_0$ ) on finished devices were  $\sim 120^\circ$  and verified via goniometry (Ramé-Hart model 250).

A crude liftoff process was used to leave small portions of the aluminum layer exposed after SU-8 and Teflon AF spin coating. The edges of each device were masked with adhesive Kapton tape before spin coating. Kapton tape remained in place until all coating was complete. Polymers coated over the masked area were then lifted off by slowly removing the Kapton tape. This permitted direct electrical access to the electrodes during later experimentation.

### **3.2 Inkjet-Printed (IJP) Devices**

Electrodes on IJP devices were produced without the need of cleanroom facilities using a low-cost inkjet printing process based on a previously described process by Dixon et al.<sup>18,50</sup> Printing was done using a commercially available Epson Stylus C88+ desktop inkjet printer ( $\sim$ \\$120 USD) (Fig. 3.3). The stock ink cartridges were replaced with cartridges of silver nanoink (Metalon JS-B25P) to produce conductive printed features. Transparent sheets of treated polyethylene terephthalate (PET) film (Novele) were loaded into the paper feed and served as a flexible base material for printed devices.

Electrode designs were drawn in Adobe Illustrator and printed directly onto the PET film without the need for patterning. Up to twelve individual designs were printed per sheet and then allowed to cure at room temperature for approximately 24 hours. Printed devices used for ejection experiments in Chapter 6 were all single-electrode designs. These were referred to as “IJP1” devices. Printing was done using the settings in Table 3.1 and with silver ink loaded into the black, cyan, and magenta nozzles of the printer. Yellow ink

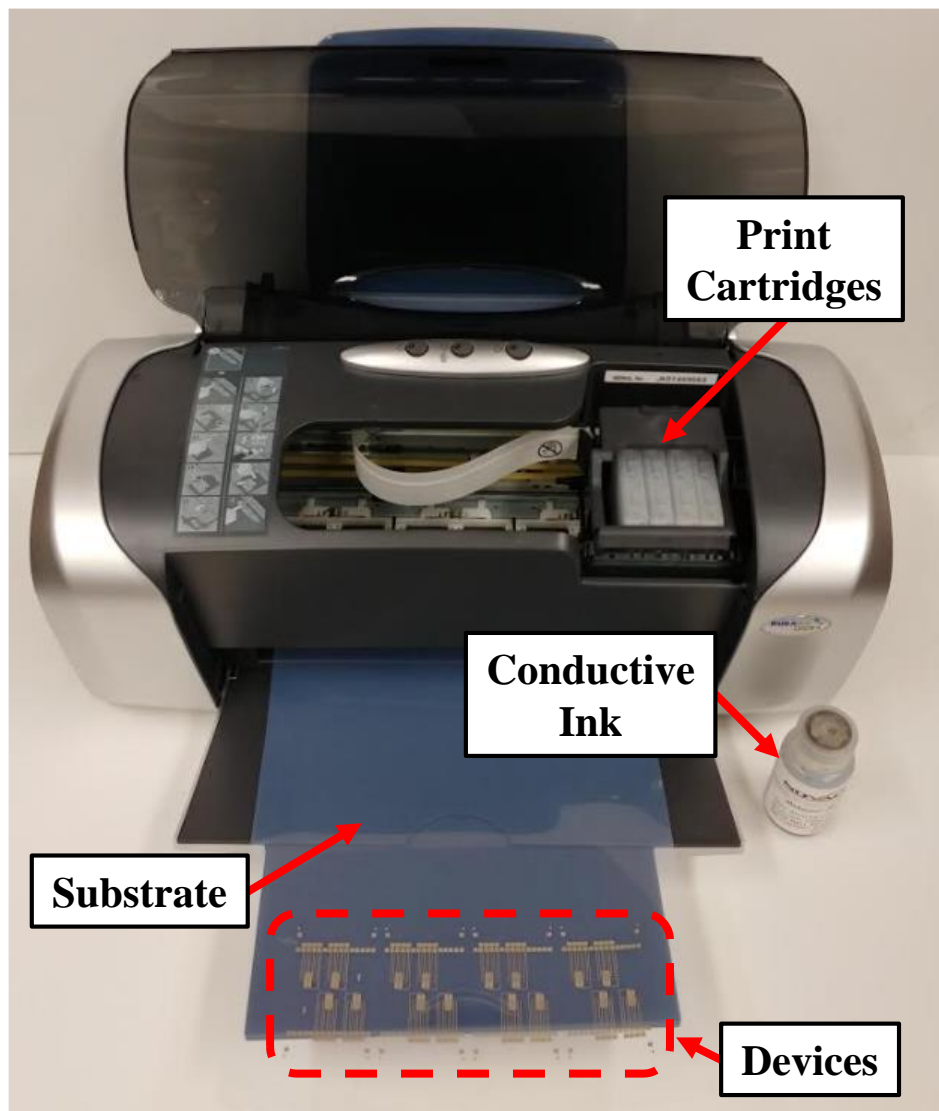


**Figure 3.3** Experimental facility for low-cost fabrication of electrodes by inkjet printing.

was loaded into the yellow nozzle. Later printing with the inkjet system to produce multi-electrode designs was done in grayscale mode with the “Paper” setting set to “Matte – Heavyweight” and silver ink loaded into the black nozzle only (Table 3.2). These changes helped minimize the impact of nozzle clogging when printing more complex features as the black nozzle was larger than the three color nozzles. The minimum feature size and

**Table 3.1** Initial printer settings used for IJP electrode fabrication and nozzle cleaning<sup>37</sup>

Parameter	Setting
Grayscale	Off
High Speed	Off
Print Quality	Best Photo
Paper Type	Ultra Glossy

**Table 3.2** Later printer settings used for IJP electrode fabrication and cleaning to improve printer longevity

Parameter	Setting
Grayscale	On
High Speed	Off
Print Quality	Best Photo
Paper Type	Matte - Heavyweight

spacing between features that could reliably be produced with these settings were  $\sim 100 \mu\text{m}$  and  $\sim 200 \mu\text{m}$ , respectively.

Individual electrode designs were cut out and affixed to glass slides using Kapton tape to provide a rigid base for spin coating. Printed electrodes were first spin coated with a layer of Teflon  $\sim 100 \text{ nm}$  thick (Fig. 3.4). They were then subsequently coated with a layer of SU-8 3005 photoresist and final layer of Teflon similar as was done on CRF devices. The extra Teflon layer directly over the electrodes served to separate the photoresist from the PET substrate. The photoresist and PET reacted when in contact and changed from translucent to an opaque white color. Such devices exhibited dielectric

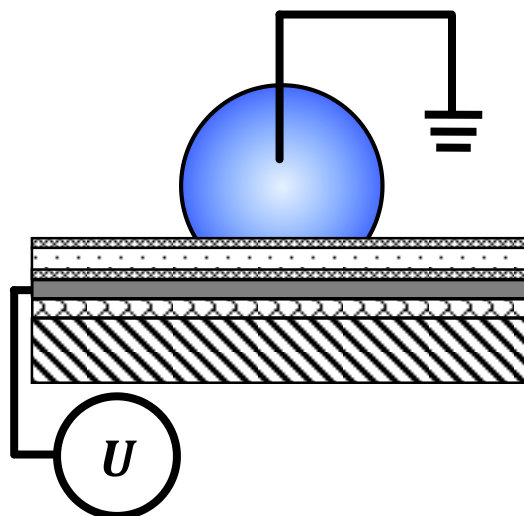


**Figure 3.4** Side-view diagram of the layers in the wired IJP devices used.

breakdown at low voltages and could not be used for experimentation. The hydrophobicity of the extra Teflon layer also resulted in a thinner SU-8 layer as detailed in Chapter 6.

To improve the longevity of the printing system and reduce the frequency of clogging, excess silver ink in the printer was purged at the end of each printing session. This was done by first loading all nozzles of the printer with a diluted cleaning solution. The stock cleaning solution consisted of glycerin, ammonia ( $\sim 1 M$ ), and isopropyl alcohol in a 1:2:10 ratio. This was diluted with three parts of DI water per one part cleaning solution. A pattern of black, cyan, magenta, and yellow squares was then repeatedly printed until the resulting sheets were damp with the cleaning solution and no ink was visible. This ensured that nozzles were unclogged and no excess metal remained.

**Table 3.3** Estimated electrode fabrication costs for a batch of eight CRF or eight IJP devices

CRF Process	Processing Cost	IJP Process	Component Cost
Al-Coated Slides	\$120.00	Blank Slides	\$3.00
Photoresist Spin Coat	\$29.21	PET Substrate	\$0.50
Exposure	\$28.95	Conductive Ink	\$10.00
Development (Manual)	-	Kapton Tape	\$0.10
Etch and Photoresist Strip	\$90.00		
Batch Cost	\$268.16	Batch Cost	\$13.10
Device Cost	\$33.52	Device Cost	\$1.64

This inkjet process allows for the fabrication of device electrodes at a greatly reduced cost as compared to the cleanroom fabrication process. Processing costs alone are reduced by approximately 95% (Table 3.3). For CRF devices, costs shown for the different processes in the SMFL account for the operation and maintenance of the equipment used, including any necessary chemicals or other consumables. Bench space and chemicals for development were freely provided. For IJP devices, all processing is done in one printing step and all necessary materials were purchased individually. Costs for each fabrication method do not reflect the startup expenses associated with buying an inkjet printer versus setting up a cleanroom facility stocked with equipment and chemicals.

### 3.3 Ejection Setup

Experiments generally consisted of depositing a droplet onto an electrowetting device, sending an actuation signal, and recording the resulting droplet behavior.

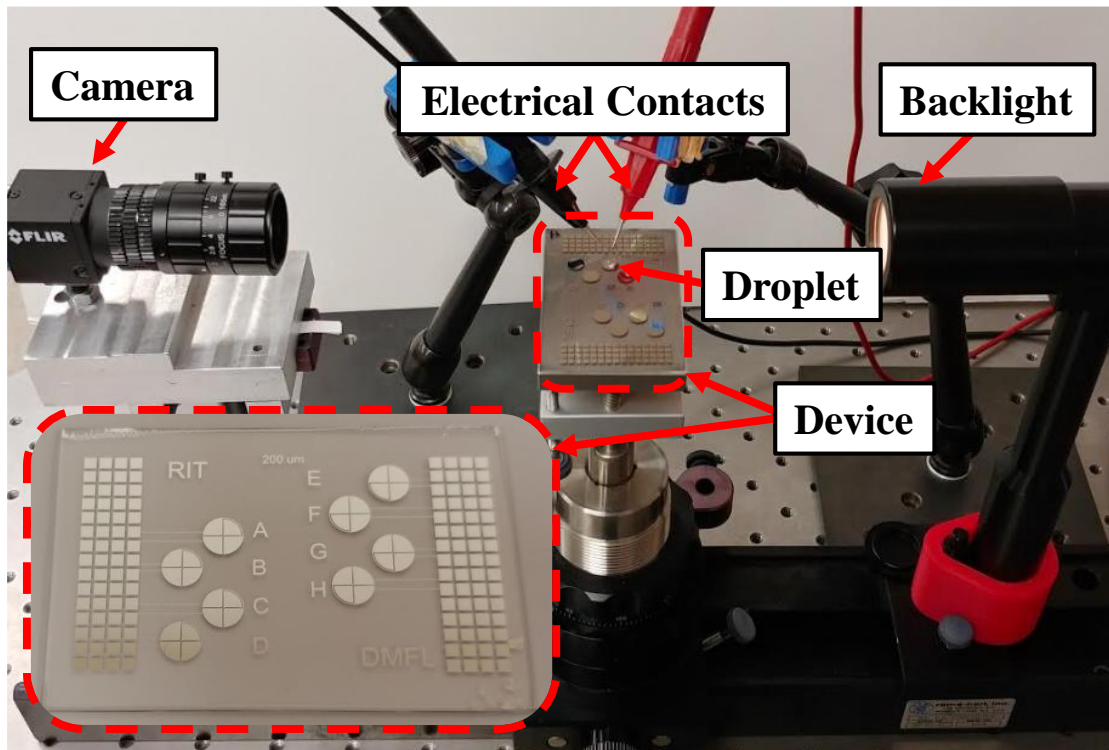


**Figure 3.5** Experimental facility used to perform electrojetting-induced droplet ejection.<sup>57</sup>

Electrojetting devices were positioned on an adjustable Ramé-Hart stage for all ejection experiments (Fig. 3.5). All droplets were manually deposited using single-channel micropipettes (Eppendorf Research® Plus Medium Gray and Eppendorf Research® Plus Yellow). Droplets ranged in volume from 3 to 15  $\mu\text{L}$  and were drawn from a 1  $\text{mM}$  salt solution of NaCl in DI water. The total error in droplet volume for the range used was  $\sim 3\%$  as reported by the pipette manufacturer.<sup>75</sup>

Actuation signals were produced using a National Instruments PXI-5402 signal generator and Trek PZD700A amplifier. Devices were connected to the actuation system in one of two ways depending on the design of the electrojetting device being tested. On single-electrode wired devices, a probe tip was connected to the active wire leading from

the amplifier and positioned in contact with exposed metal of the electrowetting device. An alligator clamp was connected to the reference wire leading from the amplifier and loaded with a  $22\ \mu\text{m}$  tungsten wire. This tungsten wire was then inserted into the droplet from above to ground it during actuation. On multi-electrode coplanar devices, probe tips were connected to both wires and positioned against the exposed contact pads of the ejection electrodes in use.

Actuation signals were square waves oscillating between zero and some active voltage depending on the current test. When calculating  $Ew$  values, only the voltage during the active signal time was considered. Pulse durations were tuned to match the spreading time ( $t_s$ ) of the current droplet. Spreading times for 3, 5, and 10  $\mu\text{L}$  droplets under DC electrowetting were previously reported to be 5.3, 7, and 9  $\text{ms}$ , respectively.<sup>56</sup> General spreading times were known to be proportional to the 1.5<sup>th</sup> power of the characteristic length of the droplet<sup>64</sup> or equivalently the square root of its volume. By fitting all reported times to this relationship, spreading times for 7, 12, and 15  $\mu\text{L}$  droplets were calculated to be 7.8, 10.1, and 11.3  $\text{ms}$ , respectively. For most trials, the duty cycle of the signal was configured to allow  $19t_s$  between pulses. This allowed the droplet to settle so the effects of each individual pulse could be observed. Signals for the trials in Chapter 6 used a 50% duty cycle where the time between pulses was the same as the active time ( $t_s$ ).

Droplets were initially actuated at active voltages too low for ejection. Testing began at 115  $V$  on wired devices and 230  $V$  on coplanar devices. The camera feed of the droplet response was observed in real time for obvious detachment. Droplets were considered to have detached if a gap was visible between the droplet and the substrate. If no such detachment was visible, voltage was stepped up and applied again. Voltage

increased in 5  $V$  increments on wired devices and 10  $V$  increments on coplanar devices. This repeated until detachment was observed or saturation was passed. Due to the timescale of the ejection phenomenon, recorded video of each trial was also reviewed after experimentation to check for detachment. The lowest voltage at which detachment occurred for a given droplet was considered its threshold voltage.

Saturation voltages were determined using a constant DC voltage signal rather than square waves. The steady-state apparent contact angle of an actuated 5  $\mu L$  droplet was measured at a series of increasing voltages. The onset of saturation was identified as the point at which the apparent angle began to deviate from theoretical predictions computed with the electrowetting equation. Saturation was found to begin at  $\sim 140 V$  on single-electrode CRF devices<sup>37</sup> and  $\sim 290 V$  on four-part CRF devices.

### **3.4 Image Capture and Processing**

Droplets were observed from the side during experimentation using one of two imaging systems. Both systems incorporated a Ramé-Hart 100-05-115 fiber optic illuminator backlight which resulted in the observation of a dark droplet profile against a white background. The majority of droplet ejection trials were conducted on a Ramé-Hart model 100-00-115 goniometer stage. Trials were recorded using a 0.4  $MP$  mono Blackfly S camera equipped with a 35  $mm$  Edmund Optics lens. The camera was controlled with SpinView software (FLIR Systems). Videos were recorded at 600  $fps$ , which corresponded to approximately 1.67  $ms$  between consecutive frames. Approximately 3  $s$  of video were recorded at a time. This spanned approximately ten actuation pulses. More pulses were captured for smaller droplets with shorter spreading times ( $t_s$ ).

Trials in Chapter 6 were performed on the stage of a Ramé-Hart model 250 goniometer system and observed with a U1 series camera. Several seconds of video at 40 *fps* were recorded using DROPImage Advanced software. This lower-speed system and DROPImage Advanced were also used when measuring the initial angles of droplets on finished devices and when determining saturation.

Recorded videos were then processed in MATLAB. The individual frames from each video were saved as images and manually checked for detachment. MATLAB was also used to generate slow-motion versions of the recorded videos to observe the droplet detachment phenomenon more clearly. For each ejection experiment performed in Chapter 4, the frame with the widest droplet contact width prior to the first detachment was also identified. These frames were assumed to be the maximum spreading states achieved prior to detachment. The contact radius in each of these images was measured directly. The radii at all other heights within the droplet were also measured and used to compute the height of the center of mass in the spread state by assuming each layer of the droplet was a circular disc.

### **3.5 Electrode Design Analysis**

All electrode designs were analyzed in MATLAB using the image processing toolbox to determine how much of the active and reference electrodes were covered by a droplet positioned over a given design. Analysis was limited to the detachment pad region that a droplet would contact on a device. Simplified versions of only this region were drawn in Adobe Illustrator. These excluded the wiring around the outer ring since the droplet would not cover it. Wiring at the center pad was drawn to consist of straight rectangular

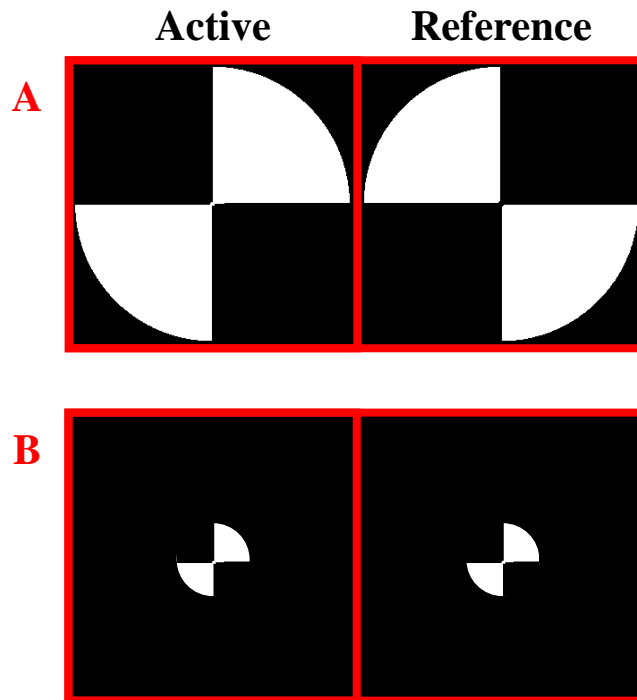


**Figure 3.6** Electrodes identified in the (a) ejection pads and (b) droplet contact regions of a  $5 \mu\text{L}$  droplet ( $\theta_0 \approx 120^\circ$ ) centered on the CRF4-20 design.

wires connecting alternating segments. For designs with  $200 \mu\text{m}$  spacing no central connection was included. Spacings in these drawings were also true to intended size rather than oversized by  $5 \mu\text{m}$  as was done for the photomasks.

The active and reference electrode regions were first identified in each image (Fig. 3.6). An image consisting of a circular region of interest (ROI) with radius  $r$  positioned over the center of the design was then constructed. The size of  $r$  corresponded to the initial contact radius of an unactuated droplet on the hydrophobic surface used ( $\theta_0 = 120.1^\circ$ ). Pixels within the ROI overlapping with an electrode were counted to determine the total active and reference electrode areas covered by a droplet. This process was then repeated several times with the circular ROI offset up to  $1 \text{ mm}$  away from the center of the design.

The lengths of contact line over the active and reference electrodes were determined using a similar process. An image with a ring-shaped ROI was constructed consisting of all points a distance  $r$  from the center of the design. Pixels within the ROI overlapping with an electrode were then counted to determine how much of the droplet perimeter covered each electrode type. This process was also repeated several times with the ring-shaped ROI offset up to  $1\text{ mm}$  away from the center of the design.

## 4.0 Impact of Droplet Size on Ejection

The investigation in this chapter extends the previous electrowetting-induced ejection experiments in air<sup>56</sup> described in Chapter 2. In those experiments, ejection was achieved using a coplanar device, but asymmetric spreading and dead space were both cited as factors limiting successful detachment. Ejection was also achieved in a wired setup, and ejection thresholds for droplets up to 10  $\mu\text{L}$  were reported to be independent of volume. The observed thresholds were significantly higher than expected based on a simple adhesion work model of the energy necessary for detachment. As a droplet separates from a surface, excess surface energy is lost to increase gravitational potential energy as well as separate the solid-liquid interface.<sup>38</sup> The magnitude of the gravitational potential energy change would increase with increasing droplet size since it is directly proportional to droplet mass. However, the resulting impact on the ejection threshold has not been thoroughly examined.

In this investigation, thresholds for electrowetting-induced droplet ejection in air are compared for droplets ranging in volume from 3  $\mu\text{L}$  to 15  $\mu\text{L}$ . The previous models for predicting detachment<sup>38,56</sup> detailed in Chapter 2 are updated to include changes in gravitational potential energy during detachment. Droplets are actuated on cleanroom-fabricated (CRF) electrowetting devices with (i) wired and (ii) coplanar electrode configurations. In the wired configuration, droplets are positioned over a CRF1 device with a large, single electrode and grounded using an inserted tungsten wire. On coplanar devices, droplets are positioned over a CRF4 device with a circular electrode pad divided into four equal regions. Actuation on both device types is performed at increasing voltages

until detachment is observed. Thresholds for all trials across a range of droplet volumes are then compared to thresholds predicted by previous models<sup>38,56</sup> and the updated models developed here. A minimum of eight trials ( $n = 8$ ) are performed for each case. All measurement errors are reported as one standard deviation ( $s$ ) from the mean unless otherwise specified. All coplanar electrowetting numbers here are the effective electrowetting number of the entire droplet contact region as weighted by electrode area ( $EW_A$ ).

The material presented in this chapter has previously been published in *Langmuir*.<sup>35</sup> Reprinted with permission from Burkhart, C. T.; Maki, K. L.; Schertzer, M. J. Coplanar Electrowetting-Induced Droplet Detachment from Radially Symmetric Electrodes. *Langmuir* 2020, 36 (28), 8129–8136. <https://doi.org/10.1021/acs.langmuir.0c01015>. Copyright 2020 American Chemical Society.

## 4.1 Modeling the Ejection Threshold

Lee et al.<sup>56</sup> provided the first estimate for a critical threshold electrowetting number ( $EW_{cr}$ ) for electrowetting-induced droplet detachment using a simple adhesion model. They predicted detachment would occur when electrical energy stored in the dielectric layer exceeded the adhesion energy between the droplet and the surface. This energy difference per unit area can be expressed as the detachment function

$$f_{adh}(EW) = \gamma_{lg}EW - \gamma_{lg}(1 + \cos \theta_0), \quad (4.1)$$

where  $EW$  is the electrowetting number,  $\gamma_{lg}$  is the surface tension along the liquid-gas interface, and  $\theta_0$  is the initial contact angle of the droplet. For the devices examined here, the initial contact angle was measured to be  $120.1^\circ \pm 0.8^\circ$ . The critical electrowetting

number for detachment predicted by the adhesion model ( $Ew_{cr,adh}$ ) occurs at the root of this function,  $f_{adh}(Ew_{cr,adh}) = 0$ .

While the adhesion model<sup>56</sup> offers a simple analytical tool to estimate the critical electrowetting number for detachment, it neglects changes in the energies of the solid-liquid and solid-gas interfaces. Cavalli et al.<sup>38</sup> provided an updated model that accounted for changes in all three interfaces by computing the difference in total free interfacial energy ( $\Delta E_{int}$ ) between the maximally spread position and a critically detached position tangent to the surface (Fig. 4.1). This can be expressed in terms of actuated apparent contact angle ( $\theta_U$ ) as

$$\Delta E_{int} = 4\pi\gamma_{lg}R_{sph}^2 - 2\pi\gamma_{lg}R^2(1 - \cos \theta_U) + \pi\gamma_{lg}R^2 \cos \theta_0 \sin^2 \theta_U, \quad (4.2)$$

where  $R_{sph}$  is the radius of a sphere with the same volume as the droplet and  $R$  is the radius of curvature of the droplet. This interfacial model predicts droplet ejection when detachment is energetically favorable ( $\Delta E_{int} < 0$ ).

The interfacial model<sup>38</sup> can also be used to predict a critical electrowetting number for droplet detachment ( $Ew_{cr,int}$ ) by approximating a droplet's maximally spread shape as its steady-state spherical cap shape. Sufficiently small droplets reach a steady-state position after actuation described by the electrowetting equation,

$$\cos \theta_U = \cos \theta_0 + Ew. \quad (4.3)$$

The spherical cap assumption is suitable for droplets small enough that their shape is largely determined by surface tension and minimally deformed by gravitational forces. The Bond number ( $Bo$ ) describes the ratio of these forces. For all droplets examined here,  $Bo$  is less than 1, indicating surface tension exceeds gravitational force and a spherical cap is a reasonable approximation for droplet shape (Table 4.1).<sup>58</sup>

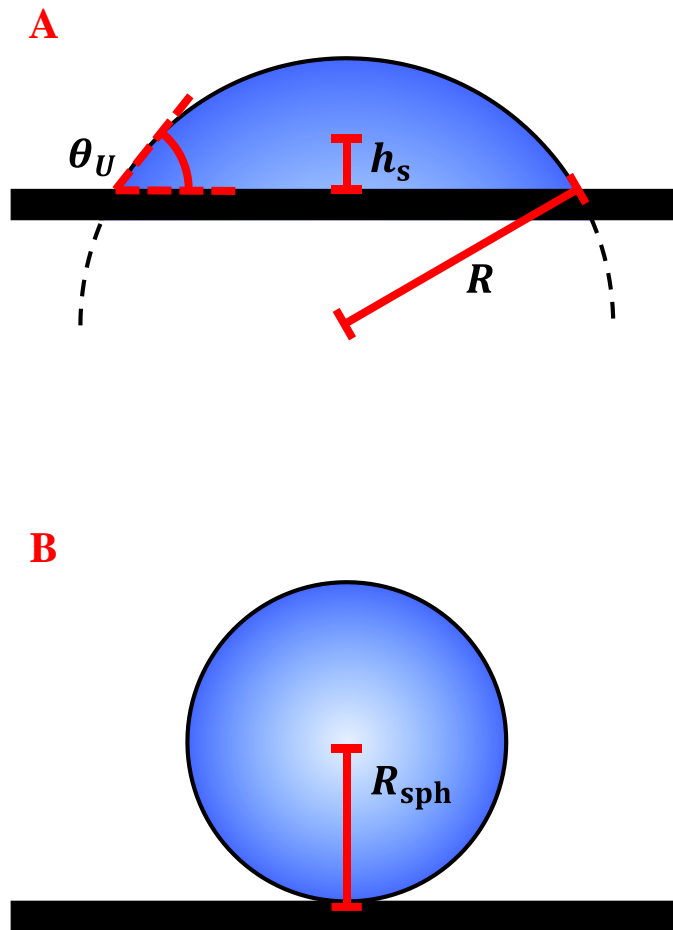


**Figure 4.1** Approximated shape of a droplet at its (a) maximally spread and (b) detachment threshold positions. The quantities  $h_s$  and  $R_{sph}$  denote the distance from the droplet's center of mass to the substrate in the spread and threshold positions, respectively.<sup>35</sup>

The steady-state shape approximation will still underpredict spreading as the droplet's dynamic contact line is known to overshoot the steady-state geometry used.<sup>64</sup> Measurements made in captured frames of maximally spread droplets from the experiments performed later in this chapter show underprediction worsens with increasing droplet volume (Table 4.2). In all cases, the steady-state contact radius is less than the maximally spread contact radius. However, this approximation allows the total free interfacial energy

**Table 4.1** Bond numbers for a droplet in air on a Teflon surface ( $\theta_0 = 120.1^\circ$ )<sup>35</sup>

Volume	Bond Number (–)
3 $\mu L$	0.18
5 $\mu L$	0.26
7 $\mu L$	0.32
10 $\mu L$	0.41
12 $\mu L$	0.46
15 $\mu L$	0.53

**Table 4.2** Deviations in droplet geometry at maximum spreading<sup>35</sup>

Volume	Deviation in Contact Radius	Deviation in Center of Mass Height
3 $\mu L$	–6.8 %	34.2%
5 $\mu L$	–10.6 %	42.1%
7 $\mu L$	–11.1%	39.2%
10 $\mu L$	–12.3%	48.5%
12 $\mu L$	–13.8%	51.8%
15 $\mu L$	–22.0%	62.8%

in the spread state to be approximated without experimentally ejecting a droplet and measuring the dynamic geometry directly.

As in the adhesion model, the energy difference in the interfacial model can also be expressed per unit area with all terms scaled by the contact area of the maximally spread droplet ( $A_s$ ), where

$$A_s = \pi R^2 \sin^2 \theta_U. \quad (4.4)$$

Since  $R_{\text{sph}}$  can be expressed as a multiple of  $R$  where

$$R_{\text{sph}} = \left( \frac{2-3 \cos \theta_U + \cos^3 \theta_U}{4} \right)^{\frac{1}{3}} R, \quad (4.5)$$

all length terms in the change in total free interfacial energy drop out when scaled by  $A_s$  resulting in

$$\frac{\Delta E_{\text{int}}}{A_s} = \gamma_{\text{lg}} \frac{(4-6 \cos \theta + 2 \cos^3 \theta)^{\frac{2}{3}} - 2(1-\cos \theta_U) + \cos \theta_0 \sin^2 \theta_U}{\sin^2 \theta_U}. \quad (4.6)$$

Using the electrowetting equation (Eq. 4.3), each  $\theta_U$  can be expressed in terms of the known initial contact angle ( $\theta_0$ ) and  $EW$ . A detachment function can then be written as

$$f_{\text{int}}(EW) = \Delta E_{\text{int}}/A_s. \quad (4.7)$$

The critical electrowetting number predicted by the interfacial model ( $EW_{\text{cr,int}}$ ) occurs at the root of this function,  $f_{\text{int}}(EW_{\text{cr,int}}) = 0$ .

Critical electrowetting numbers predicted by the adhesion and interfacial models neglect changes in the gravitational potential energy of the droplet. When a droplet transitions from the maximally spread state to the detached state, its center of mass shifts upward (Fig. 4.1). This results in a change in gravitational potential energy ( $\Delta E_g$ ) that can be expressed as

$$\Delta E_g = \Delta \rho V g (R_{\text{sph}} - h_s), \quad (4.8)$$

where  $\Delta \rho$  is the droplet density relative to the surrounding medium,  $V$  is the droplet volume,  $g$  is the acceleration due to gravity, and  $h_s$  is the height of the center of mass of the droplet when maximally spread.

The center of mass height can be estimated by assuming the droplet maintains a spherical cap shape as it dynamically spreads ( $h_s \approx h_{\text{cap}}$ ). The center of mass height for a spherical cap relative to the surface ( $h_{\text{cap}}$ ) is computed as

$$h_{\text{cap}} = \frac{3(2R-H)^2}{4(3R-H)} - R + H, \quad (4.9)$$

where the total droplet height ( $H$ ) for a given droplet volume varies as

$$H = R(1 - \cos \theta_U). \quad (4.10)$$

However, this is known to overestimate  $h_s$  since droplets overshoot the steady-state position and do not maintain a spherical cap shape at all times. Experimental measurements from experiments performed later in this chapter show the steady-state center of mass is always higher than the maximally spread center of mass (Table 4.2).

Gravitational potential energy can be introduced to the adhesion (Eq. 4.1) and interfacial (Eq. 4.7) models to account for the change in center of mass height between the maximally spread and detached positions. The detachment function for the modified adhesion model becomes

$$f_{\text{adh+g}}(V, Ew) = f_{\text{adh}} + \Delta E_g/A_s. \quad (4.11)$$

Values for  $A_s$  and  $h_s$  at a given volume can be approximated in terms of  $Ew$  by again assuming the spread droplet takes its steady-state spherical cap shape. Thus  $f_{\text{adh+g}}$  is a function of volume and electrowetting number. The critical electrowetting number predicted by this new adhesion plus gravitational potential model ( $Ew_{\text{cr,adh+g}}(V)$ ) is then  $f_{\text{adh+g}}(V, Ew_{\text{cr,adh+g}}) = 0$ .

The interfacial model (Eq. 4.7) can similarly be modified to include changes in gravitational potential energy. The modified detachment function becomes

$$f_{\text{int+g}}(V, Ew) = f_{\text{int}} + \Delta E_g/A_s. \quad (4.12)$$

The critical electrowetting number predicted by this new interfacial plus gravitational potential model ( $Ew_{\text{cr,int+g}}(V)$ ) occurs when  $f_{\text{int+g}}(V, Ew_{\text{cr,int+g}}) = 0$ . This model is

expected to be the most accurate of the four presented, as it includes the fewest simplifying assumptions.

The impact of the change in gravitational potential energy during detachment can be examined by comparing the critical electrowetting numbers predicted by each model (Fig. 4.2). Predictions were calculated for an aqueous droplet in air at room temperature on a hydrophobic surface ( $\Delta\rho = 997 \text{ kg/m}^3$ ,  $\gamma_{lg} = 0.072 \text{ N/m}$ ,  $\theta_0 = 120.1^\circ$ ). Both the adhesion and interfacial models predict constant thresholds independent of volume. However, the interfacial prediction is approximately 8% higher. This is expected since the interfacial model considers energy changes along two additional interfaces.

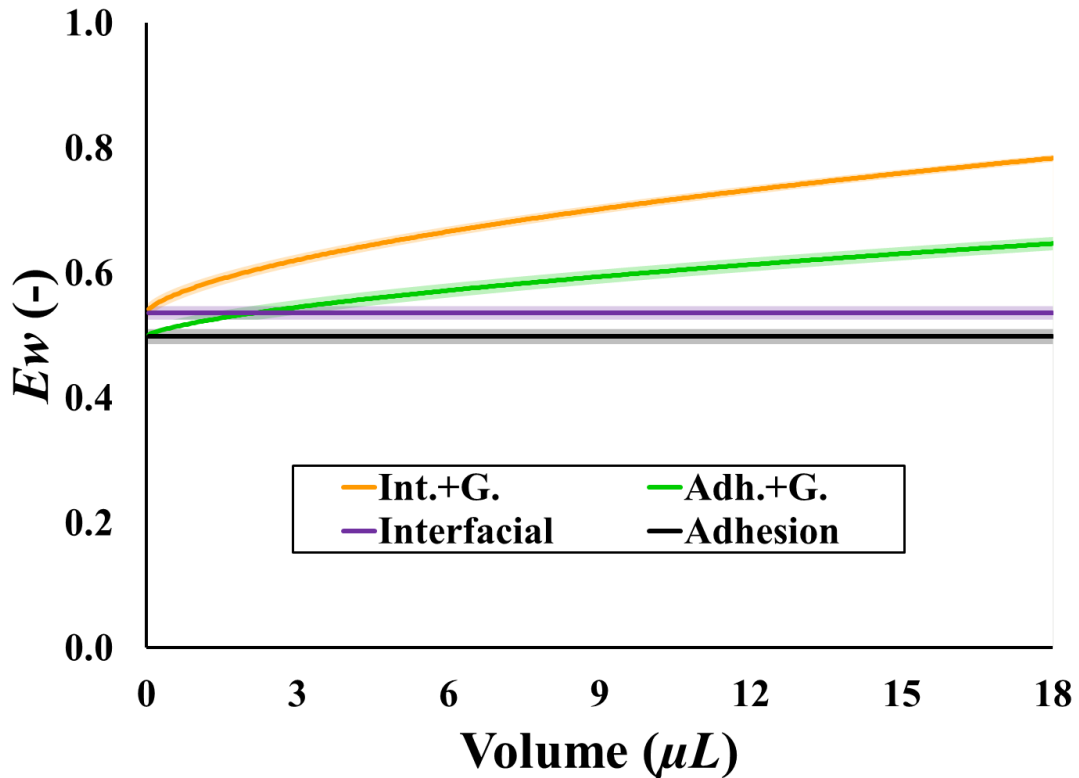


**Figure 4.2** Predicted  $E_w$  detachment thresholds for each model shown as solid lines. From top to bottom (based on  $18 \mu\text{L}$  volume): interfacial plus gravitational model (orange), adhesion plus gravitational model (green), interfacial model (purple), and adhesion model (black).<sup>35</sup>

The relative importance of gravitational potential energy appears to be significant as its inclusion causes a larger deviation from the adhesion model than the interfacial model for all volumes greater than  $2.5 \mu\text{L}$ . For the smallest droplets examined here ( $3 \mu\text{L}$ ), including gravitational potential in the adhesion and interfacial models results in predicted thresholds ( $Ew_{\text{cr}}$ ) that are 9% and 16% higher, respectively (Fig. 4.3). For  $15 \mu\text{L}$  droplets, inclusion of gravitational potential increases the predicted  $Ew_{\text{cr}}$  by 27% (adhesion) and 42% (interfacial). This suggests that gravitational effects may be significant, even for relatively small droplets.

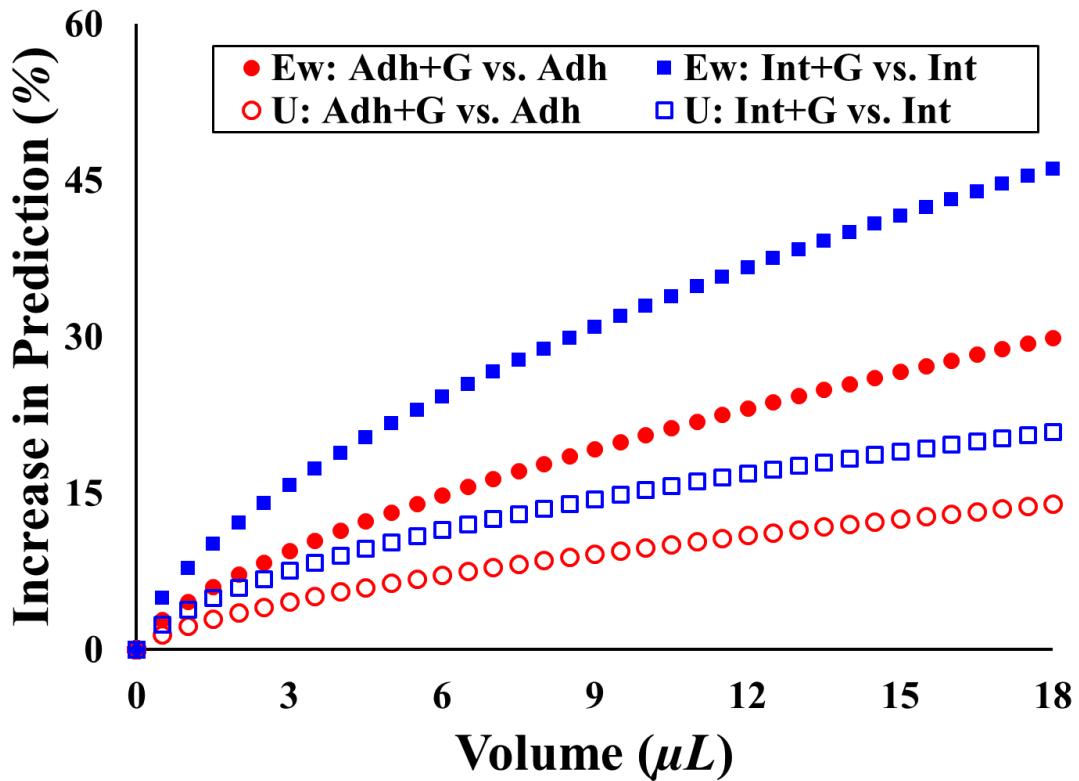


**Figure 4.3** Increase in predicted electrowetting number (solid) and corresponding voltage (empty) between the adhesion plus gravitational potential model (red circles) and the interfacial plus gravitational model (blue squares) as compared to the adhesion only and interfacial only models, respectively.<sup>35</sup>

## 4.2 Coplanar Ejection from Radially Symmetric Electrodes

The first objective of this investigation is to demonstrate electrowetting-induced droplet detachment from a coplanar electrode array. Figure 4.4 depicts typical actuation cycles of a  $5\ \mu\text{L}$  droplet that was (a) unsuccessfully and (b) successfully ejected from a coplanar device. The captured frame with the widest droplet contact diameter (i) is assumed to occur approximately when the actuation pulse is released and the droplet interface stores its maximum excess energy. The contact diameter then shrinks as the surface energy shifts the droplet upward (ii,iii). The bulk of the droplet then separates from the surface (iv) before falling back and reattaching (v,vi). Droplet detachment using coplanar electrodes was successfully recorded with volumes ranging from  $3\ \mu\text{L}$  to  $15\ \mu\text{L}$  (Table 4.3).

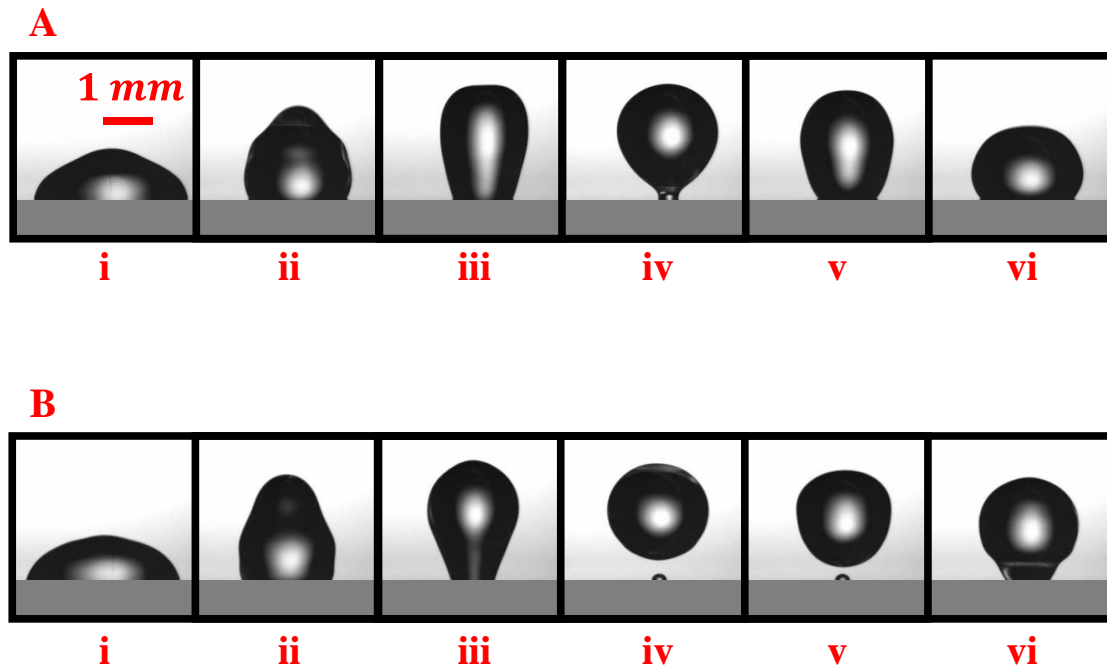


**Figure 4.4** Captured frames of a  $5\ \mu\text{L}$  droplet on a coplanar device (i) after a  $7\ \text{ms}$  pulse and then (ii-vi) every  $\sim 3.3\ \text{ms}$ . The droplet exhibits (a) incomplete detachment at  $250\ \text{V}$  and (b) detachment at  $260\ \text{V}$ .<sup>35</sup>

**Table 4.3** Observed droplet ejection thresholds<sup>35</sup>

Volume	Coplanar		Wired		Lee et al. <sup>56</sup> (Wired)
	Critical Voltage (V)	Critical $Ew$ (-)	Critical Voltage (V)	Critical $Ew$ (-)	Critical $Ew$ (-)
0.4 $\mu L$	-	-	-	-	0.67
1 $\mu L$	-	-	-	-	0.69
3 $\mu L$	249 $\pm$ 6	0.58 $\pm$ 0.03	124 $\pm$ 5	0.62 $\pm$ 0.05	0.62
5 $\mu L$	246 $\pm$ 9	0.57 $\pm$ 0.04	124 $\pm$ 5	0.62 $\pm$ 0.05	0.64
7 $\mu L$	257 $\pm$ 21	0.61 $\pm$ 0.10	131 $\pm$ 3	0.69 $\pm$ 0.03	-
10 $\mu L$	259 $\pm$ 6	0.63 $\pm$ 0.03	131 $\pm$ 6	0.69 $\pm$ 0.07	0.64
12 $\mu L$	276 $\pm$ 16	0.71 $\pm$ 0.08	135 $\pm$ 3	0.74 $\pm$ 0.03	-
15 $\mu L$	273 $\pm$ 9	0.70 $\pm$ 0.04	142 $\pm$ 7	0.81 $\pm$ 0.08	-

Previous coplanar detachment in air was only possible via a closely timed double pulse to perturb and then eject droplets.<sup>56</sup> The successful detachment from coplanar electrodes in this investigation can be attributed to electrode design. Unlike the IDEs used by Lee et al.,<sup>56</sup> the symmetry of the pattern used here allowed for more axisymmetric droplet spreading. This minimizes the amount of surface energy wasted on azimuthal oscillations as the droplet recedes. The four-part electrode array used here also significantly reduced the amount of dead space compared to the interdigitated electrodes.<sup>56</sup> The area fraction in the four-part coplanar design was  $\alpha_A \approx 0.495$  (less than 3% dead space) as compared to  $\alpha_A \approx 0.459$  on the interdigitated finger electrodes (~15% dead space). Lower area fractions limit the maximum achievable electrowetting number prior to the onset of contact angle saturation. Increasing voltage after saturation is not expected to induce detachment as the electrowetting response falls off dramatically.

While coplanar detachment was successful across the droplet volume range examined here, experimentally observed critical electrowetting numbers increased with droplet volume. The smallest droplets ( $3 \mu\text{L}$ ) ejected at an electrowetting number of  $0.58 \pm 0.03$ , while the largest droplets ( $15 \mu\text{L}$ ) ejected at  $0.70 \pm 0.04$ . This appears to contradict previous results on wired devices reported by Lee et al. that thresholds are independent of volume.<sup>56</sup> The discrepancy could be due to (i) the change to a coplanar electrode configuration or (ii) the higher range of droplet volumes examined here. The modified adhesion model supports the significance of the larger droplets examined. Predicted thresholds are up to 25% higher for an ejected  $15 \mu\text{L}$  when gravitational potential energy changes are considered.

### 4.3 Wired Ejection

To further examine the role of gravitational potential energy, experiments were repeated for all volumes in a wired configuration to observe the impact of droplet volume on critical electrowetting number. The wire used to ground droplets was less than 2% of the smallest droplet diameter and should have had a minimal influence on the system.<sup>40,56</sup>

Experimentally observed critical electrowetting numbers from both configurations in this investigation were compared to those from Lee et al.<sup>56</sup> Critical electrowetting numbers for both wired and coplanar configurations were consistent with previously reported data<sup>56</sup> for volumes between  $3 \mu\text{L}$  and  $10 \mu\text{L}$ . Previous work examining droplets at smaller volumes than those included here (including  $0.4 \mu\text{L}$  and  $1 \mu\text{L}$ ) observed an increase in critical electrowetting number in those cases.<sup>56</sup> This increase has been attributed to a change in spreading dynamics from underdamped to overdamped as droplets get smaller

( $R < \sim 1 \text{ mm}$ ) and increased domination of surface tension effects.<sup>71</sup> This limits the excess surface energy stored in the interface during dynamic spreading.

Like the coplanar data described above, an increase in critical electrowetting number was also apparent in the wired configuration over the larger range of volumes examined here. For the coplanar configuration, thresholds over the entire range increased with volume from  $0.62 \pm 0.05$  ( $3 \mu\text{L}$ ) to  $0.81 \pm 0.08$  ( $15 \mu\text{L}$ ). The wired configuration consistently had higher mean critical electrowetting numbers than the coplanar configuration, but thresholds between device types agreed for most volumes (two sample  $t$ -test,  $p > 0.01$ ). For the  $7 \mu\text{L}$  and  $15 \mu\text{L}$  trials, the wired configuration had statistically higher thresholds ( $p < 0.01$ ) than the coplanar configuration. This demonstrates that the increasing threshold-volume relationship is not unique to the coplanar configuration.

#### **4.4 Significance of Gravitational Potential Energy**

Experiments performed in this investigation suggest that gravitational potential significantly impacts droplet detachment. To test this hypothesis, experimental results were compared to predictions from analytical models with and without gravitational potential energy. Threshold conditions for detachment are consistently underpredicted when adhesion and interfacial models neglect changes in gravitational potential energy. Predictions from both models are improved in nearly all cases when changes in gravitational potential energy are considered.

Detachment of  $3 \mu\text{L}$  droplets in wired and coplanar configurations ( $n = 8$ ) was observed at  $E_w = 0.62$  ( $s = 0.05$ ) and  $E_w = 0.58$  ( $s = 0.03$ ), respectively. When changes in gravitational potential energy were neglected, the adhesion model predicted

droplet detachment at  $E_{w,cr,adh} = 0.50 \pm 0.01$  for all volumes. The difference between the predicted and experimentally observed threshold was statistically significant in this case (two sample  $t$ -test,  $p < 0.01$ ). This demonstrates that the adhesion model underpredicts the detachment threshold, suggesting that additional energies may play a significant role in detachment.

When gravitational potential energy is neglected, accuracy of predictions made with the adhesion model decreases with increasing droplet volume (Fig. 4.5). At  $3 \mu L$  the adhesion model deviated by 19% and 14% on wired and coplanar devices, respectively

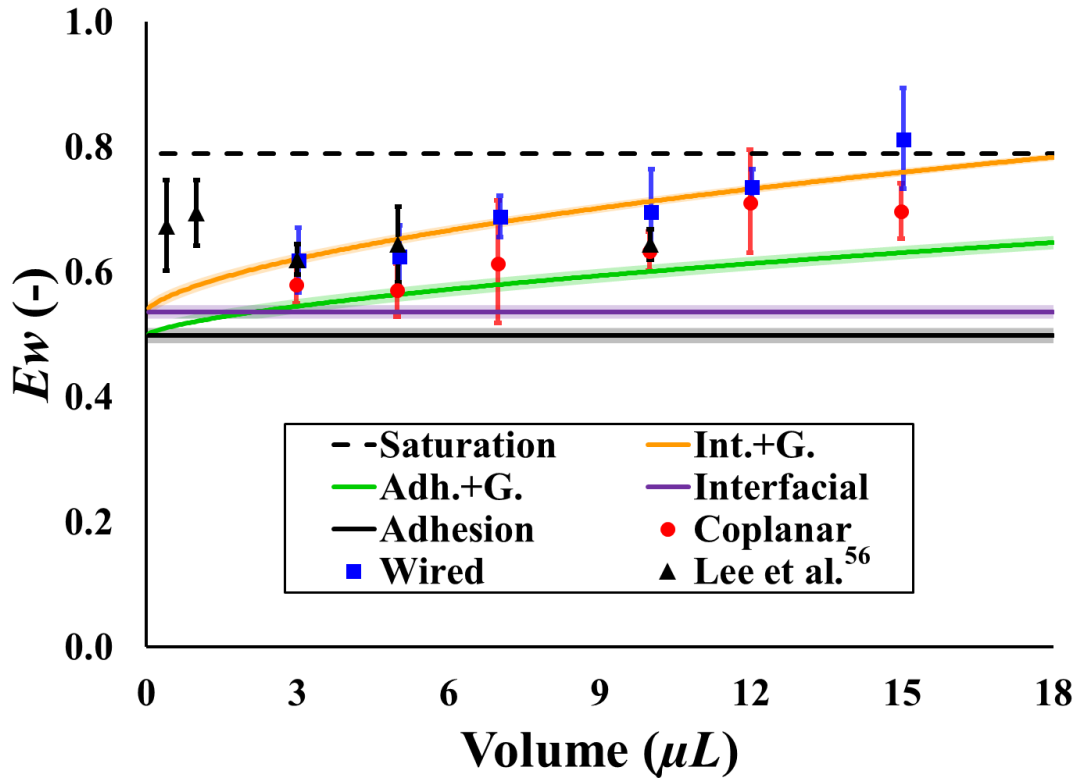


**Figure 4.5** Coplanar detachment threshold results (red circles), wired results (blue squares), Lee et al.'s wired results<sup>56</sup> (black triangles), saturation limit (dashed black), and detachment threshold predictions from top to bottom (based on an  $18 \mu L$  volume): interfacial plus gravitational model (solid orange), adhesion plus gravitational model (solid green), interfacial model (solid purple), and adhesion model (solid black).<sup>35</sup>

**Table 4.4** Deviations from predicted thresholds<sup>35</sup>

	Volume	Adhesion Model	Interfacial Model	Adh. + G. Model	Int. + G. Model
Coplanar	3 $\mu L$	14.0%	7.5%	5.9%	-7.2%
	5 $\mu L$	12.7%	6.0%	1.2%	-14.4%
	7 $\mu L$	18.7%	12.5%	5.4%	-10.8%
	10 $\mu L$	21.3%	15.3%	5.1%	-12.6%
	12 $\mu L$	30.0%	24.6%	13.8%	-3.0%
	15 $\mu L$	28.6%	23.1%	9.5%	-8.9%
Wired	3 $\mu L$	19.4%	13.2%	11.8%	-0.5%
	5 $\mu L$	20.2%	14.1%	9.7%	-4.5%
	7 $\mu L$	27.6%	22.1%	15.8%	1.4%
	10 $\mu L$	28.3%	22.9%	13.6%	-2.6%
	12 $\mu L$	32.3%	27.1%	16.6%	0.4%
	15 $\mu L$	38.7%	34.0%	22.3%	6.5%
Lee et al. <sup>56</sup> (Wired)	0.4 $\mu L$	16.6%	12.5%	14.9%	9.4%
	1 $\mu L$	19.2%	15.2%	16.1%	9.8%
	3 $\mu L$	9.3%	4.8%	2.1%	-7.4%
	5 $\mu L$	12.8%	8.4%	3.1%	-7.7%
	10 $\mu L$	12.8%	8.4%	-2.3%	-16.1%

(Table 4.4). The discrepancy roughly doubles for 15  $\mu L$  droplets to 39% and 29%, respectively. The increasing error suggests that the adhesion model oversimplifies the droplet system. Experimental detachment thresholds in both configurations increased with volume. A model neglecting gravitational potential energy does not capture this effect. Effectively, such a model predicts the minimum limit for a massless droplet.

Inclusion of gravitational potential energy improves critical electrowetting number predictions and captures the increasing threshold-volume relationship. The roots of the adhesion plus gravitational potential model detachment function (Eq. 4.11) were calculated to predict critical electrowetting numbers for the range of volumes tested here (Fig. 4.5).

Including changes in gravitational potential improved prediction accuracy from 14.0% (without) to 5.9% (with) for 3  $\mu\text{L}$  droplets on coplanar devices. The improvement increased with droplet volume with deviations going from 28.6% (without) to 9.5% (with) for 15  $\mu\text{L}$  droplet. On wired devices, inclusion of gravitational potential improved the accuracy of the adhesion model from 19.4% (without) to 11.8% (with) for 3  $\mu\text{L}$  droplets and 38.7% (without) to 22.3% (with) for 15  $\mu\text{L}$  droplets.

Experimental thresholds were also found to be underestimated by the interfacial model when changes in gravitational potential energy were neglected. The interfacial model predicted a higher threshold of  $Ew_{\text{cr,adh}} = 0.54 \pm 0.01$  for all volumes. It was expected that this prediction would be higher than the adhesion prediction as it accounts for additional interfacial energy changes in the system. However, it still fell below the mean experimental threshold at all volumes with the magnitude of underprediction generally increasing with volume. This suggests interfacial energy alone may not provide a sufficiently accurate prediction of critical electrowetting number.

The accuracy of the interfacial model was also improved by the inclusion of gravitational potential energy (Fig. 4.5). Deviations on coplanar devices improved from 7.5% (without) to  $-7.2\%$  (with) for 3  $\mu\text{L}$  droplets and from 23.1% (without) to  $-8.9\%$  (with) for 15  $\mu\text{L}$  droplets. On wired devices, the accuracy improved from 13.2% (without) to  $-0.5\%$  (with) for 3  $\mu\text{L}$  droplets and 34.0% (without) to 6.5% (with) for 15  $\mu\text{L}$  droplets.

Of the four models examined, the interfacial plus gravitational potential model generally provides the most accurate prediction of experimentally observed critical electrowetting numbers. This was expected as this model accounts for the most energies influencing the droplet's behavior out of the different models examined. In the wired

configuration, this model predicts a threshold within approximately 6% of what was experimentally observed. In the coplanar configuration, the interfacial plus gravitational model deviates least for the two largest volumes. The adhesion plus gravitational model predicts the detachment threshold most accurately for the remaining smaller droplet volumes.

Based upon the collected results and despite previous findings to the contrary,<sup>56</sup> gravitational potential energy appears to have a significant impact on the critical electrowetting number required for droplet detachment. While the low Bond numbers for the droplets examined here indicate that droplet mass did not significantly affect droplet shape in any case, droplet mass still affects the magnitude of gravitational potential energy changes as droplets are lifted through the air. Analytical and experimental results in this investigation demonstrate that this change in gravitational potential energy is a significant contribution to the energy difference between the ejected and spread states and should be considered when performing electrowetting-induced droplet ejection.

## **4.5 Summary**

This investigation demonstrates the first coplanar droplet detachment in air using single pulses. Additionally, it presents two new models for electrowetting-induced droplet detachment that account for the gravitational potential energy of the droplet. An improved understanding of the detachment threshold is critical for development of 3D digital microfluidic (DMF) devices. While the threshold has previously been estimated using either the work of adhesion or total free interfacial energy changes, in the experiments performed here it was observed that these estimates fell increasingly below what was

observed. The proposed models incorporate the increase in gravitational potential energy of a detaching droplet into these previous models. By approximating the droplet's spreading profile with its steady state electrowetting profile, the new models can be used to predict the electrowetting number required for detachment prior to any experimentation. Threshold predictions using these models agreed more closely with the observed thresholds, roughly halving the deviation from the adhesion model.

It should be noted that a droplet in a 3D DMF device has the potential to be manipulated when resting on the bottom plate of the device or when hanging from the top plate. The results here suggest that the voltage threshold to detach a droplet would change whether ejecting a droplet upward or downward. Future investigations into the voltage threshold for inverted ejection will prove beneficial for the advancement of 3D DMF devices.

## 5.0 Impact of Electrode Geometry on Ejection

The investigation in this chapter extends the coplanar electrowetting-induced ejection experiments in air described in Chapter 4.<sup>35</sup> In those experiments droplets were successfully ejected from a coplanar electrowetting device featuring a radially symmetric electrode design. The electrode pad beneath the droplet was divided into four segments with  $20\ \mu\text{m}$  gaps separating them. Successful ejection was attributed to the greatly reduced the gap space beneath an actuated droplet as compared to previous coplanar ejection performed using interdigitated finger electrode,<sup>56</sup> but the role of the design was not thoroughly examined. The design used also incorporates small features not compatible with current low-cost electrode fabrication techniques.<sup>18,37,50</sup>

In this investigation, the electrowetting and ejection performance of multiple variations of the coplanar design used in Chapter 4 are characterized. Detachment pads are segmented into four, six, or eight electrodes parts. Spacing between individual electrodes varies from  $20\ \mu\text{m}$  to  $200\ \mu\text{m}$ . Predicted performance for a  $5\ \mu\text{L}$  droplet on each design is first determined numerically. Designs are then tested experimentally on physical devices. All devices are fabricated using the same cleanroom processes to isolate the effects of number of electrode segments and electrode spacing. Increasing voltage is applied until electrowetting-induced droplet ejection is observed. Observed droplet ejection thresholds for each design are presented with the thresholds predicted using the ejection model developed in Chapter 4. A minimum of four trials are performed for each case. All measurement errors are reported as one standard deviation from the mean unless otherwise specified.

The material presented in this chapter has been submitted for publication in *Sensors and Actuators A: Physical*.<sup>36</sup>

## 5.1 Electrode Design Variations

Five different cleanroom-fabricated (CRF) electrode patterns were tested here. Electrodes in the benchmark pattern (Fig. 5.1a) consisted of a 6 mm diameter circular region divided into four quarter-circle segments. Alternating segments were connected at either the center of the circular region or by an outer ring. The minimum spacing between electrodes was 20  $\mu\text{m}$ . The benchmark design is referred to here as “CRF4-20” which

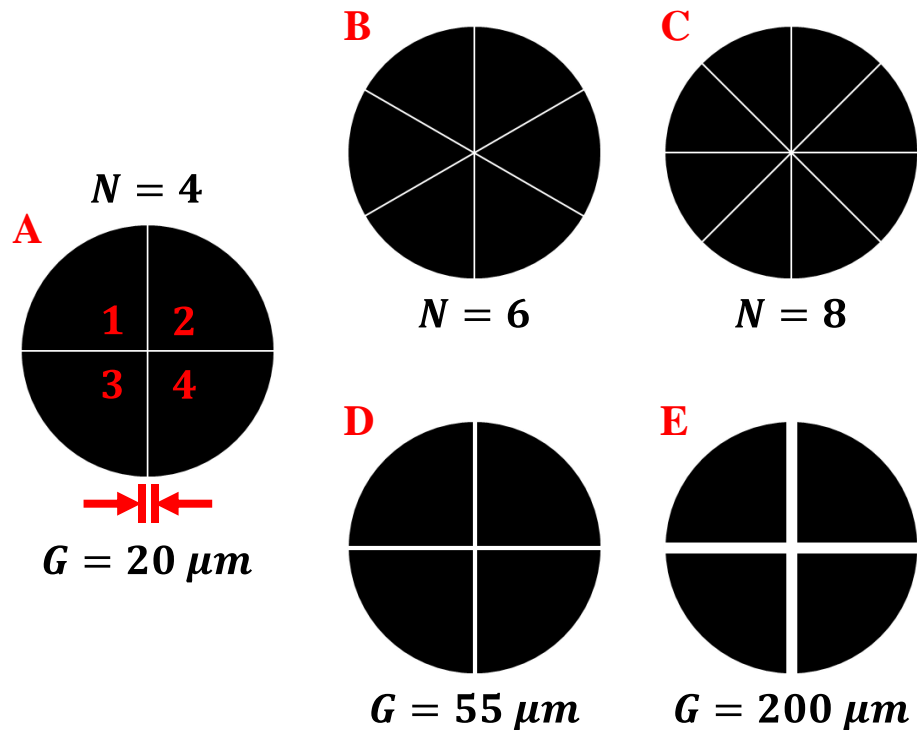


**Figure 5.1** Simplified top-view of the detachment pad designs used with varying numbers of segments ( $N$ ) and minimum gap spacings ( $G$ ). Gaps are not to scale. Wiring of alternating segments is not shown.<sup>36</sup>

references the fabrication process (CRF), number of segments (4), and electrode spacing ( $20\ \mu\text{m}$ ) to identify the design and distinguish it from the other four.

The effect of the number of segments in the coplanar electrode array was tested using two additional designs with  $20\ \mu\text{m}$  spacing. These designs have the same circular electrode region divided into either six (“CRF6-20”) (Fig. 5.1b) or eight (“CRF8-20”) (Fig. 5.1c) segments.

The effect of electrode spacing was tested using two additional designs with four segments in the coplanar electrode array. These designs have the same overall footprint but with minimum spacings of  $55\ \mu\text{m}$  (“CRF4-55”) (Fig. 5.1d) and  $200\ \mu\text{m}$  (“CRF4-200”) (Fig. 5.1e) between features. These spacings were chosen to mimic reported resolutions of low-cost inkjet-printing fabrication methods.<sup>18,37,50</sup>

## 5.2 Design Analysis

Predicted electrowetting performance of each design was first compared using numerically measured area factors ( $\alpha_A$ ) for an initially unactuated  $5\ \mu\text{L}$  droplet centered on each design (Table 5.1). These were computed as

$$\alpha_A = \sqrt{\frac{A_a}{A_t} \left( \frac{A_r}{A_a + A_r} \right)^2 + \frac{A_r}{A_t} \left( \frac{A_a}{A_a + A_r} \right)^2}, \quad (5.1)$$

where  $A_a$  is the measured active electrode area beneath the droplet,  $A_r$  is the measured reference electrode area beneath the droplet, and  $A_t$  is the total contact area of the droplet. Droplets were assumed to have an initial contact angle ( $\theta_0$ ) of  $\theta_0 = 120^\circ$ .

An area efficiency ( $\eta_A$ ) was computed for each design by normalizing all area factors by the theoretical maximum area factor ( $\eta_A = \alpha_A/0.5$ ). The four-part design with

**Table 5.1** Predicted electrowetting performance over the contact area of a centered 5  $\mu\text{L}$  droplet ( $\theta_0 = 120^\circ$ )<sup>36</sup>

Device Type	Area Factor ( $\alpha_A$ )	Area Efficiency ( $\eta_A$ )	Voltage Increase ( $0.5/\alpha_A - 1$ )
CRF4-20	0.493	98.6%	1.4%
CRF6-20	0.490	98.0%	2.1%
CRF8-20	0.486	97.3%	2.8%
CRF4-55	0.482	96.4%	3.7%
CRF4-200	0.433	86.6%	15.4%

20  $\mu\text{m}$  spacing (CRF4-20) served as the benchmark for comparison as it had previously been used to study droplet ejection.<sup>35</sup> The benchmark CRF4-20 design was found to have the highest area efficiency ( $\eta_A = 0.986$ ).

Area efficiency decreased as detachment electrodes were further segmented and additional gap lines were required. The CRF8-20 had an area efficiency of  $\eta_A = 0.973$  which would only increase voltage requirements by 1.4% as compared to an ideal design with  $\eta_A = 1$ . As all gaps were relatively narrow ( $\sim 20 \mu\text{m}$ ), total dead space with eight segments is a small fraction of the overall droplet area ( $\sim 5.3\%$ ).

Area efficiency also fell as gap space widened. The CRF4-55 was moderately less efficient at  $\eta_A = 0.964$ , but efficiency fell significantly on CRF4-200 down to  $\eta_A = 0.866$ . Nearly one quarter of the CRF4-200 design is gap space which results in a 15.4% increase in voltage requirements versus an ideal design. This suggests that droplet ejection from a CRF4-200 device would require a significantly higher voltage than a device of any of the other four designs.

Predicted sensitivity to droplet position on each device type was then examined by computing  $\eta_A$  for droplets positioned offset toward one electrode (Fig. 5.2). An increased

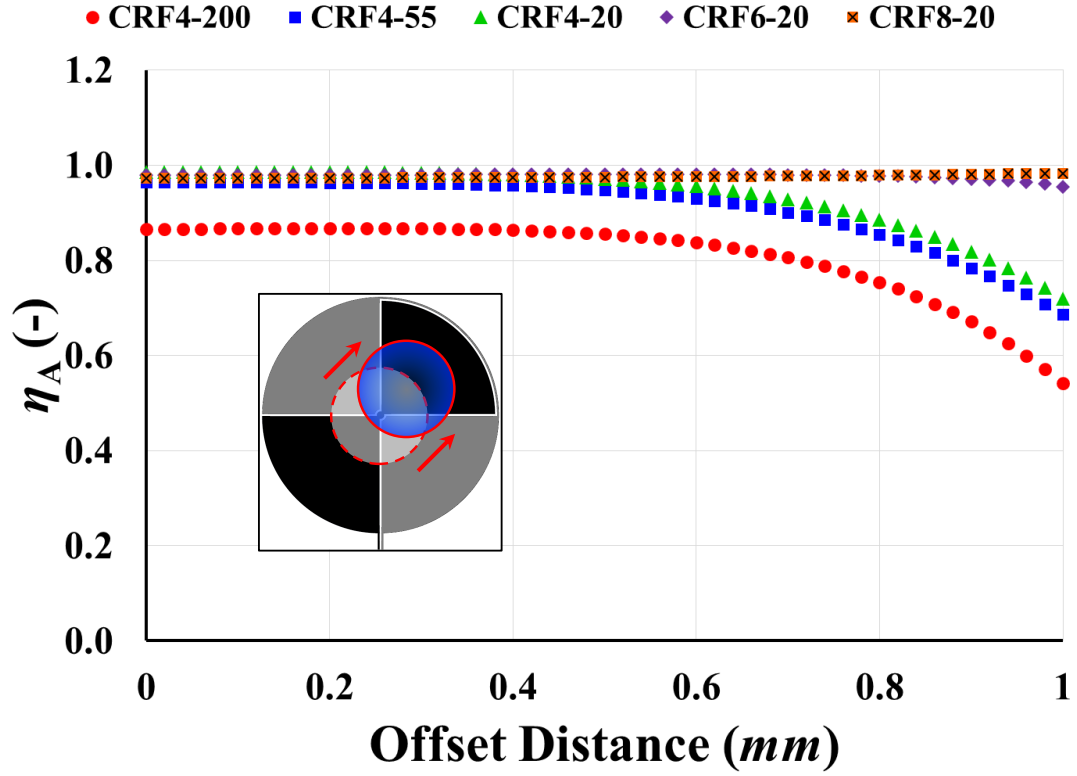


**Figure 5.2** Expected area factor efficiency of a  $5 \mu L$  droplet offset along the midline of an electrode segment (inset).<sup>36</sup>

number of segments in the electrode array delays the decline in predicted performance at higher offsets. The benchmark CRF4-20 design remains the most efficient ( $\eta_A \approx 98\%$ ) for offsets up to  $0.4 \text{ mm}$  and remains relatively constant (within 2%) until an offset of  $0.52 \text{ mm}$ . At larger offsets, the area efficiency on CRF4-20 begins to drop off. A substantially offset droplet on the CRF4-20 design rests primarily over a single electrode segment. This creates an imbalance in the active versus reference areas covered. The voltage in each region is inversely related to the size of its areas and can be computed as

$$U_a = \frac{A_r}{A_a + A_r} U, U_r = \frac{A_a}{A_a + A_r} U, \quad (5.2)$$

where  $U$  is the input voltage,  $U_a$  is the voltage across the dielectric layer in the active electrode region, and  $U_r$  is the voltage across the dielectric layer in the reference electrode region. At an offset position, the resulting imbalance in covered electrode areas reduces the voltage applied to most of the droplet.

Predicted performance on the CRF6-20 and CRF8-20 designs for small offsets ( $< \sim 0.54 \text{ mm}$ ) is similar to the benchmark case despite the additional gap lines required. At larger offsets CRF6-20 and CRF8-20 become more efficient than CRF4-20 despite their increased gap space. Performance on CRF6-20 does not appreciably decay ( $> 2\%$ ) until an offset of  $1 \text{ mm}$ , and performance on CRF8-20 never appreciably decays in the offset range examined. The additional electrode segments in the CRF6-20 and CRF8-20 designs allow for a more equal ratio of active and reference electrode areas to be covered at an offset position. It is expected that at even larger offsets the CRF8-20 design will also drop off as the droplet begins to cover predominantly a single electrode segment. These results suggests reductions in performance due to an offset can be mitigated by further subdividing the electrode pad as is also done with thin-film transistor arrays.<sup>76</sup>

The gap distance between electrodes results in a more rapid decline of predicted performance at increasing offsets. Performances on the CRF4-20, CRF4-55, and CRF4-200 designs all begin to drop off appreciably beyond offsets of approximately  $0.52 \text{ mm}$ . However, the overall drop in performance due to a  $1 \text{ mm}$  offset ( $\eta_A(1 \text{ mm})/\eta_A(0)$ ) increases with increasing gap size. Performance on the CRF4-20, CRF4-55, and CRF4-200 designs drops by 27%, 29%, and 38%, respectively. By minimizing the spacing between electrodes the impact of a sizeable offset can be reduced.

Area efficiency on all five designs is minimally impacted by small offsets and drops less than 2% for offsets up to 0.52 mm. In this range, a design with the fewest segments is preferable since it will have the highest efficiency. If higher offsets are expected, then additional segments can be included to reduce the sensitivity of efficiency to droplet offset. This comes at the cost of additional gap lines, but overall gap space can remain low if gap widths are small.

### 5.3 Droplet Ejection Results

Electrowetting-induced droplet detachment experiments were successfully performed on all five electrode designs. Droplets were actuated at increasing voltages until detachment was observed. Figure 5.3 shows a typical detachment process captured on a CRF4-200 device. Actuation causes the droplet bulk to shift from its initial position (Fig. 5.3a) downward toward the substrate to a deformed position (Fig. 5.3b). As the signal is released, the droplet returns towards its initial position (Fig. 5.3c). With sufficient stored energy, the droplet can overshoot the initial position (Fig. 5.3d) and eject from the surface (Fig. 5.3e). The success on the CRF4-200 design is promising for future inkjet-printed 3D digital microfluidic (DMF) device testing, as current low-cost printing techniques are capable of producing electrodes with similar feature resolution.<sup>18,37,50</sup>

Threshold voltages for detachment were then compared to predicted performance. Predicted critical electrowetting numbers for droplet ejection ( $EW_{CR}$ ) were computed using the interfacial plus gravitational potential energies model developed in Chapter 4 and used to determine critical voltage thresholds ( $U_{CR}$ ). In a coplanar device, voltage is related to the effective electrowetting number over the droplet contact area ( $EW_A$ ) as

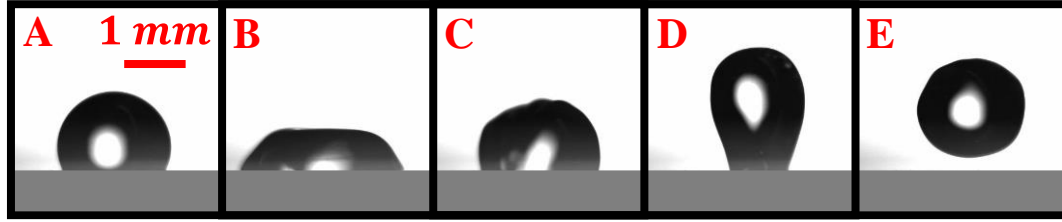


**Figure 5.3** A  $5 \mu\text{L}$  droplet ejected from a CRF4-200 electrowetting device. Approximately  $5 \text{ ms}$  elapse between consecutive frames.<sup>36</sup>

$$U = \sqrt{\frac{2d\gamma_{\text{lg}}Ew_A}{\epsilon_0\epsilon_d\alpha_A^2}}, \quad (5.3)$$

where  $U$  is the applied voltage,  $d$  is the thickness of the dielectric layer,  $\gamma_{\text{lg}}$  is the surface tension along the liquid-gas interface,  $\epsilon_0$  is the permittivity of free space, and  $\epsilon_d$  is the dielectric constant.

Experimental thresholds on CRF4-200, CRF4-55, CRF6-20, and CRF8-20 devices were all significantly higher than previously observed on the benchmark CRF4-20 (two sample  $t$ -tests,  $p < 0.01$ ) and occurred beyond the estimated onset of saturation (Fig. 5.4). This is attributable in part to differences in dielectric thickness. The previously fabricated CRF4-20 devices had a coating thickness of  $4.8 \pm 0.4 \mu\text{m}$ . The CRF4-200, CRF4-55, CRF6-20, and CRF8-20 devices were fabricated separately and had a measured dielectric thickness of  $5.4 \pm 0.6 \mu\text{m}$ . Predictions shown in Figure 5.4 reflect the measured dielectric thickness specific to each design type. An increase in dielectric thickness reduces the effective electrowetting number. This increases the voltage necessary to achieve the critical electrowetting number for detachment.

Observed voltage thresholds on the CRF4-200, CRF4-55, CRF6-20, and CRF8-20 devices were not statistically significantly different from each other (single-factor

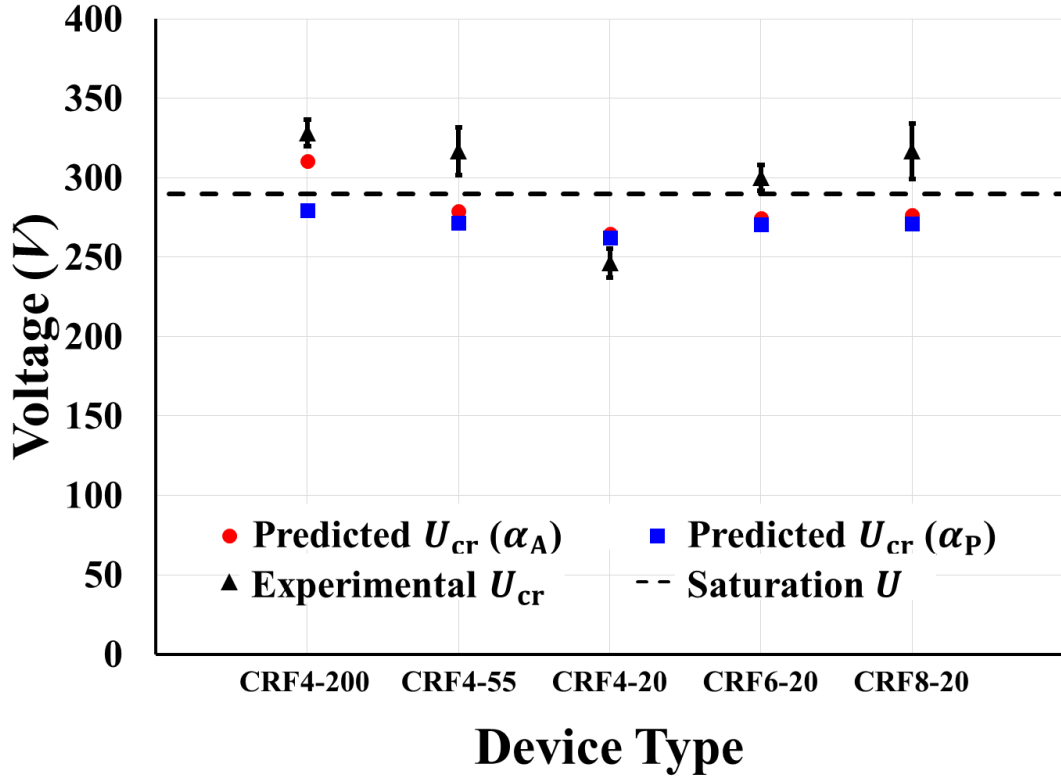


**Figure 5.4** Experimentally observed threshold voltage and critical electrowetting number for droplet ejection from each device type.<sup>36</sup>

ANOVA,  $p > 0.05$ ). It was expected that the CRF4-55, CRF6-20, and CRF8-20 devices would have similar voltage thresholds since they have similar area efficiencies (within  $\sim 2\%$ ). The same parameter suggested detachment on the CRF4-200 design would be less likely since its area efficiency was lower ( $\eta_A = 86.6\%$ ). The predicted detachment voltage on CRF4-200 devices (310 V) was  $\sim 13\%$  higher than on all other designs.

## 5.4 Contact Line Electrowetting Model

Successful detachment from the CRF4-200 design despite its poor efficiency suggests that the geometry coefficient  $\alpha_A$  may underpredict the effectiveness of an

electrode design in some cases. In practice, the electrowetting response and subsequent spreading of a droplet are driven by changes at the contact line.<sup>59</sup> As such, dead space at the center of the droplet area may not have an impact on spreading.

The effective electrowetting number over the entire droplet contact area has previously been computed as

$$EW_A = \frac{\epsilon_0 \epsilon_d}{2d\gamma_{lg}} \left( \frac{A_a}{A_t} U_a^2 + \frac{A_r}{A_t} U_r^2 + \frac{A_g}{A_t} U_g^2 \right), \quad (5.4)$$

where  $A_g$  is the gap area beneath the droplet, and  $U_g$  is the voltage across the dielectric layer in the gap region.<sup>29,35</sup> This can be reformulated to compute the effective electrowetting number only at the contact line of the droplet ( $EW_P$ ). This is expressed as

$$EW_P = \frac{\epsilon_0 \epsilon_d}{2d\gamma_{lg}} \left( \frac{s_a}{s_t} U_a^2 + \frac{s_r}{s_t} U_r^2 + \frac{s_g}{s_t} U_g^2 \right), \quad (5.5)$$

where  $s_a$ ,  $s_r$ , and  $s_g$  are the total lengths of the droplet contact line over active electrodes, reference electrodes, and gaps, respectively. The total length of the contact line ( $s_t$ ) is equivalent to the perimeter of the circular interface where the droplet contacts the substrate.

Since  $U_g = 0$ , this reduces to

$$EW_P = \frac{\epsilon_0 \epsilon_d}{2d\gamma_{lg}} \alpha_P^2 U^2, \quad (5.6)$$

where a new “perimeter factor” ( $\alpha_P$ ) can be defined as

$$\alpha_P = \sqrt{\frac{s_a}{s_t} \left( \frac{A_r}{A_a + A_r} \right)^2 + \frac{s_r}{s_t} \left( \frac{A_a}{A_a + A_r} \right)^2}. \quad (5.7)$$

This new factor characterizes how effectively the input voltage is distributed to the contact line. All geometric quantities used to determine the perimeter factor are also computed at a maximally spread droplet position to better reflect the physical spreading behavior rather than an initially unactuated shape as previously done using an area factor analysis.<sup>35</sup> These

**Table 5.2** Predicted electrowetting performance along the contact line of a centered 5  $\mu\text{L}$  droplet ( $\theta = 75^\circ$ )<sup>36</sup>

Device Type	Perimeter Factor ( $\alpha_P$ )	Perimeter Efficiency ( $\eta_P$ )	Voltage Increase ( $0.5/\alpha_P - 1$ )
CRF4-20	0.498	99.6%	0.4%
CRF6-20	0.497	99.3%	0.7%
CRF8-20	0.496	99.2%	0.8%
CRF4-55	0.495	99.0%	1.1%
CRF4-200	0.481	96.1%	4.0%

are approximated using the steady-state spherical cap shape predicted by the general electrowetting equation at saturation. The model used to predict detachment similarly approximates the spread geometry using the steady-state geometry.

The perimeter factor was computed for a centered droplet on all designs (Table 5.2). A fixed contact angle ( $\theta$ ) of  $\theta = 75^\circ$  was used for all cases here, as this is the approximate saturation angle on the CRF4-20 device. A droplet centered on an idealized version of the designs used here where no gaps were present and the active electrode area, reference electrode area, active electrode perimeter, and reference electrode perimeter were equal ( $\frac{A_a}{A_t} = \frac{A_r}{A_t} = \frac{s_a}{s_t} = \frac{s_r}{s_t} = 0.5$ ) would have a perimeter factor of  $\alpha_P = 0.5$ . Results were scaled by this value to compute a perimeter efficiency ( $\eta_P = \alpha_P/0.5$ ). Perimeter efficiency was slightly higher ( $\sim 2\%$ ) for most designs as compared to their area efficiency. In the case of the CRF4-200 design,  $\eta_P$  was more than 10% higher than  $\eta_A$ . As a result, perimeter efficiencies for all designs agreed within 4%, whereas previously the area efficiency of CRF4-200 was  $\sim 11\%$  lower than all other designs. This agreement in predicted

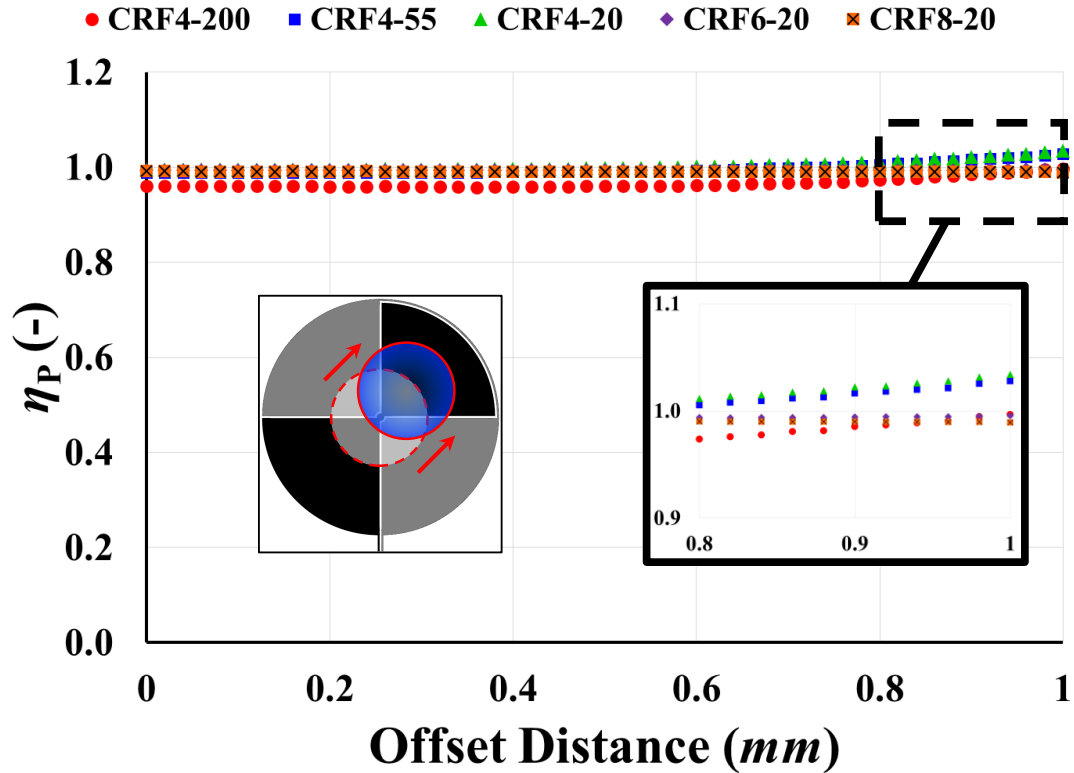


**Figure 5.5** Expected perimeter factor efficiency of a  $5 \mu\text{L}$  droplet offset along the midline of an electrode segment.<sup>36</sup>

performance matches the trend in the experimental results where droplets on the CRF6-20, CRF8-20, CRF4-55, and CRF4-200 designs all ejected at similar voltages (Fig. 5.4).

Predicted sensitivity to droplet position was then reexamined by computing  $\eta_P$  at different offsets along the midline of one electrode (Fig. 5.5). As with  $\eta_A$ , the efficiency on all designs is initially steady. Performance decreases less than 2% for offsets up to 0.84 mm. At higher offsets performance continues to hold steady or improves. On the CRF4-20 and CRF4-55 designs,  $\eta_P$  exceeds 1 at an offset of 1 mm. This indicates that in these positions the effective voltage along the contact line ( $\tilde{U}_P$ ) is more than half of the input voltage.

The effective voltage over the entire droplet area ( $\tilde{U}_A$ ) is limited to 50% of the input voltage. The effective area voltage increases as the square of the voltage on the active and reference electrodes increases, where

$$\tilde{U}_A^2 = \frac{2d\gamma_{lg}}{\epsilon_0\epsilon_d} EW_A = \frac{A_a}{A_t} U_a^2 + \frac{A_r}{A_t} U_r^2. \quad (5.8)$$

Because the voltage on each electrode is inversely related to its area (Eq. 5.2),  $\tilde{U}_A$  is maximized when the areas are equal. An imbalance in the ratio of active to reference electrode area can result in a higher local voltage on one of the two electrodes, but will still reduce the effective voltage applied to the entire area.

## 5.5 Designing for Localized Electrowetting

The perimeter factor model suggests that dissimilarly sized electrodes can be beneficial when interested only in increasing the voltage applied at the contact line. The effective contact line voltage ( $\tilde{U}_P$ ) can be represented as

$$\tilde{U}_P^2 = \frac{2d\gamma_{lg}}{\epsilon_0\epsilon_d} EW_P = \frac{s_a}{s_t} U_a^2 + \frac{s_r}{s_t} U_r^2. \quad (5.9)$$

Voltages at positions elsewhere in the droplet area do not contribute to  $\tilde{U}_P$ . However, the ratio of active to reference electrode areas still dictates  $U_a$  and  $U_r$ . Having two dissimilarly sized electrodes will result in voltage being preferentially distributed toward the smaller electrode. If the contact line primarily covers the smaller electrode, then it will receive most of the input voltage. The larger electrode can be safely positioned toward the center of the droplet where voltage can be sacrificed. This imbalance in the ratio of active to reference electrode areas still results in a lower  $\tilde{U}_A$ , but the careful positioning can also result in  $\tilde{U}_P$  exceeding half of the input voltage.

In an extreme case,  $\alpha_p$  has a maximum value of 1 when the contact line covers an infinitely thin ring-shaped active electrode and the droplet contact area covers a circular reference electrode (Fig. 5.6). However, such a case is unrealistic since a droplet spreads as it is actuated and must cover both active and reference electrodes at all times to do so. The contact radius of the initial unactuated droplet limits the maximum size of the circular electrode ( $r_{\text{inner}}$ ). The minimum outer radius of the ring electrode ( $r_{\text{outer}}$ ) is limited by the contact radius of a maximally spread droplet, since a ring electrode any smaller would limit spreading. For the  $5 \mu\text{L}$  droplets on the hydrophobic surface used here ( $\theta_0 \approx 120^\circ$ ), the limits of these radii are  $0.97 \text{ mm}$  and  $1.51 \text{ mm}$ , respectively. In practice, constructing such a design (Fig. 5.6), where any wiring or gaps are neglected ( $s_a = 0$ ,  $s_r/s_t = 1$ ) results in a perimeter factor of only  $\alpha_p = 0.41$ . This is less efficient than a droplet on any of the physical designs tested here. While there may be a more efficient electrode geometry

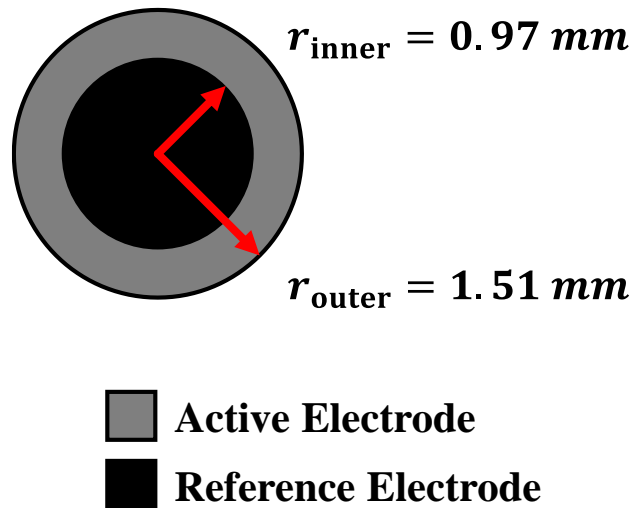


**Figure 5.6** Top-view schematic of a theoretical two-part electrode design sized for a  $5 \mu\text{L}$  droplet ( $\theta_0 \approx 120^\circ$ ).<sup>36</sup>

suitable for physical applications, this suggests the optimal design is not obvious and merits further investigation.

## 5.6 Summary

The electrode geometry is an important design consideration in coplanar electrowetting applications. An efficient design maximizes the electrowetting number achieved at a given input voltage by minimizing dead space and allowing a droplet to cover as equal a ratio of active to reference electrode areas as possible. Efficiency also translates to reaching a target electrowetting number at a reduced voltage as is critical in a droplet ejection application. Radially symmetric electrode designs can be highly efficient provided droplet are not significantly offset. Such designs can contain fewer parts than an interdigitated finger design and as a result require less gap space. The more uniform radial spreading is also beneficial for droplet ejection.

Droplets here were successfully detached from all examined electrode designs. This includes a four-part electrode design with  $200\ \mu\text{m}$  gaps between the electrode segments (CRF4-200). The successful detachment despite the significant dead space beneath the initial droplet ( $\sim 25\%$ ) suggests that a sufficient electrowetting number at the contact line is critical for detachment rather than a sufficient mean electrowetting number across the entire droplet area. The proposed perimeter factor ( $\alpha_P$ ) characterizes how effectively input voltage is divided through the electrode array at the contact line. Successful ejection on the CRF4-200 design is also promising for the design of future 3D inkjet-printed DMF devices as current low-cost printing techniques can already achieve spacings of this size and smaller.

## 6.0 Ejection from Inkjet-Printed Devices

The investigation in this chapter examines electrowetting-induced droplet ejection on digital microfluidic (DMF) devices fabricated using the low-cost inkjet printing process described in Chapter 3 and originally developed by Dixon et al.<sup>18,50</sup> As highlighted in Chapter 1, the expenses associated with traditional cleanroom fabrication of DMF devices are a major hurdle for the widespread implementation of DMF devices as point of care (POC) diagnostic tools. The inkjet-printing process used here eliminates the need for cleanroom facilities and is already a promising low-cost alternative for fabricating 2D DMF devices.<sup>18</sup> However several properties of these printed devices have not previously been characterized.

In this investigation, the conductivity and roughness of cleanroom-fabricated (CRF) and inkjet-printed (IJP) devices are compared. The adhesion energy of an unconfined 5  $\mu\text{L}$  droplet on each device types is then calculated and used to estimate the minimum threshold electrowetting number for ejection using Lee et al.'s adhesion model.<sup>56</sup> Droplet ejection is then demonstrated by applying ejection pulses at saturation voltage to droplets on both device types. Each device contains a single electrode and is actuated in a wired configuration using a 22  $\mu\text{m}$  tungsten wire inserted into the active droplet. All measurement errors are reported as one standard deviation from the mean unless otherwise specified.

The material presented in this chapter has previously been published in *Microfluidics and Nanofluidics*.<sup>37</sup> Material from: 'Bernetski, K. A.; Burkhart, C. T.; Maki, K. L.; Schertzer, M. J.; Characterization of Electrowetting, Contact Angle Hysteresis, and

Adhesion on Digital Microfluidic Devices with Inkjet-Printed Electrodes; Microfluids and Nanofluids; published 2018; Springer Nature.'

## 6.1 Conductivity of Printed Electrodes

Conductivity of printed electrodes (Fig. 6.1) was characterized prior to fabricating complete devices for ejection testing. The IJP electrodes fabricated by Dixon et al.<sup>50</sup> were not actively sintered and were simply allowed to cure overnight prior to being coated. Photonic curing allows for conductivity to be improved without thermally damaging the flexible polymer substrate used in the inkjet-printed devices. Here two active photonic curing techniques and their impact on conductivity were examined. The first active technique was based on a low-cost process reported by Yung et al.<sup>77</sup> involving a simple



**Figure 6.1** An early inkjet-printed electrode.

camera flash (Nikon Speedlight DB-600, ~\$100 USD). Electrodes were positioned ~1 cm away from the flash and exposed one, two, or three times. The second involved photosintering devices in an industrial photonic curing system (Novacentrix PulseForge 3300, ~\$1M USD) at 200 V for 400  $\mu$ s. PulseForge processing is not conducive to low-cost applications, but it served as a reference for comparing the effectiveness of the low-cost alternatives. To further explore the effects of passive curing each technique was used on a freshly printed device and on a device allowed to rest for approximately two weeks. To compare conductivities, six measurements of sheet resistance were taken across each device using a four-point probe (Jandel RM 3000+).

Freshly printed electrodes were found to have a sheet resistance of  $745 \pm 53 \text{ m}\Omega/\text{sq}$  (Fig. 6.2). Camera flash exposure reduced resistivity, but diminishing returns were observed with multiple exposures. The maximum reduction in resistivity was approximately 17% after three exposures. This was consistent with results reported by Yung et al.<sup>77</sup> As expected, the improvement in resistivity with the PulseForge (~84%) was far superior to that of the low-cost camera flash method. Electrodes that were allowed to rest had lower sheet resistances in all cases. Interestingly, the rested electrode that was not actively sintered had a lower sheet resistance than all the fresh and actively sintered electrodes aside from the PulseForge case.

While both active curing techniques reduced sheet resistance, neither was performed when fabricating the ejection devices tested later in this chapter. Instead, electrodes were allowed to dry at least overnight as done by Dixon et al.<sup>50</sup> The benefit of improved conductivity in the devices is likely small since they contain no complex electrode geometry and the current in the devices is negligible. Furthermore, both

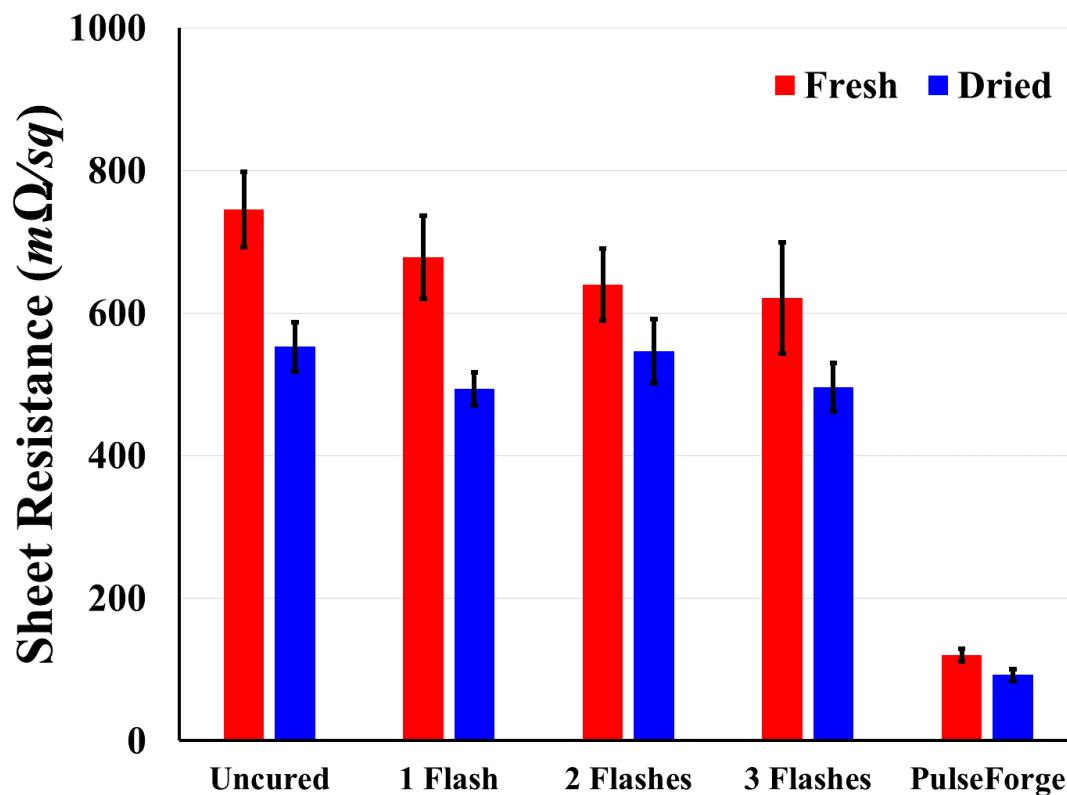


**Figure 6.2** Conductivity of fresh and dried printed electrodes samples after various curing techniques.<sup>37</sup>

techniques represent an increase in device cost and processing time. While these methods were not implemented here, they may be attractive for more widely spread commercial applications.

## 6.2 Roughness, Dielectric Thickness, and Adhesion

Surface roughness of inkjet-printed electrodes was examined to determine if it would have a significant impact on the hydrophobicity of the final device surface. An increased density of surface defects can decrease the initial contact angle of a droplet<sup>78</sup> and

in turn inhibit droplet ejection.<sup>56</sup> Surface defects can also result in local variations in the thickness of the dielectric layer and create variations in the local electrowetting number.

The root-mean-square roughness of the printed electrodes was measured in three  $0.5 \text{ mm} \times 0.5 \text{ mm}$  regions across multiple devices using a Nanovea ST400 profilometer and found to be  $400 \text{ nm} \pm 85 \text{ nm}$ . This is approximately three times greater than the roughness reported by Dixon et al.<sup>50</sup> After deposition of the dielectric and hydrophobic films, roughness on IJP devices was measured to be  $189 \text{ nm} \pm 6 \text{ nm}$ . Roughness on coated CRF devices was measured to be  $73 \text{ nm} \pm 4 \text{ nm}$ , which is approximately the resolution of the profilometer. This suggests that increased roughness on an IJP electrode can affect roughness of the polymer layers subsequently spin coated over them.

Initial contact angles ( $\theta_0$ ) were measured on both device types and found to be slightly lower on IJP devices ( $115.7^\circ$ ) as compared to CRF devices ( $118.5^\circ$ ).<sup>37</sup> The lower initial contact angle on IJP devices indicates greater surface adhesion. Adhesion work per area ( $w_{\text{adh}}$ ) can be estimated as

$$w_{\text{adh}} \approx \gamma_{\text{lg}}[1 + \cos(\theta_0)], \quad (6.1)$$

where  $\theta_0$  is the initial contact angle of a droplet on the surface and  $\gamma_{\text{lg}}$  is the surface tension between the droplet and the surrounding medium.<sup>56</sup> In order for an actuated droplet to eject from the surface, the electrical energy in the system ( $\gamma_{\text{lg}}Ew$ ) must at least be greater than this adhesion work. By equating the electrical energy and adhesion work, the minimum necessary electrowetting number for ejection ( $Ew_{\text{cr}}$ ) can be estimated as

$$Ew_{\text{cr}} = 1 + \cos(\theta_0). \quad (6.2)$$

The difference in initial contact angle results in a predicted  $Ew_{CR}$  for IJP devices (0.57) that is approximately 8% higher than on CRF devices (0.52).

The thickness of the dielectric layer in IJP and CRF devices was also measured and compared. Despite being deposited using the same spin coating parameters, the dielectric layer in the IJP devices was thinner ( $\sim 4.4 \mu m$ ) than in the CRF devices ( $\sim 6.4 \mu m$ ). This was attributed to the additional hydrophobic Teflon layer deposited directly over the printed electrodes in all IJP devices. Previous works have demonstrated that spin coating photoresist on fluoropolymers can be difficult due to the high hydrophobicity,<sup>79–81</sup> but sufficiently viscous photoresists ( $> 50 cSt$ ) can still be deposited directly.<sup>79</sup> The manufacturer reported viscosity of the SU-8 3005 photoresist used is  $65 cSt$ . The combination of the moderate photoresist viscosity and the hydrophobicity of the Teflon coating appear to result in a reduced thickness of spin-coated SU-8.

### 6.3 Droplet Ejection

The printing system was then used to produce single-electrode inkjet-printed devices (IJP1) for detachment trials in a wired configuration (Fig. 6.3). Prints were allowed to dry for a day or more prior to spin coating. Devices were tested with  $5 \mu L$  droplets actuated with  $7 ms$  pulses at varying DC voltages and recorded using DROPimage software at  $40 fps$ . Droplet ejection was also performed on single-electrode CRF devices for comparison.

Droplets were successfully ejected from printed devices with the application of  $120 V$  ( $Ew \approx 0.60$ ) (Fig. 6.4). This is the first reported demonstration of electrowetting-induced droplet ejection from an IJP device. Droplets on similarly tested single-electrode



**Figure 6.3** A single-electrode printed device used for droplet ejection.<sup>37</sup>

CRF devices (CRF1s) were also ejected at  $Ew \approx 0.48$ . The experimentally observed thresholds on both device types agreed well with the values predicted by the simple adhesion model. As expected, the increased adhesion energy on IJP devices required the addition of more electrical energy at the solid liquid interface than on CRF devices. This may not have been the case if the reduction in the initial contact angle increased  $Ew_{cr}$  beyond the threshold for contact angle saturation.

The frame rate used in this investigation (40 *fps*) was well below the 5000 *fps* used by Lee et al. to characterize the dynamics and maximum height of electrowetting-induced droplet detachment.<sup>56</sup> However, results presented here suggest that the wetting dynamics are likely similar on CRF and IJP devices since full detachment was observed at the predicted electrowetting number on both device types.

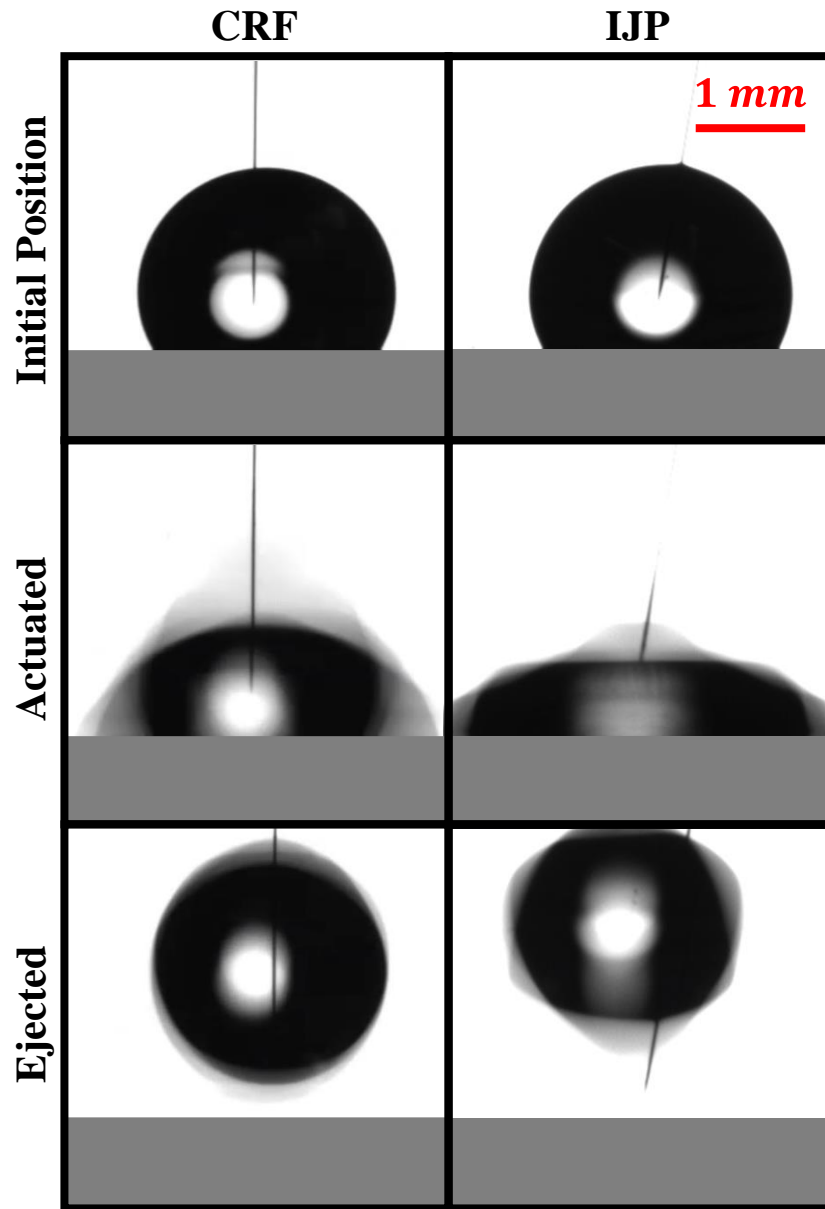


**Figure 6.4** Successful ejection of a  $5 \mu\text{L}$  droplet from an CRF and IJP device.<sup>37</sup>

## 6.4 Summary

Minimizing the cost of DMF devices is critical for their future development as POC diagnostic tools. The inkjet printing process examined here is a low-cost alternative to traditional cleanroom electrode fabrication. This investigation characterized the roughness

of printed electrodes and found there was a minimal impact on the hydrophobicity of the final coated surface despite the increased roughness. The experimental results presented also demonstrate that electrowetting-induced droplet ejection is possible on printed electrodes and can be predicted using a simple adhesion work model. The success here is promising for the future development of low-cost 3D DMF systems using this inkjet printing fabrication process.

## 7.0 Concluding Remarks

### 7.1 Summary

Digital microfluidic (DMF) devices are well suited for biological testing applications because they are automatable, reconfigurable, and can process a wide range of samples. Traditional 2D DMF devices have been used to perform chemical synthesis, particle filtration, immunoassays, and a variety of other biological protocols. However, cross-contamination is an ever present concern as droplets of biological reagents are processed. Newer 3D DMF devices can reduce cross contamination and improve testing sensitivity by routing droplets such that they never cross paths. These 3D systems leverage the first milliseconds of the electrowetting response in order to eject and transfer droplets between opposing substrates.

Understanding electrowetting-induced droplet ejection is critical for the future design and optimization of 3D DMF devices. Here, an analytical model for droplet ejection was developed that predicts the minimum electrowetting number necessary for successful detachment. This model expanded previous models of adhesion work and free interfacial energy changes throughout detachment by also accounting for gravitational potential energy changes. By approximating the droplet's maximally spread profile with its actuated steady-state profile, the ejection threshold can be predicted based on properties of the device and droplet known prior to experimentation. While the impact of gravitational force on droplet shape is generally neglected in DMF applications, gravitational potential energy changes throughout detachment were found to have a significant impact on the predicted threshold. As droplet size increased, this impact was greater. Droplet ejection experiments

confirmed that ejection thresholds were more accurately predicted by the newly developed interfacial plus gravitational potential energies model than previous models.

Optimizing the design of the ejection electrodes used can allow a target electrowetting number to be achieved at a lower input voltage. While a wired configuration allows for the lowest input voltage, such a design is not practical for real-world applications. In a coplanar electrode design, the input voltage is divided between dielectric material over active electrodes covered by a droplet and dielectric material over reference electrodes covered by a droplet. The area factor efficiency ( $\eta_A$ ) can be used to quantify how effectively an input voltage is applied to the entire droplet area in a given position. An ideal design will minimize dead space and allow a droplet cover active and reference electrodes equally. The different radially symmetric electrode designs examined here had close area factor efficiencies with the exception of the four-part design with  $200\ \mu\text{m}$  spacing (CRF4-200). However, ejection was possible with all designs at similar voltages despite the  $\sim 25\%$  dead space droplets covered on CRF4-200 devices. Recalculating the effective electrowetting number at only the contact line found the difference in the perimeter factor efficiency ( $\eta_P$ ) was much smaller. The experimental results suggest this contact line electrowetting number model is more appropriate for predicting the necessary threshold voltage, especially in cases with more sizable gaps between electrodes.

Reducing device fabrication costs will also be critical for the development of 3D DMF technology in point-of-care diagnostic applications. Inkjet printing is a promising low-cost alternative to traditional cleanroom fabrication that has been used to produce 2D DMF devices with features  $200\ \mu\text{m}$  and smaller. Here, an inexpensive commercial desktop inkjet printer ( $\sim \$120$  USD) was used to create single-electrode devices. Droplets were

successfully ejected in a wired configuration, demonstrating the feasibility of low-cost 3D DMF devices as well. The successful coplanar ejection on the CRF4-200 design suggests more practical coplanar electrodes can also be printed and used to eject droplets.

## **7.2 Contributions**

All work detailed here was performed with the intent of improving the current physical understanding of electrowetting-induced droplet ejection. The droplet ejection operation in DMF devices allows for 3D control that can minimize cross-contamination between reagents used and can approximately double the working area within a single device. As 3D DMF devices are developed for practical applications, a thorough understanding of ejection will be critical for designing functional and efficient systems.

In the first investigation presented (Chapter 4), a new analytical model for droplet ejection was developed that accounted for changes in gravitational potential energy and free interfacial energy throughout detachment. While gravitational potential energy changes were not considered in previous models, it was shown here analytically and experimentally that these changes have a significant impact on the energy barrier for detachment. This new model was able to predict critical electrowetting numbers for ejection more accurately than previous models. When designing future 3D DMF systems, this model can be used to predict the minimum electrowetting number a device must be able to achieve to ensure droplet ejection is possible. It was also demonstrated here that the radially symmetric electrode design used could achieve droplet ejection in air using single pulses rather than a double pulse signal. Incorporating a similar radially symmetric design

into a 3D DMF system at ejection sites could reduce the necessary complexity of the actuation system.

The subsequent investigation (Chapter 5) examined variations of the initial coplanar electrode design that had different electrode spacings and numbers of ejection pad segments. A numerical image processing technique was used to quantify droplet coverage prior to experimentation to predict performance on each design based on its area factor ( $\alpha_A$ ). The process used can readily be extended to analyze new designs as well. Analysis showed that small offsets on the radially symmetric designs did not significantly impact predicted performance. Droplets moving in 3D systems will always have a degree of imprecision, and it is useful to know what magnitude of offset can be tolerated. Experiments demonstrated that ejection was possible from designs with up to  $200 \mu m$  spacing, indicating that the area factor can underpredict performance in some cases. A new model of contact line electrowetting and reanalysis of the designs used suggested that a critical electrowetting number at the droplet contact line is necessary for ejection rather than a critical electrowetting number over the entire droplet area. How effectively a design distributes an input voltage to the contact line can be characterized by the new perimeter factor ( $\alpha_P$ ) developed here. This perimeter factor can be used to predict performance of new electrode designs. As future 3D DMF systems are developed, knowledge of how electrode layout and droplet positioning affect the perimeter factor can be leveraged to enable more efficient droplet ejection. Higher efficiency allows for ejection to be achieved at lower voltages and can reduce constraints on the actuation system necessary for device operation.

In the final investigation presented (Chapter 6), an inkjet-printing process was used to create single-electrode DMF devices. The first reported droplet ejection from inkjet-printed electrodes was then achieved. The electrode fabrication technique used here was significantly less costly than traditional electrode fabrication in a cleanroom environment. Cleanroom accessibility can act as a barrier to entry for new research laboratories interested in studying droplet ejection. The success here demonstrates that this more accessible processes can also be used to create devices and examine droplet ejection. Low-cost alternative processes typically sacrifice feature resolution for cost. In the previous investigation coplanar ejection was achieved using a design with  $200\ \mu\text{m}$  spacing. This resolution was achievable using the printing system here. The wired droplet ejection from printed devices in conjunction with the coplanar ejection from cleanroom devices with  $200\ \mu\text{m}$  spacing suggest that coplanar ejection from printed devices is also feasible. In practice, that would mean complete 3D DMF systems could be fabricated using this low-cost system. This would make prototyping and studying new 3D systems more widely accessible and would help minimize diagnostic testing costs as printed devices are eventually developed for specific biological applications.

### **7.3 Future Work**

Findings from the investigations performed here lend themselves to several avenues of further research and exploration into electrowetting-induced droplet ejection. A model for the changes in interfacial and gravitational potential energies throughout detachment was developed in Chapter 4 and showed that the potential energy contribution was significant. This was confirmed experimentally by ejecting droplets upward off of devices.

However, droplets in a 3D DMF device can be transferred between the bottom and top surface in either direction. The developed model suggests that the threshold ejection voltage will be lower when ejecting a droplet downward, but this was not confirmed experimentally. Additional experiments investigating thresholds for the case of inverted ejection could further validate the model. The model developed here also implies that actuation at electrowetting numbers beyond the predicted threshold will result in excess energy when reaching the detached state. Previous ejection experiments have found that actuation beyond the threshold causes droplets to be ejected higher into the air.<sup>56</sup> The model proposed here could theoretically be rewritten to predict an ejection height for a given droplet volume and electrowetting number. Ejection experiments like those done here could be repeated to measure heights at different electrowetting numbers and validate the model, but this would require a high frame rate to ensure a droplet is observed at its apex. A model for ejection height would be beneficial for determining the voltage capabilities and substrate spacings necessary in complete 3D DMF systems.

Based on the successful coplanar ejection in Chapter 5 from CRF devices with printable electrode geometries, ejection from coplanar IJP devices seems feasible. The experiments in Chapter 6 demonstrated that single-electrode IJP devices were capable of droplet ejection in a wired configuration. These IJP electrodes could next be used to construct a proof-of-concept 3D DMF device where ejection is performed using an inserted wire to move a droplet between two devices. However, such a device would have limited practical applications. The more significant next step would be to print coplanar electrodes and then use them to perform electrowetting-induced droplet ejection. This would more

strongly demonstrate the feasibility of low-cost 3D DMF devices and further pave the way for more accessible 3D DMF devices in the future.

The ejection threshold model developed in Chapter 4 and the electrode geometry considerations examined in Chapter 5 can both be used to inform the development of future 3D DMF devices. One potential future application in particular is cell culturing. The traditional 2D DMF platform is already an attractive fluid handling option for cell culturing applications since it can reduce the need for manual processing or expensive robotic systems.<sup>16</sup> Devices have previously been used to seed, treat, detach, and sort cells. With the added functionality of droplet ejection, the 3D DMF platform could serve as an automated chemical delivery system. Such a system would consist of an open DMF plate positioned over a large culture dish or a microwell plate loaded with a number of smaller samples (Fig. 7.1). Droplets could then be positioned over precise regions or wells and ejected downward to deliver the loaded chemicals. Sequences of different droplet types could be delivered as necessary for a particular protocol. As with previous DMF devices, multiple droplets could be manipulated simultaneously to reduce processing times. However, this 3D system would also not need to interface directly with the cell culture and would not risk exposing cells to electric fields or heating in the event of device failure.<sup>16</sup>

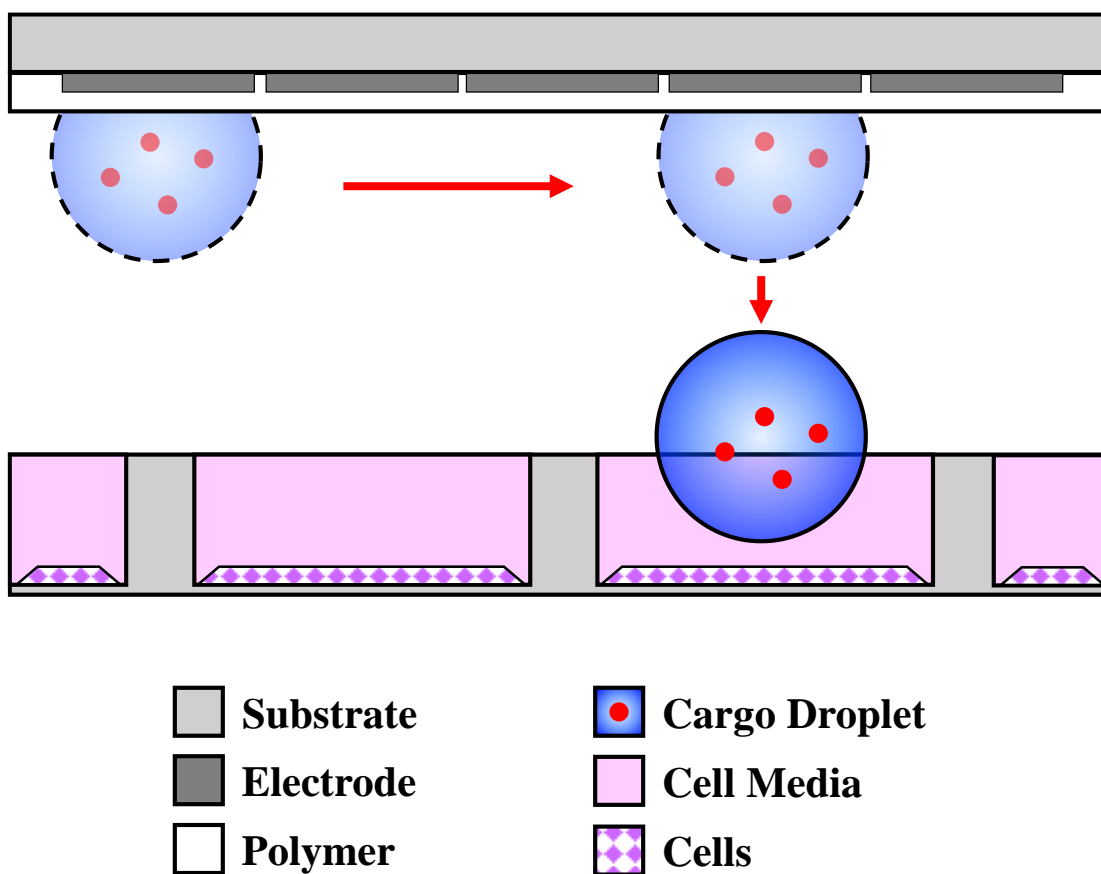


**Figure 7.1** Diagram of a proposed 3D DMF droplet delivery system for cell culturing applications.

## References

- (1) Whitesides, G. M. The Origins and the Future of Microfluidics. *Nature* **2006**, *442* (7101), 368–373. <https://doi.org/10.1038/nature05058>.
- (2) Duffy, D. C.; Gillis, H. L.; Lin, J.; Sheppard, N. F.; Kellogg, G. J.; Bioscience, G.; Avenue, B. Microfabricated Centrifugal Microfluidic Systems : Characterization and Multiple Enzymatic Assays. **1999**, *71* (20), 4669–4678. <https://doi.org/10.1021/ac990682c>.
- (3) Laser, D. J.; Santiago, J. G. A Review of Micropumps. *J. Micromech. Microeng.* **2004**, *14*, R35–R64. <https://doi.org/10.1088/0960-1317/14/6/R01>.
- (4) Beebe, D. J.; Mensing, G. A.; Walker, G. M. Physics and Applications of Microfluidics in Biology. *Annu. Rev. Biomed. Eng.* **2002**, *4*, 261–286. <https://doi.org/10.1146/annurev.bioeng.4.112601.125916>.
- (5) Lazar, I. M.; Karger, B. L. Multiple Open-Channel Electroosmotic Pumping System for Microfluidic Sample Handling. **2002**, *74* (24), 6259–6268. <https://doi.org/10.1021/ac0203950>.
- (6) Teh, S.-Y.; Lin, R.; Hung, L.-H.; Lee, A. P. Droplet Microfluidics. *Lab Chip* **2008**, *8* (2), 198–220. <https://doi.org/10.1039/b715524g>.
- (7) Choi, K.; Ng, A. H. C.; Fobel, R.; Wheeler, A. R. Digital Microfluidics. *Annu. Rev. Anal. Chem.* **2012**, *5* (1), 413–440. <https://doi.org/10.1146/annurev-anchem-062011-143028>.
- (8) Sin, M. L.; Gao, J.; Liao, J. C.; Wong, P. K. System Integration - A Major Step toward Lab on a Chip. *J. Biol. Eng.* **2011**, *5* (May), 6. <https://doi.org/10.1186/1754-1611-5-6>.

- (9) Nawar, M. (U. S. E. P. A. *Potential Nano-Enabled Environmental Applications for Radionuclides*; 2009.
- (10) Janasek, D.; Franzke, J.; Manz, A. Scaling and the Design of Miniaturized Chemical-Analysis Systems. *Nature* **2006**, *442* (7101), 374–380.  
<https://doi.org/10.1038/nature05059>.
- (11) Hill, D.; Sandström, N.; Gylfason, K.; Carlborg, F.; Karlsson, M.; Haraldsson, T.; Sohlström, H.; Russom, A.; Stemme, G.; Claes, T.; Bienstman, P.; Kazmierczak, A.; Dortu, F.; Bañuls Polo, M. J.; Maquieira, A.; Kresbach, G. M.; Vivien, L.; Popplewell, J.; Ronan, G.; Barrios, C. A.; Van Der Wijngaart, W. Microfluidic and Transducer Technologies for Lab on a Chip Applications. *2010 Annu. Int. Conf. IEEE Eng. Med. Biol. Soc. EMBC'10* **2010**, 305–307.  
<https://doi.org/10.1109/IEMBS.2010.5627523>.
- (12) Van den Berg, A. Labs on a Chip for Health Care Applications. *Int. Conf. Miniaturized Syst. Chem. Life Sci.* **2010**, No. October, 4–6.
- (13) Sista, R.; Hua, Z.; Thwar, P.; Sudarsan, A.; Srinivasan, V.; Eckhardt, A.; Pollack, M.; Pamula, V. Development of a Digital Microfluidic Platform for Point of Care Testing. *Lab Chip* **2008**, *8* (12), 2091–2104. <https://doi.org/10.1039/b814922d>.
- (14) Fair, R. B. Digital Microfluidics: Is a True Lab-on-a-Chip Possible? *Microfluid. Nanofluidics* **2007**, *3* (3), 245–281. <https://doi.org/10.1007/s10404-007-0161-8>.
- (15) Berthier, J. *The Physics of Microdroplets*, 1st ed.; Wiley-Scrivener, 2012.
- (16) Ng, A. H. C.; Li, B. B.; Chamberlain, M. D.; Wheeler, A. R. Digital Microfluidic Cell Culture. *Annu. Rev. Biomed. Eng.* **2015**, *17* (1), 91–112.  
<https://doi.org/10.1146/annurev-bioeng-071114-040808>.

- (17) Yoon, J. Y.; Garrell, R. L. Preventing Biomolecular Adsorption in Electrowetting-Based Biofluidic Chips. *Anal. Chem.* **2003**, *75* (19), 5097–5102.  
<https://doi.org/10.1021/ac0342673>.
- (18) Ng, A. H. C.; Fobel, R.; Fobel, C.; Lamanna, J.; Rackus, D. G.; Summers, A.; Dixon, C.; Dryden, M. D. M.; Lam, C.; Ho, M.; Mufti, N. S.; Lee, V.; Asri, M. A. M.; Sykes, E. A.; Champerlain, M. D.; Joseph, R.; Ope, M.; Scobie, H. M.; Knipes, A.; Rota, P. A.; Marano, N.; Chege, P. M.; Njuguna, M.; Nzunza, R.; Kisangau, N.; Kiogora, J.; Karuingi, M.; Burton, J. W.; Borus, P.; Lam, E.; Wheeler, A. R. A Digital Microfluidic System for Serological Immunoassays in Remote Settings. *Sci. Transl. Med.* **2018**, *10* (438), eaar6076.  
<https://doi.org/10.1126/scitranslmed.aar6076>.
- (19) Jebrail, M. J.; Bartsch, M. S.; Patel, K. D. Digital Microfluidics: A Versatile Tool for Applications in Chemistry, Biology and Medicine. *Lab Chip* **2012**, *12* (14), 2452–2463. <https://doi.org/10.1039/c2lc40318h>.
- (20) Wheeler, A. R.; Moon, H.; Bird, C. A.; Loo, R. R. O.; Kim, C. C. J.; Loo, J. A.; Garrell, R. L. Digital Microfluidics with In-Line Sample Purification for Proteomics Analyses with MALDI-MS Spot , Which Is Analyzed by MALDI-MS . This Purification. *Anal. Chem.* **2005**, *77* (2), 534–540.
- (21) Abdelgawad, M.; Freire, S. L. S.; Yang, H.; Wheeler, A. R. All-Terrain Droplet Actuation. *Lab Chip* **2008**, *8* (5), 672. <https://doi.org/10.1039/b801516c>.
- (22) Fiddes, L. K.; Luk, V. N.; Au, S. H.; Ng, A. H. C.; Luk, V.; Kumacheva, E. Hydrogel Discs for Digital Microfluidics. **2012**, *014112*, 1–11.  
<https://doi.org/10.1063/1.3687381>.

- (23) Brutin, D.; Sobac, B.; Loquet, B.; Sampol, J. Pattern Formation in Drying Drops of Blood. *J. Fluid Mech.* **2011**, *667* (January), 85–95.  
<https://doi.org/10.1017/S0022112010005070>.
- (24) Jebrail, M. J.; Wheeler, A. R. Digital Microfluidic Method for Protein Extraction by Precipitation. **2009**, *81* (1), 4833–4838.
- (25) Srinivasan, V.; Pamula, V. K.; Fair, R. B. An Integrated Digital Microfluidic Lab-on-a-Chip for Clinical Diagnostics on Human Physiological Fluids. *Lab Chip* **2004**, *4* (4), 310–315. <https://doi.org/10.1039/b403341h>.
- (26) Pollack, M. G.; Shenderov, A. D.; Fair, R. B. Electrowetting-Based Actuation of Droplets for Integrated Microfluidics. *Lab Chip* **2002**, *2* (2), 96–101.  
<https://doi.org/10.1039/b110474h>.
- (27) Ren, H.; Fair, R. B.; Pollack, M. G.; Shaughnessy, E. J. Dynamics of Electro-Wetting Droplet Transport. *Sensors Actuators B Chem.* **2002**, *87* (1), 201–206.  
[https://doi.org/10.1016/S0925-4005\(02\)00223-X](https://doi.org/10.1016/S0925-4005(02)00223-X).
- (28) Srinivasan, V.; Pamula, V. K.; Fair, R. B. Droplet-Based Microfluidic Lab-on-a-Chip for Glucose Detection. *Anal. Chim. Acta* **2004**, *507* (1), 145–150.  
<https://doi.org/10.1016/j.aca.2003.12.030>.
- (29) Yi, U.-C.; Kim, C.-J. Characterization of Electrowetting Actuation on Addressable Single-Side Coplanar Electrodes. *J. Micromechanics Microengineering* **2006**, *16* (10), 2053–2059. <https://doi.org/10.1088/0960-1317/16/10/018>.
- (30) Wang, G.; Teng, D.; Fan, S. K. Three-Dimensional Digital Microfluidics and Applications. *2012 7th IEEE Int. Conf. Nano/Micro Eng. Mol. Syst. NEMS 2012* **2012**, 415–418. <https://doi.org/10.1109/NEMS.2012.6196807>.

- (31) Chae, J. B.; Shin, I. U.; Rhee, K.; Chung, S. K. Three-Dimensional Digital Microfluidics Using an Alternative Current Electrowetting-on-Dielectric (AC-EWOD). *2013 Transducers Eurosensors XXVII 17th Int. Conf. Solid-State Sensors, Actuators Microsystems, TRANSDUCERS EUROSENSORS 2013* **2013**, No. June, 1286–1289. <https://doi.org/10.1109/Transducers.2013.6627011>.
- (32) Chae, J. B.; Lee, S. J.; Yang, J.; Chung, S. K. 3D Electrowetting-on-Dielectric Actuation. *Sensors Actuators, A Phys.* **2015**, *234*, 331–338. <https://doi.org/10.1016/j.sna.2015.09.004>.
- (33) Hong, J.; Kim, Y. K.; Kang, K. H.; Kim, J.; Lee, S. J. Spreading Dynamics and Oil Film Entrapment of Sessile Drops Submerged in Oil Driven by DC Electrowetting. *Sensors Actuators, B Chem.* **2014**, *196*, 292–297. <https://doi.org/10.1016/j.snb.2014.02.020>.
- (34) Hong, J.; Kim, Y. K.; Won, D.-J.; Kim, J.; Lee, S. J. Three-Dimensional Digital Microfluidic Manipulation of Droplets in Oil Medium. *Sci. Rep.* **2015**, *5*, 10685. <https://doi.org/10.1038/srep10685>.
- (35) Burkhart, C. T.; Maki, K. L.; Schertzer, M. J. Coplanar Electrowetting-Induced Droplet Detachment from Radially Symmetric Electrodes. *Langmuir* **2020**, *36* (28), 8129–8136. <https://doi.org/10.1021/acs.langmuir.0c01015>.
- (36) Burkhart, C. T.; Maki, K. L.; Schertzer, M. J. Radially Symmetric Electrode Segmentation and Spacing for Electrowetting-Induced Droplet Ejection. **2021**.
- (37) Bernetski, K. A.; Burkhart, C. T.; Maki, K. L.; Schertzer, M. J. Characterization of Electrowetting, Contact Angle Hysteresis, and Adhesion on Digital Microfluidic Devices with Inkjet-Printed Electrodes. *Microfluid. Nanofluidics* **2018**, *22* (9).

<https://doi.org/10.1007/s10404-018-2119-4>.

- (38) Cavalli, A.; Preston, D. J.; Tio, E.; Martin, D. W.; Miljkovic, N.; Wang, E. N.; Blanchette, F.; Bush, J. W. M. Electrically Induced Drop Detachment and Ejection. *Phys. Fluids* **2016**, *28* (2). <https://doi.org/10.1063/1.4940213>.
- (39) Jun Lee, S.; Lee, S.; Hyoung Kang, K. Droplet Jumping by Electrowetting and Its Application to the Three-Dimensional Digital Microfluidics. *Appl. Phys. Lett.* **2012**, *100* (8). <https://doi.org/10.1063/1.3688487>.
- (40) Hong, J.; Lee, S. J. Detaching Droplets in Immiscible Fluids from a Solid Substrate with the Help of Electrowetting. *Lab Chip* **2015**, *15* (3), 900–907. <https://doi.org/10.1039/C4LC01049C>.
- (41) Zhao, Y.; Chakrabarty, K. Cross-Contamination Avoidance for Droplet Routing in Digital Microfluidic Biochips. *IEEE Trans. Comput. Des. Integr. Circuits Syst.* **2012**, *31* (6), 817–830. <https://doi.org/10.1109/TCAD.2012.2183369>.
- (42) Lin, C. C. Y.; Chang, Y. W. Cross-Contamination Aware Design Methodology for Pin-Constrained Digital Microfluidic Biochips. *IEEE Trans. Comput. Des. Integr. Circuits Syst.* **2011**, *30* (6), 817–828. <https://doi.org/10.1109/TCAD.2011.2108010>.
- (43) Fiorini, G. S.; Chiu, D. T. Disposable Microfluidic Devices : Fabrication, Function, and Application. **2005**, *446* (March), 429–446.
- (44) Coltro, W. K. T.; De Jesus, D. P.; Da Silva, J. A. F.; Do Lago, C. L.; Carrilho, E. Toner and Paper-Based Fabrication Techniques for Microfluidic Applications. *Electrophoresis* **2010**, *31* (15), 2487–2498. <https://doi.org/10.1002/elps.201000063>.

- (45) Coltro, W. K. T.; Silva, J. A. F. da; Carrilho, E. Rapid Prototyping of Polymeric Electrophoresis Microchips with Integrated Copper Electrodes for Contactless Conductivity Detection. *Anal. Methods* **2011**, 168–172.  
<https://doi.org/10.1039/c0ay00486c>.
- (46) Watson, M. W. L.; Abdelgawad, M.; Ye, G.; Yonson, N.; Trottier, J.; Wheeler, A. R. Microcontact Printing-Based Fabrication of Digital Microfluidic Devices. *Anal. Chem.* **2006**, 78 (22), 7877–7885. <https://doi.org/10.1021/ac0613378>.
- (47) Abdelgawad, M.; Wheeler, A. R. Rapid Prototyping in Copper Substrates for Digital Microfluidics. *Adv. Mater.* **2007**, 19 (1), 133–137.  
<https://doi.org/10.1002/adma.200601818>.
- (48) Abdelgawad, M.; Wheeler, A. R. Low-Cost, Rapid-Prototyping of Digital Microfluidics Devices. *Microfluid. Nanofluidics* **2007**, 4 (4), 349–355.  
<https://doi.org/10.1007/s10404-007-0190-3>.
- (49) Fobel, R.; Kirby, A. E.; Ng, A. H. C.; Farnood, R. R.; Wheeler, A. R. Paper Microfluidics Goes Digital. *Adv. Mater.* **2014**, 26 (18), 2838–2843.  
<https://doi.org/10.1002/adma.201305168>.
- (50) Dixon, C.; Ng, A. H. C.; Fobel, R.; Miltenburg, M. B.; Wheeler, A. R. An Inkjet Printed, Roll-Coated Digital Microfluidic Device for Inexpensive, Miniaturized Diagnostic Assays. *Lab Chip* **2016**, 16, 4560–4568.  
<https://doi.org/10.1039/C6LC01064D>.
- (51) Ko, H.; Lee, J.; Kim, Y.; Lee, B.; Jung, C. H.; Choi, J. H.; Kwon, O. S.; Shin, K. Active Digital Microfluidic Paper Chips with Inkjet-Printed Patterned Electrodes. *Adv. Mater.* **2014**, 26 (15), 2335–2340. <https://doi.org/10.1002/adma.201305014>.

- (52) 't Mannetje, D. J. C. M.; Murade, C. U.; Van Den Ende, D.; Mugele, F.  
Electrically Assisted Drop Sliding on Inclined Planes. *Appl. Phys. Lett.* **2011**, *98*  
(1). <https://doi.org/10.1063/1.3533362>.
- (53) Yong Lee, K.; Hong, J.; Chung, S. K. Smart Self-Cleaning Lens Cover for  
Miniature Cameras of Automobiles. *Sensors Actuators, B Chem.* **2017**, *239*, 754–  
758. <https://doi.org/10.1016/j.snb.2016.08.032>.
- (54) Kim, J.; Kaviany, M. Purging of Dropwise Condensate by Electrowetting. *J. Appl.*  
*Phys.* **2007**, *101* (10). <https://doi.org/10.1063/1.2734933>.
- (55) Kim, J.; Kaviany, M. Electrowetting Purged Surface Condensate in Evaporators.  
*Heat Transf. Eng.* **2010**, *31* (2), 101–107.  
<https://doi.org/10.1080/01457630903285302>.
- (56) Lee, S. J.; Hong, J.; Kang, K. H.; Kang, I. S.; Lee, S. J. Electrowetting-Induced  
Droplet Detachment from Hydrophobic Surfaces. *Langmuir* **2014**, *30* (7), 1805–  
1811. <https://doi.org/10.1021/la404344y>.
- (57) Burkhart, C. T. Droplet Ejection for 3D Digital Microfluidics. *The Rochester*  
*Engineer*. 2020, pp 14–15.
- (58) Mugele, F.; Baret, J.-C. Electrowetting: From Basics to Applications. *J. Phys.*  
*Condens. Matter* **2005**, *17* (28), R705–R774. [https://doi.org/10.1088/0953-  
8984/17/28/R01](https://doi.org/10.1088/0953-8984/17/28/R01).
- (59) Nelson, W. C.; Kim, C. C. J. Droplet Actuation by Electrowetting-on-Dielectric  
(EWOD): A Review. *J. Adhes. Sci. Technol.* **2012**, *26* (12–17), 1747–1771.
- (60) Lippmann, M. G. Relations Entre Les Phénomènes Électriques et Capillaires. *Ann.*  
*Chim. Phys.* 1875, p 494.

- (61) Berge, B. Électrocapillarité et Mouillage de Films Isolants Par l'eau. *C. R. Acad. Sc. Paris, Série II* **1993**, 317, 157–163.
- (62) Liu, H.; Dharmatilleke, S.; Maurya, D. K.; Tay, A. A. O. Dielectric Materials for Electrowetting-on-Dielectric Actuation. *Microsyst. Technol.* **2010**, 16 (3), 449–460. <https://doi.org/10.1007/s00542-009-0933-z>.
- (63) Hu, H.; Larson, R. G. Analysis of the Microfluid Flow in an Evaporating Sessile Droplet. *Langmuir* **2005**, 21 (9), 3963–3971. <https://doi.org/10.1021/la047528s>.
- (64) Hong, J.; Kim, Y. K.; Kang, K. H.; Oh, J. M.; Kang, I. S. Effects of Drop Size and Viscosity on Spreading Dynamics in DC Electrowetting. *Langmuir* **2013**, 29 (29), 9118–9125. <https://doi.org/10.1021/la401801u>.
- (65) Kang, K. H. How Electrostatic Fields Change Contact Angle In. **2002**, No. 10, 10318–10322.
- (66) Klarman, D.; Andelman, D.; Urbakh, M. A Model of Electrowetting, Reversed Electrowetting, and Contact Angle Saturation. *Langmuir* **2011**, 27 (10), 6031–6041. <https://doi.org/10.1021/la2004326>.
- (67) Mugele, F. Fundamental Challenges in Electrowetting: From Equilibrium Shapes to Contact Angle Saturation and Drop Dynamics. *Soft Matter* **2009**, 5 (18), 3377. <https://doi.org/10.1039/b904493k>.
- (68) Walker, S.; Shapiro, B. Modeling the Fluid Dynamics of Electrowetting on Dielectric (EWOD). *J. Microelectromechanical Syst.* **2006**, 15 (4), 986.
- (69) Lee, S. J.; Lee, S.; Kang, K. H. Jumping of a Droplet on a Superhydrophobic Surface in AC Electrowetting. *J. Vis.* **2011**, 14 (3), 259–264. <https://doi.org/10.1007/s12650-011-0076-z>.

- (70) Hong, J.; Kim, Y. K.; Kang, K. H.; Kim, J.; Lee, S. J. Effects of Drop Viscosity on Oscillation Dynamics Induced by AC Electrowetting. *Sensors Actuators, B Chem.* **2014**, *190*, 48–54. <https://doi.org/10.1016/j.snb.2013.08.057>.
- (71) Vo, Q.; Su, H.; Tran, T. Universal Transient Dynamics of Electrowetting Droplets. *Sci. Rep.* **2018**, 1–7. <https://doi.org/10.1038/s41598-018-19167-7>.
- (72) Nelson, W. C.; Peng, I.; Lee, G.-A.; Loo, J. A.; Garrel, R. L.; Kim, C.-J. Incubated Protein Reduction and Digestion on an EWOD Digital Microfluidic Chip for MALDI-MS. **2010**, *82* (23), 9932–9937. <https://doi.org/10.1021/ac101833b.Incubated>.
- (73) Moon, H.; Wheeler, A. R.; Garrell, R. L.; Loo, J. A.; Kim, C. J. An Integrated Digital Microfluidic Chip for Multiplexed Proteomic Sample Preparation and Analysis by MALDI-MS. *Lab Chip* **2006**, *6* (9), 1213–1219. <https://doi.org/10.1039/b601954d>.
- (74) Luk, V. N.; Mo, G. C. . H.; Wheeler, A. R. Pluronic Additives: A Solution to Sticky Problems in Digital Microfluidics. *Langmuir* **2008**, *24* (12), 6382–6389.
- (75) Eppendorf Research plus - Technical Data [https://www.eppendorf.com/product-media/doc/en/672922/Liquid-Handling\\_Technical-data\\_Research-plus\\_Eppendorf-Research-plus.pdf](https://www.eppendorf.com/product-media/doc/en/672922/Liquid-Handling_Technical-data_Research-plus_Eppendorf-Research-plus.pdf).
- (76) Hadwen, B.; Broder, G. R.; Morganti, D.; Jacobs, A.; Brown, C.; Hector, J. R.; Kubota, Y.; Morgan, H. Programmable Large Area Digital Microfluidic Array with Integrated Droplet Sensing for Bioassays. *Lab Chip* **2012**, *12* (18), 3305–3313. <https://doi.org/10.1039/c2lc40273d>.
- (77) Yung, K. C.; Gu, X.; Lee, C. P.; Choy, H. S. Ink-Jet Printing and Camera Flash

- Sintering of Silver Tracks on Different Substrates. *J. Mater. Process. Technol.* **2010**, *210* (15), 2268–2272. <https://doi.org/10.1016/j.jmatprotec.2010.08.014>.
- (78) Kozbial, A.; Trouba, C.; Liu, H.; Li, L. Characterization of the Intrinsic Water Wettability of Graphite Using Contact Angle Measurements : Effect of Defects on Static and Dynamic Contact Angles. *Langmuir* **2017**, *33* (4), 959–967. <https://doi.org/10.1021/acs.langmuir.6b04193>.
- (79) Li, Y.; Mckenna, E. O.; Parkes, W.; Pitt, A. R.; Walton, A. J. The Application of Fixed Hydrophobic Patterns for Confinement of Aqueous Solutions in Proteomic Microarrays. *Appl. Phys. Lett.* **2011**, *99* (073703), 1–3. <https://doi.org/10.1063/1.3626037>.
- (80) Ikawa, M.; Yamada, T.; Matsui, H.; Minemawari, H.; Tsutsumi, J.; Horii, Y.; Chikamatsu, M.; Azumi, R.; Kumai, R.; Hasegawa, T. Simple Push Coating of Polymer Thin-Film Transistors. *Nat. Commun.* **2012**, *3* (1176), 1–8. <https://doi.org/10.1038/ncomms2190>.
- (81) Zhang, H.; Yan, Q.; Xu, Q.; Xiao, C.; Liang, X. A Sacrificial Layer Strategy for Photolithography on Highly Hydrophobic Surface and Its Application for Electrowetting Devices. **2017**, No. March, 1–7. <https://doi.org/10.1038/s41598-017-04342-z>.